

University of Louisville

## ThinkIR: The University of Louisville's Institutional Repository

---

Electronic Theses and Dissertations

---

5-2014

### Low power strain sensor based on MOS tunneling current.

Li Zhu

*University of Louisville*

Follow this and additional works at: <https://ir.library.louisville.edu/etd>



Part of the [Electrical and Computer Engineering Commons](#)

---

#### Recommended Citation

Zhu, Li, "Low power strain sensor based on MOS tunneling current." (2014). *Electronic Theses and Dissertations*. Paper 1648.

<https://doi.org/10.18297/etd/1648>

This Doctoral Dissertation is brought to you for free and open access by ThinkIR: The University of Louisville's Institutional Repository. It has been accepted for inclusion in Electronic Theses and Dissertations by an authorized administrator of ThinkIR: The University of Louisville's Institutional Repository. This title appears here courtesy of the author, who has retained all other copyrights. For more information, please contact [thinkir@louisville.edu](mailto:thinkir@louisville.edu).

LOW POWER STRAIN SENSOR BASED ON MOS TUNNELING CURRENT

By

Li Zhu

B.S., Beijing Institute of Technology, China, 2007

M.S., Beijing Institute of Technology, China, 2009

A Dissertation

Submitted to the Faculty of the

J. B. Speed School of Engineering of the University of Louisville

in Partial Fulfillment of the Requirements

for the Degree of

Doctor of Philosophy

Department of Electrical and Computer Engineering

University of Louisville

May 2014

Copyright 2014 by Li Zhu

All rights reserved



LOW POWER STRAIN SENSOR BASED ON MOS TUNNELING CURRENT

By

Li Zhu

B.S., Beijing Institute of Technology, China, 2007

M.S., Beijing Institute of Technology, China, 2009

A Dissertation Approved on

April 21, 2014

by the following Dissertation Committee:

---

Shamus McNamara, Ph.D

---

Kevin Walsh, Ph.D

---

John Naber, Ph.D

---

Sergio Mendes, Ph.D

---

Gamini Sumanasekera, Ph.D

## DEDICATION

This dissertation is dedicated to my family, especially  
to my parents, Xingqi Zhu and Hongmei Zhang, who guide me and support  
me for over 20 years;  
to my wife, Mingxia, for being a great wife;  
to my new born lovely boy, Yicheng, for his cheerful smile.

## ACKNOWLEDGMENTS

I would like to give my deepest appreciation to my advisor Dr. Shamus McNamara. He has demonstrated himself as a great mentor in both research and daily life. He never hesitates to give his help and guidance whenever I have questions about experiment, documentation and presentation. He is serious about everything he works on. In the same time, he always smiles when I speak with him, which is really cheerful and warm.

I also would like to thank my committee members, Dr. Kevin Walsh, Dr. John Naber, Dr. Sergio Mendes and Dr. Gamini Sumanasekera. They have been very helpful on my research. Dr. Kevin Walsh and Dr. John Naber have given me a lot useful suggestions on my research and have been very generous to let me use instruments in their labs. Dr. Sergio Mendes and Dr. Gamini Sumanasekera gave me a lot helpful ideas during my dissertation proposal and research.

I want to thank my previous and current lab colleges, Dr. Chakravarthy Yamarthy, Dr. Kunal Pharas, Alexander Bell, Stephanie Miles, Abderrazzak Faiz, Mark Crain, Pranoy Shuvra and Bryan Snatchko. Especially thanks to Dr. Kunal Pharas. He is a great friend. I still remember that he showed me around the campus of University of Louisville when I first came to the university. He was very patient when he was my cleanroom “buddy”. He shares a lot of ideas in both research and life with me. Mr. Mark Crain has been very helpful with suggestions on micro-fabrication. I also thank Douglas Jackson and Thomas Roussel. Doug has helped me a lot in circuit design and experiments.

I am really impressed by his fancy tools and gadgets. He is a very experienced engineer, and he always has an answer to my questions. Thomas is definitely an expert in software and programming. He has done a great job in set up and maintaining the KRUNCH server. His experience in MEMS modeling and Labview was really a great help to me.

I also appreciate staff in Micro/Nano Technology Center. Without their hard work to maintain cleanroom instruments, I would never be able to make any devices and do my research.

I also would like to thank my dear friends in Louisville, Dr. Huihang Dong, Dr. Dongqing Chen, Dr. Hui Wang, Dr. Xinghua Sun, Dr. Mingxiao Li, Shuangshuang Jiang, Hanwen Yuan, Jason Li, etc. It is my great honor to have them as my friends. Their friendship and encouragement keep me positive during my research and daily life.

Last, I want to give most thanks to my family, especially my wife, Mingxia Liu, my son, Yicheng, my parents and in-laws. Mingxia is not only a great wife, but a heart-to-heart friend. She always takes care of my daily life, reminds me of every important thing, encourages me and gives me her love. I also want to thank her for giving birth to our lovely angel, Yicheng, who is now our family's biggest source of happiness.



## ABSTRACT

### LOW POWER STRAIN SENSOR BASED ON MOS TUNNELING CURRENT

Li Zhu

April 12, 2014

Sensors, such as pressure sensors, accelerometers and gyroscopes, are very important components in modern portable electronics. A limited source of power in portable electronics is motivating research on new low power sensors. Piezoresistive and capacitive sensing technologies are the most commonly utilized technologies, which typically consume power in the  $\mu\text{W}$  to  $\text{mW}$  range. Tunneling current sensing is attractive for low power applications because the typical tunneling current is in the  $\text{nA}$  range.

This dissertation demonstrates a low power strain sensor based on the tunneling current in a metal-oxide-semiconductor (MOS) structure with a power consumption of a couple of nano-Watts (nW) with a minimum detectable strain of 0.00036%. Both DC and AC measurements were used to characterize the MOS tunneling current strain sensor. The noise level is found to be smallest in the inversion region, and therefore it is best to bias the device in the inversion region.

To study the sensitivity in the inversion region, a model is developed to compute the tunneling current as a function of strain in the semiconductor. The model calculates the tunneling current due to electrons tunneling from the

conduction band of the semiconductor to the gate (ECB tunneling current) and the tunneling current due to electrons tunneling from the valence band of the semiconductor to the gate (EVB tunneling current). It is found that the ECB tunneling current is sufficient to explain experimental gate leakage current results reported in the literature for MOSFETs with low substrate doping concentration. However, for the tunneling current strain sensor with a higher substrate doping concentration reported here, a model using both ECB and EVB tunneling current is required. The model fits our experiments.

During both DC and AC measurements, the MOS tunneling current is found to drift with time. The drift could arise from the trap states within the oxide. The current drift makes it difficult to obtain an absolute measurement of the strain. Combining the tunneling current strain sensor with a resonant sensor may be a good choice because it measures changes in the mechanical resonant frequency, independent of a drift of the tunneling current amplitude.

## TABLE OF CONTENTS

DEDICATION	iii
ACKNOWLEDGMENTS	iv
ABSTRACT	vi
LIST OF TABLES	xii
LIST OF FIGURES	xiii
CHAPTER 1 INTRODUCTION	1
1.1 Motivation	1
1.2 Relevance of the research	5
1.3 Outline of Dissertation	6
CHAPTER 2 INTRODUCTION TO MOS TUNNELING CURRENT	9
2.1 History of quantum tunneling studying	9
2.2 Different Types of Tunneling current in MOS capacitor	12
2.3 Derivation of Fowler-Nordheim tunneling current equation in MOS structure	15
2.3.1 Tsu and Esaki model for Fowler-Nordheim tunneling current equation	16
2.3.2 The WKB method	19
2.4 Direct tunneling in MOS structure	26
2.4.1 Derivation of the direct tunneling formula	27
2.5 Summary	29
CHAPTER 3 STRAIN EFFECTS IN SILICON	31

3.1	Silicon band structure	31
3.2	Stress tensor	34
3.3	Strain tensor	35
3.4	Strain effects on silicon band structure	37
3.5	Summary	42
CHAPTER 4 EXPERIMENTS ON MOS TUNNELING CURRENT		43
4.1	Introduction	43
4.2	Fabrication and Measurement setup	45
4.3	DC experiments of strain effects on tunneling current	49
	4.3.1 Tensile strain	50
	4.3.2 Compressive strain	54
	4.3.3 Discussion	57
4.4	AC experiments of strain effects on tunneling current	58
	4.4.1 The principle of AC measurement	58
	4.4.2 Results and discussion	61
	4.4.3 Conclusions	67
CHAPTER 5 MOS STRAIN SENSOR SENSITIVITY STUDY BASED ON ECB AND EVB MODELING		69
5.1	Introduction	69
5.2	ECB modeling	70
	5.2.1 Approximate methods for quantized inversion layer	72
	5.2.2 ECB tunneling current using WKB approximation	76
	5.2.3 Strain induced ECB tunneling current changing	78
	5.2.4 Summary of ECB tunneling current modeling	81

5.3	EVB modeling	81
5.4	ECB and EVB tunneling current modeling for the MOS tunneling current strain sensor used in the DC measurement	84
5.5	Different doping concentration	88
5.6	Summary	92
CHAPTER 6 BULK ACOUSTIC LONGITUDINAL RF RESONATOR BASED ON MOS TUNNELING CURRENT STRAIN SENSOR		94
6.1	Introduction to RF MEMS resonator	94
6.2	Bulk Acoustic RF resonator based on MOS tunneling current strain sensor	96
6.2.1	Principle of bulk acoustic RF resonator	97
6.2.2	Fabrication of Bulk Acoustic RF resonator based on MOS tunneling current strain sensor	98
6.2.3	Bulk acoustic RF resonator testing	108
6.2.4	Testing and discussion	111
6.3	Suggestions for improvement in future	115
CHAPTER 7 CONCLUSIONS AND FUTURE DIRECTIONS		116
7.1	Conclusions	116
7.2	Future directions	118
7.2.1	Sensitivity study at different stresses	118
7.2.2	Continuing research on RF resonator based on MOS tunneling current strain sensor	119
7.3	Bolometer based on MOS tunneling current	120
REFERENCES		122



## LIST OF TABLES

Table 1	Summaries of advantages and disadvantages for different sensing methods.....	4
Table 2	Summaries of gauge factor, linearity and power consumption for different sensing methods.....	4
Table 3	Uniformity measurement result .....	47
Table 4	Analysis of experiment data .....	50
Table 5	Noise measurement at different frequencies.....	62
Table 6	Noise measurement at different time constant.....	64
Table 7	Values of effective masses used in this paper. ....	75
Table 8	Sensitivity vs. gate voltage from our group's experiment. ...	84
Table 9	Summary of vibrating shapes.....	96
Table 10	Parameters of the resonator .....	104
Table 11	Definition of components used in equivalent circuit .....	105
Table 12	Measurement results for substrate impedance .....	113
Table 13	Experiment result .....	121

## LIST OF FIGURES

Figure 2.1	FN tunneling (Figure is from [32]). .....	10
Figure 2.2	Current-Voltage relation of a tunneling diode [32]. .....	11
Figure 2.3	Band diagram of a tunneling diode at varies biases [32]. .....	12
Figure 2.4	Illustration of direct tunneling in MOS structure. (a) positive bias; (b) negative bias. ....	14
Figure 2.5	Schematic illustrating the Trap-assist-Tunneling current. The figure is from [42]. ....	15
Figure 2.6	Schematic illustrating Fowler-Nordheim Tunneling current. The figure is from [42]. ....	16
Figure 2.7	Schematic Illustrating for the WKB method. ....	20
Figure 2.8	Transfer matrix method [46]. ....	28
Figure 3.1	FCC lattice [48]. ....	32
Figure 3.2	Band structure of Silicon [50]. ....	33
Figure 3.3	The first Brillouin zone of Silicon [51]. ....	33
Figure 3.4	Stress components on the surfaces of an infinitesimal cube [52]. ....	34
Figure 3.5	Biaxial stress .....	38
Figure 3.6	Band splitting of Si under biaxial tensile stress [53] . ....	39
Figure 3.7	Uniaxial <110> stress [53]. ....	40
Figure 3.8	Band splitting of Si under uniaxial <110> compressive stress [53]. ....	41



Figure 3.9	Uniaxial stress on constant energy surface. (a) Deformation under uniaxial $\langle 110 \rangle$ stress. (b) Constant energy contour in (001) plane [53].	42
Figure 4.1	Fabrication process and the figure of MOS tunneling current strain sensor. (a). Fabrication process; (b). Picture of the device.	46
Figure 4.2	P type wafer for uniformity measurement using ellipsometer.	47
Figure 4.3	IV curve for MOS capacitor. (a). Good device; (b). Bad device.	48
Figure 4.4	Photograph of measurement setup, and illustration of MOS tunneling current strain sensor using cantilever beam. The MOS device is near the fixed end. (a). Measurement setup; (b). Illustration of MOS tunneling current strain sensor using cantilever beam.	49
Figure 4.5	Tunneling current versus time at different gate voltages and different tensile strain.	53
Figure 4.6	Tunneling current change versus tensile strain.	54
Figure 4.7	Tunneling current versus time at compressive strain.	56
Figure 4.8	Tunneling current change versus compressive strain.	57
Figure 4.9	(a) The top one is the setup for strain measurement and the bottom one is the setup for noise spectrum measurement. (b) The equivalent circuit for a MOS tunneling sensor.	59
Figure 4.10	Noise spectrum.	61

Figure 4.11	AC measurement at different frequencies when the time constant is 100 ms. ....	62
Figure 4.12	(a) AC measurement of different time constant at 1 kHz; (b) SD/avg vs. time constant. ....	64
Figure 4.13	DC method. (a) tunneling current at $V_{dc}=0.7$ V; (b) strain response at different DC voltages at the strain of 0.012%. ...	66
Figure 4.14	AC method. (a) tunneling current at $V_{rms}= 100$ mV, $V_{dc}=0.7$ V and 1 kHz; (b) strain response at different DC voltages at the strain of 0.012%. ....	67
Figure 5.1	NMOS in inversion region. ....	71
Figure 5.2	Sub-bands vs. gate voltage. The doping concentration of p-type substrate is $1e17$ $cm^{-3}$ . The doping concentration of n-type poly gate is $1e20$ $cm^{-3}$ . The thickness of gate oxide is 2.19 nm. ....	76
Figure 5.3	Gate current density vs. gate voltage. The device parameters are the same as used in Figure 5.2. The experiment results are from [66]. ....	78
Figure 5.4	Modeling vs. experimental results. For the tensile case, the doping concentration is $5e17$ $cm^{-3}$ for the p-type substrate and $1e20$ $cm^{-3}$ for the n-type poly gate. The thickness of gate oxide is 1.3 nm. The experimental data for the tensile is from [56]. For the compressive case, the doping concentration is $1e17$ $cm^{-3}$ for the p-type substrate and $1e20$ $cm^{-3}$ for the n-type poly gate. The thickness of gate oxide is 1.3 nm. The experimental data for the tensile is from [67]. ....	79

Figure 5.5	Percent change in current density versus voltage. The tensile and compressive stress are both 200 MPa. The parameters are the same as Figure 5.4. ....	81
Figure 5.6	EVB modeling. The parameters used in EVB modeling are the same as those in Fig. 2 in [71]. ....	83
Figure 5.7	Calculated current density for the MOS strain sensor without strain, including the ECB tunneling current, EVB tunneling current, and the total tunneling current. A comparison to the experimental results are also shown. ....	85
Figure 5.8	Sensitivity vs. gate voltage for ECB. ....	86
Figure 5.9	Calculated sensitivity vs. gate voltage for EVB tunneling current. ....	87
Figure 5.10	Sensitivity vs. gate voltage for total tunneling current. The line is calculated from the model, and the diamonds are the measured experimental results. ....	88
Figure 5.11	ECB modeling for different doping concentration. Parameters are the same as MOS tunneling current strain sensor in DC measurement. (a). Current density vs. gate voltage for ECB; (b). Sensitivity vs. gate current for ECB. ....	89
Figure 5.12	EVB modeling for different doping concentration. Parameters are the same as MOS tunneling current strain sensor in DC measurement. (a). Current density vs. gate voltage for EVB; (b). Sensitivity vs. gate current for EVB. ....	90

Figure 5.13	Total sensitivity vs. gate voltage at different doping concentration. Parameters are the same as MOS tunneling current strain sensor in DC measurement.....	91
Figure 6.1	(a) 3D structure of a bulk acoustic RF resonator; (b) a schematic showing working principle of longitudinal mode beam resonator [10]......	98
Figure 6.2	SEM picture and microscope picture of fabricated devices. (a) SEM pictures for top layer before etching sacrificial layer of SOI wafer. (b) Optical microscope picture for the final device which is misaligned and not fully released. (c) SEM picture of substrate layer for the final device which is misaligned. (d) Optical microscope picture of the final device which is misaligned but full released. (e) Packaged devices for testing.	103
Figure 6.3	Equivalent circuit for MOS tunneling current sensing method.	106
Figure 6.4	The output spectrum when $R \approx R1$ . (a) $\alpha \gg 1$ . (b) $\alpha \ll 1$ ...	108
Figure 6.5	Schematic for measurement set up. (a) Capacitive sensing method measurement set up. (b) MOS tunneling current sensing method measurement set up. (c) Picture of the measurement set up. ....	111
Figure 6.6	COMSOL modeling. The top bulk is contact which is $340 \mu\text{m}$ (x) $\times 340 \mu\text{m}$ (y) $\times 100 \mu\text{m}$ (z). The bottom bulk is Silicon which is $6\text{mm}$ (x) $\times 6\text{mm}$ (y) $\times 400\mu\text{m}$ (z). The voltage is $1 \text{ V}$ .....	114

Figure 6.7	Spice modeling of substrate contact influence on capacitive sensing method. (a) Equivalent circuit for capacitive sensing method. R3 is the output. (b) Simulation result with $R_g = 200 \Omega$ . (c) Simulation result with $R_g = 1 \Omega$ .....	115
Figure 7.1	Setup for sensitivity study at different stresses. ....	119
Figure 7.2	Table of commercial and state-of-the-art R&D uncooled infrared bolometers. ....	121

# CHAPTER 1

## INTRODUCTION

### 1.1 Motivation

Since the research about the piezoresistance of silicon was published by Smith from Bell Telephones Laboratories in 1954, people have been studying the possibility of making micro sensors which have a superior performance to macro sensors at power consumption, reliability and size [1, 2]. According to different applications, microelectromechanical systems (MEMS) sensors can be cataloged into pressure sensors, accelerometers, gyroscopes, flow sensors, etc. Among these MEMS sensors, pressure sensors and accelerometers have a leading position in the markets [3]. The MEMS sensors can also be grouped to piezoresistive sensors, piezoelectric sensors, capacitive sensors, etc. Piezoresistive sensors are among the earliest sensors, which are now being replaced by capacitive sensors.

Although MEMS pressure sensors and accelerometers have been widely researched and commercialized for decades, the recent increased demand for low power sensors is motivating research on new techniques. Portable electronics and biosensors in vivo usually require low power sensor to conserve power. Piezoresistive and capacitive sensing technologies are the most common technologies, which have been widely used to measure strain, pressure and acceleration [2, 4]. They both typically consume power from  $\mu\text{W}$

to mW [5].

As for the piezoresistive sensors, to achieve low power consumption, the doping concentration of the piezoresistor has to be decreased. For example, to have a minimum detectable strain of 0.001%, the doping concentration should be at least  $10^{16}$  atoms/cm<sup>3</sup> [6], and this doping concentration gives a resistivity of 1 ohm-cm. Information from [7] indicates that the MOS tunneling current through a 3.8 nm thick and 1 mm × 1 mm area SiO<sub>2</sub> layer is around 1 nA at 1 V, which results in a resistivity of  $10^{13}$  ohm-cm. It is obvious a good alternative for low power sensing compared with piezoresistive technology [7]. Besides the power consumption, another disadvantage of piezoresistive technology is that it is not easy to control the doping profile of the piezoresistive layer especially for a very thin layer [1]. The SiO<sub>2</sub> layer of the MOS tunneling sensor can be grown to less than 1 nm.

Capacitive sensors are the most common MEMS sensors now. They provide excellent low noise performance, high sensitivity, small temperature dependency and low power consumption. However parasitic capacitance of bond pads and small signal hinder the miniaturization of the capacitive sensors. Interface circuit is usually much more complex than piezoresistive sensors. The response is nonlinear, and both electrical and physical shielding is necessary [8, 9].

Besides adopting tunneling current through a MOS capacitor, tunneling sensors also employ tunneling current through an air gap between a tip and a plate which also have the merit of low power consumption. Pressure or acceleration induces displacement between the tip and the plate, which is read by the voltage or current changing [10-12]. The fabrication process of

this type of sensors is very complex. Like capacitive sensors, the response is also nonlinear. The interface circuit is very complex, which requires closed-loop control to maintain the gap distance. The reliability is also impacted due to deterioration of the tip.

The MOS tunneling sensors measure the current change induced by strain in silicon. The tunneling current is determined by the tunneling barrier between the silicon band edges and the gate dielectric band edges, as well as the effective mass. When a uniaxial strain is induced, the silicon band edges will be shift and split, which will change the tunneling barrier. As a result, the tunneling current changes with the strain. Detailed theory about the MOS tunneling sensors will be elaborated in the theory chapters.

Table 1 summarizes the advantages and the disadvantages of different MEMS sensors. The advantages are that the MOS tunneling current strain sensors are easy to fabricate and they are Complementary metal–oxide–semiconductor (CMOS) process compatible. However, the MOS tunneling current strain sensors are very sensitive to temperature like the piezoresistive sensors. Another disadvantage is that electrostatic discharge (ESD) protection is necessary, since the MOS tunneling current strain sensor is mainly a MOS capacitor.

Table 2 compares the gauge factor, the response linearity and the power consumption of different MEMS sensors. We can see that the gauge factor of MOS tunneling current strain sensor is in the same range of piezoresistive sensors, while its power consumption is much smaller. Here gauge factor is defined as  $GF = \frac{\Delta R/R}{\varepsilon} = \frac{\Delta I/I}{\varepsilon} = \frac{\Delta C/C}{\varepsilon}$ .



Table 1

Summaries of advantages and disadvantages for different sensing methods

	Advantages	Disadvantages
Piezoresistive	<ul style="list-style-type: none"> <li>• Simple interface circuit</li> </ul>	<ul style="list-style-type: none"> <li>• Large temperature dependency</li> <li>• Difficult to control Doping profile in the nm range</li> <li>• High power consumption</li> </ul>
Capacitive	<ul style="list-style-type: none"> <li>• Excellent noise performance</li> <li>• High sensitivity</li> <li>• Small temperature dependency</li> <li>• Low power consumption</li> </ul>	<ul style="list-style-type: none"> <li>• Large area</li> <li>• Complex circuit</li> <li>• Need electrical and physical shield</li> <li>• Non-linear</li> </ul>
Air gap Tunneling	<ul style="list-style-type: none"> <li>• High sensitivity</li> <li>• Small temperature dependency</li> </ul>	<ul style="list-style-type: none"> <li>• Complex interface circuit</li> <li>• Tip deterioration</li> <li>• Non-linear</li> </ul>
MOS tunneling	<ul style="list-style-type: none"> <li>• Low power consumption</li> <li>• Easy to miniaturize</li> </ul>	<ul style="list-style-type: none"> <li>• Temperature dependent</li> <li>• Need ESD protection</li> </ul>

Table 2

Summaries of gauge factor, linearity and power consumption for different sensing methods

Principle	Gauge Factor	Linearity	Power consumption
Piezoresistive	100 [9]	Linear	10 ~ 1000 uW [13, 14]
Capacitive	249 [15]	Nonlinear	~100 uW [16]
MOS Tunneling current	35 [7, 17]	Linear	1~100 nW [7]

## 1.2 Relevance of the research

This dissertation demonstrates the first use of tunneling current sensing for a sensor that is based on the effects of strain in the semiconductor substrate. Prior efforts to create tunneling current sensors all utilize the tunneling current through a gap between two materials, and thus inherently measure the gap between the electrodes. In this dissertation, it is fundamentally the strain in the semiconductor, and not the gap, that is measured.

Along with metal–oxide–semiconductor field-effect transistor (MOSFET) scaling, gate oxide is scaled down and MOS tunneling current or gate leakage current arises [18-20]. Since then, a lot of research on this MOS tunneling current has been done in both experimental and theoretical way [21-26]. Most of this research is focused on the performance of new high-k dielectric materials by studying their MOS tunneling current. Strained MOSFET can improve carries' mobility, which has been studied extensively. In the same time, MOS tunneling current in strained MOSFET is also studied by several groups [27-30]. However in this research, MOS tunneling current is treated as an unpleasant phenomenon, and very few study are done to use this MOS tunneling current. For example, MOS tunneling current can be a very competitive alternative for low power strain sensors because of its high resistivity.

In the dissertation, it is the first time that a strain sensor based on MOS tunneling current is made and characterized. Parameters like noise, drift and sensitivity of MOS tunneling current strain sensor are characterized. It is found that noise is very small when MOS devices are in the inversion region.

We perform both DC measurement and AC measurement for the characterization. We find that an AC method using lock-in amplifier is more efficient to reduce noise than normal DC method.

To study sensitivity, a computationally efficient model for MOS tunneling current is built. Other groups only study ECB tunneling current for MOS in inversion region, which is enough for current density study. It is found that both the ECB and the EVB tunneling current must be considered when calculating the sensitivity for high doping concentrations and high voltages. The model fits our experiment very well.

A RF resonator based on MOS tunneling current strain sensor is also made. The first try was not successful. However, some tips to improve the design for future research are learned from this first try.

### **1.3 Outline of Dissertation**

The research goals of this project are to characterize the properties of MOS tunneling sensors, solve problems hindering the performance of the MOS tunneling sensors and make a resonator based on the MOS tunneling current strain sensor as an application.

Chapter 2 introduces research history of tunneling current as well as theories of MOS tunneling current. Different types of MOS tunneling current are discussed, like Fowler-Nordheim tunneling, direct tunneling and trap-assist-tunneling. In this chapter, an approximation method to calculate tunneling probability, the WKB method, is elaborated, as well as other basic formulas for MOS tunneling current. This WKB method will be used in the modeling for direct tunneling in Chapter 5.

Chapter 3 discusses strain effect on Silicon and MOS tunneling

current. First, the silicon band structure is briefly introduced. Then, the basic theory of strain tensor and stress tensor are introduced. In the end, strain effect on silicon band structure is discussed.

Chapter 4 characterizes the MOS tunneling current strain sensors experimentally using DC and AC method. The demonstration device is a cantilever beam. The MOS tunneling current strain sensor is fabricated near the fix end of the cantilever beam. Strain is induced by bending the free end. In the DC experiment, a semiconductor parameter analyzer is used to apply DC voltage and measure the DC current. During the AC experiment, a lock-in amplifier is used to isolate the MOS tunneling current. The reason of using AC method is to reduce noise in a faster way, which is very important especially when band width is considered for a sensor. From the experiments, it is found that the noise of NMOS tunneling current strain sensor in inversion region is much less than others.

Chapter 5 discusses modeling for NMOS tunneling current strain sensor in inversion region, which MOS tunneling current comprises two parts. One is the ECB tunneling current, in which electrons tunnel from conduction band. Another one is the EVB tunneling current, in which electrons tunnels from valence band. Sensitivity is extensively studied by modeling. In this chapter, it also shows that substrate doping concentration has a very large influence on MOS tunneling current.

Chapter 6 explores one application of MOS tunneling current strain sensor, which is a longitudinal bulk acoustic RF resonator. In this chapter, we design, simulate, fabricate and test a 13 MHz longitudinal bulk acoustic RF resonator. The difficulties of the fabrication are discussed in this chapter. The

resonator does not work. The reasons that may lead the resonator to fail are analyzed, and some modifications for future design are proposed.

In the end, Chapter 7 does a summary of this dissertation as well as a proposal of future research.

## CHAPTER 2

### INTRODUCTION TO MOS TUNNELING CURRENT

#### **2.1 History of quantum tunneling studying**

This chapter gives a brief introduction of the history of quantum tunneling studying. Quantum tunneling is a phenomenon that a particle can penetrate a barrier which potential is higher than the particle's kinetic energy. Taking tunneling current as an example, the carrier (hole or electron) can surmount a potential barrier which is larger than its kinetic energy. This phenomenon is impossible in classic physics [18, 31].

After the discovery of natural alpha radioactivity in 1896, the law of exponential decay was established through the efforts of Elster, Rutherford, etc. [31, 32]. The theory of  $\alpha$ -radioactivity on the basis of quantum tunneling was proposed by Gamow in 1928. Classically, the particle confined to the nucleus lacks the energy to surmount the nucleus potential wall, but in quantum mechanics there is a probability at which a particle can tunnel out of the nucleus. Gamow solved a model potential for the nucleus by combining the attractive nuclear forces with the Coulomb repulsion and derived from a relationship between the half-life of the alpha-decay event process and the energy of the emission, the Geiger-Nuttall formula, which had been previously discovered empirically [32, 33]. At nearly the same time, the problem was also solved by Gurney and Condon qualitatively [32].

During the same period, tunneling was used to explain electron emission from cold metal by Fowler and Nordheim [34]. They proposed a one-dimensional model. Metal electrons are confined by a potential wall whose height is determined by the work function plus the Fermi energy, and the wall becomes triangle like and thinned with an applied high electric field. The electrons tunneling through the potential wall change with applied electric field. Along with this model, they came up with the famous Fowler-Nordheim equation [31],

$$J = AF^2 \exp\left(-\frac{\sqrt{2m_{eff}}}{\hbar} \frac{4}{3} \frac{(\Phi_B)^{3/2}}{qF}\right) \quad (2.1)$$

where  $\hbar$  is Planck's constant,  $q$  is electronic charge,  $F$  is electric field in the oxide,  $\Phi_B$  is barrier height, and  $m_{eff}$  is electron effective mass of the insulator.

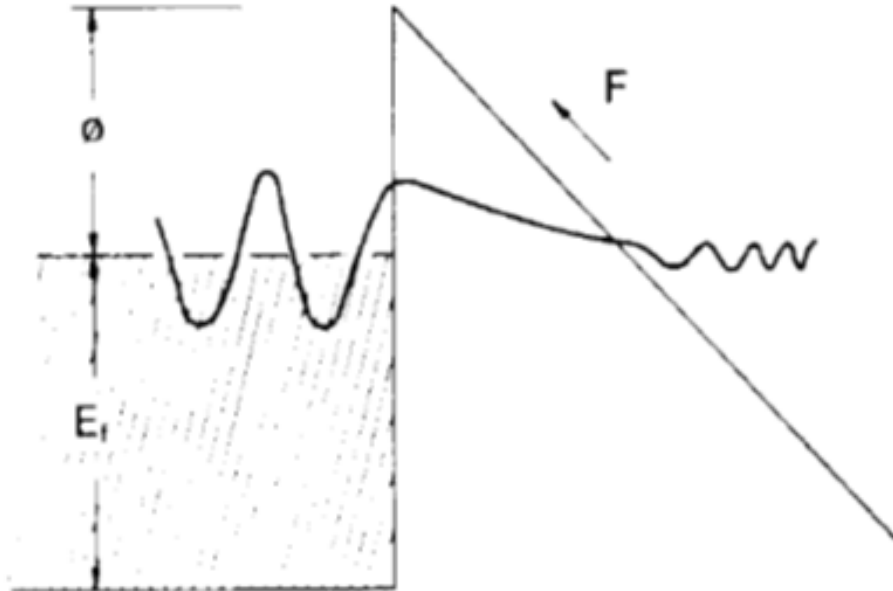


Figure 2.1 FN tunneling (Figure is from [31]).

During the 1930s and 1940s, tunneling was proposed to explain the transportation of electrical contacts between two solids. In 1930, Frenkel [35]

proposed that the anomalous temperature independence of contact resistance between metals could be explained in terms of tunneling across a narrow vacuum separation. Holm and Meissner verified that by experiment. In 1932, Wilson [36], Frenkel and Joffe [37] and Nordheim [38] applied quantum mechanical tunneling to the interpretation of metal-semiconductor contacts (rectifiers), but it was later proved to be wrong about the direction of rectifying in reality.

In 1950, with the development of diodes and transistors, the tunneling of electrons received new attention. In 1957 Esaki discovered the tunneling diode and this discovery proved the electron tunneling in solids conclusively [31]. The tunneling diode shows a negative resistance region as shown in Figure 2.2. This negative resistance can be interpreted by Figure 2.3. Both p and n type semiconductor are heavily doped to degeneration. When  $V_1$  is applied, electrons tunnel from n type conduction band to the p type valence band. When the voltage is increased to  $V_2$ , there is no energy level for electrons to tunnel, so the current decreases. As the voltage continuously increases, the tunnel diode works like a normal p-n diode.

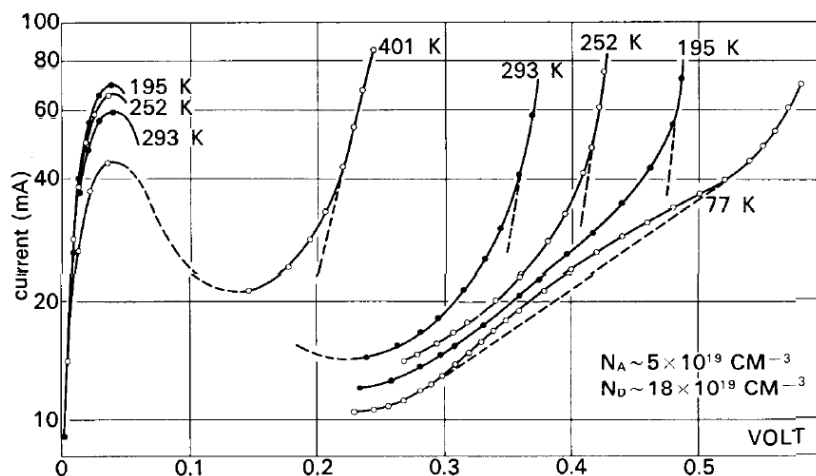


Figure 2.2 Current-Voltage relation of a tunneling diode [31].



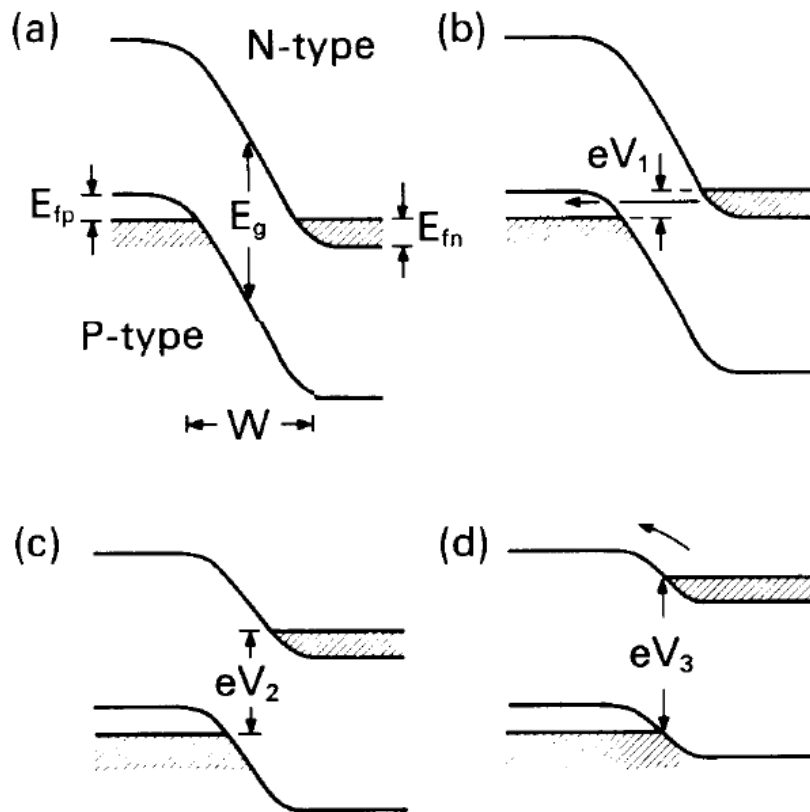


Figure 2.3 Band diagram of a tunneling diode at varies biases [31].

Tunneling was also researched in superconducting. In 1960, Giaever observed tunneling current between two conductors. At least one of the metals is a superconductor. This experiment enabled measurement of the energy gap in superconductors. This gap appears with Cooper pairs, and the gap plays an essential role in the BCS theory [39].

## 2.2 Different Types of Tunneling current in MOS capacitor

In the previous section, the history of research on quantum tunneling was reviewed briefly. This section will focus on MOS tunneling current. There are mainly three types of tunneling current in MOS capacitor, Fowler-Nordheim tunneling current, direct tunneling current and trap-assist-tunneling current.

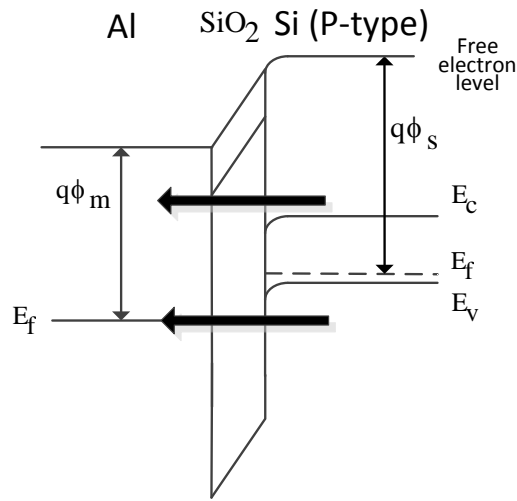
As mentioned in the previous section, Fowler and Nordheim give a complete theory of Fowler-Norheim tunneling. However it is complicated. Lenzlinger and Snow simplify the equation by ignoring the effects of finite temperature and image-force barrier lowering [40]. The simplified equation is,

$$J = \frac{q^3 F^2}{16\pi^2 \hbar \Phi_B} \exp\left(-\frac{\sqrt{2m_{eff}}}{\hbar} \frac{4}{3} \frac{(\Phi_B)^{3/2}}{qF}\right) \quad (2.2)$$

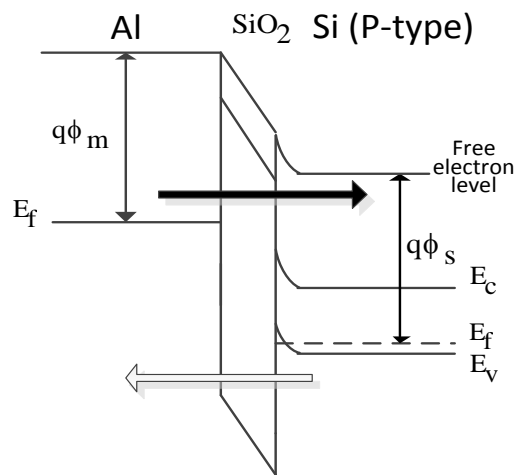
where  $\hbar$  is Planck's constant,  $q$  is electronic charge,  $F$  is electric field in the oxide,  $\Phi_B$  is barrier height, and  $m_{eff}$  is electron effective mass of the insulator. Section 2.3 will derive this equation for Fowler-Norheim tunneling current. The reason that Equation 2.2 is derived is to get deep understanding of MOS tunneling current. In the same time, some concepts from Fowler-Norheim tunneling current are used to derive models for direct tunneling current, like WKB method.

If the gate oxide is less than 4 nm, direct tunneling current will arise and become much larger than Fowler-Norheim tunneling current. As shown in the Figure 2.4 (a), when the gate voltage applied to the metal gate MOS devices is positive, there are two types of MOS tunneling current. One is ECB, where the electrons tunnel from the conduction band of silicon to aluminum; another one is EVB, where the electrons tunnel from the valence band of silicon to aluminum. When a negative gate voltage is applied to the gate as shown in Figure 2.4 (b), there are also two components of tunneling current. One is tunneling current from aluminum; another one is HVB, where the holes tunnel from the valence band of silicon to aluminum. The following chapters will focus on direct tunneling current, since the gate oxide of our MOS tunneling current strain sensor is less than 4 nm. Modeling of direct tunneling

current will be fully discussed in Chapter 5.



(a)



(b)

Figure 2.4 Illustration of direct tunneling in MOS structure. (a) positive bias;  
(b) negative bias.

The last type of MOS tunneling current is the trap-assist-tunneling current, which is shown in Figure 2.5. Electrons from the cathode first tunnel into the traps in the insulator layer, and then tunnel into the anode from the traps in the insulator layer. Traps are usually defects in the insulator layer.

During the trapping procedure, electrons usually exchange energy with insulator lattice through phonons. Large tunneling current at large gate voltage usually will introduce defects in the insulator layer, which will eventually break the insulator layer. Trap-assist-tunneling current is commonly recognized as one of the sources of noise in MOS tunneling current.

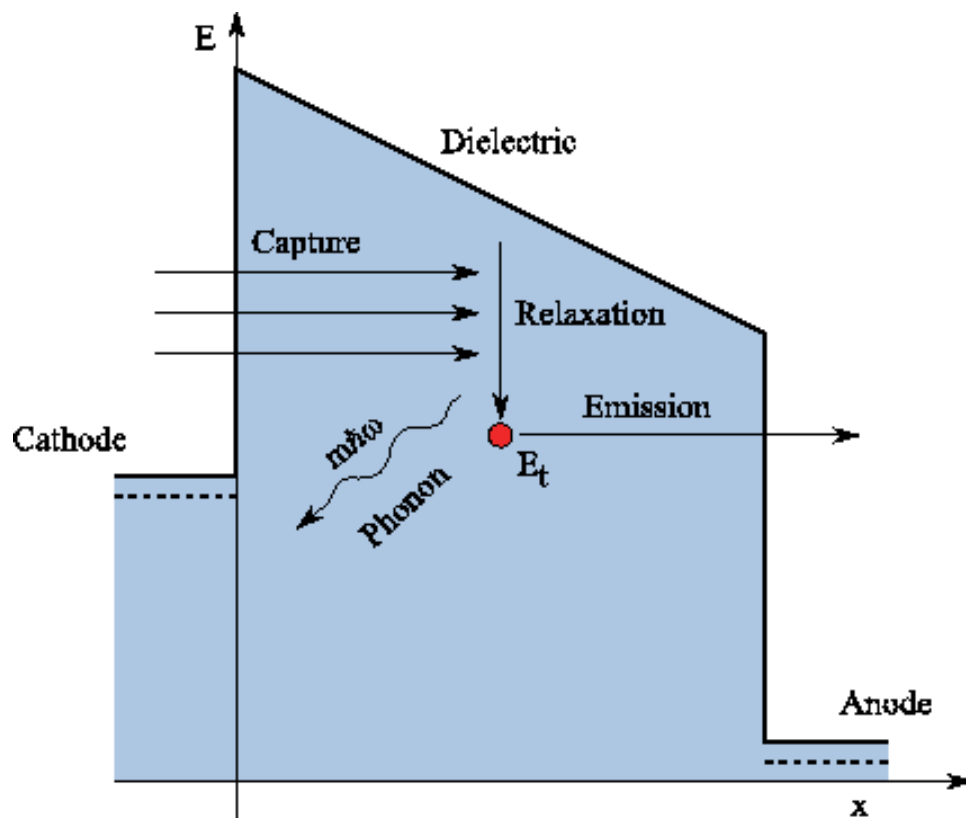


Figure 2.5 Schematic illustrating the Trap-assist-Tunneling current. The figure is from [41].

### 2.3 Derivation of Fowler-Nordheim tunneling current equation in MOS structure

This section will derive Fowler-Nordheim tunneling Equation 2.2. The purpose of this derivation is to understand MOS tunneling current deeper. The derivation for Equation 2.2 will also be partly adopted in the derivation of

formula for direct tunneling current. The Tsu and Esaki model and the WKB method will be used to formulate a general equation for Fowler-Nordheim tunneling current. After the general equation is derived, by setting temperature to 0 K to remove temperature influence, Equation 2.2 can be derived.

### 2.3.1 Tsu and Esaki model for Fowler-Nordheim tunneling current equation

The formula for Fowler-Nordheim tunneling can be derived by the Tsu and Esaki model [42]. In the Tsu and Esaki model, as shown in Figure 2.6, it is assumed that the net tunneling current is determined by difference between the current flow from side 1 to side 2 ( $J_{1 \rightarrow 2}$ ) and the current flow from side 2 to side 1 ( $J_{2 \rightarrow 1}$ ).

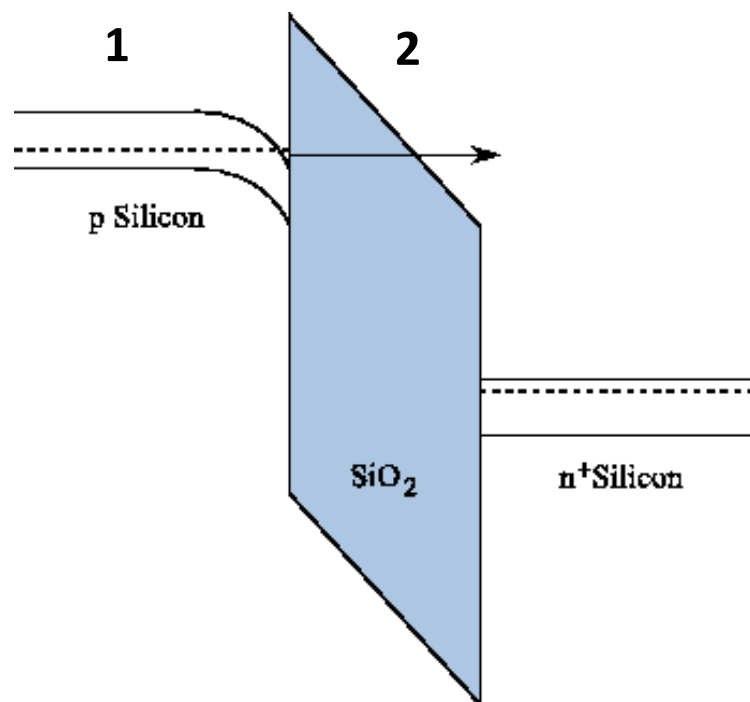


Figure 2.6 Schematic illustrating Fowler-Nordheim Tunneling current. The figure is from [41].

$$\begin{aligned}
dJ_{1 \rightarrow 2} &= qTC_1(k_x)v_xg_1(k_x)f_1(E)(1 - f_2(E))dk_x \\
dJ_{2 \rightarrow 1} &= qTC_2(k_x)v_xg_2(k_x)f_2(E)(1 - f_1(E))dk_x
\end{aligned} \tag{2.3}$$

The current density through the two interfaces depends on the perpendicular component of the wave vector  $k_x$ , the transmission coefficient  $TC$ , the perpendicular velocity  $v_x$ , the density of states  $g(k_x)$ , and the Fermi-Dirac distribution function  $f(E)$  at both sides of the barrier. For the Fowler-Nordheim tunneling, side 2 is the conduction band edge of  $\text{SiO}_2$ . Since  $\text{SiO}_2$  is an insulator,  $f_2(E)$  is almost 0 for energies above the conduction band edge of  $\text{SiO}_2$ . As a result,  $J_{2 \rightarrow 1}$  is ignored and only  $J_{1 \rightarrow 2}$  exists, which can be written as,

$$dJ = qTC(k_x)v_xg(k_x)f(E)dk_x \tag{2.4}$$

Here the density of states  $g(k_x)$  is

$$g(k_x) = \int_0^\infty \int_0^\infty g(k_x, k_y, k_z) dk_y dk_z \tag{2.5}$$

where  $g(k_x, k_y, k_z)$  denotes the three-dimensional density of states in the momentum space. Considering the quantized wave vector components within a cube of side length  $L$ ,

$$\Delta k_x = \frac{2\pi}{L}, \Delta k_y = \frac{2\pi}{L}, \Delta k_z = \frac{2\pi}{L} \tag{2.6}$$

The density of states within the cube can be written as

$$g(k_x, k_y, k_z) = 2 \frac{1}{\Delta k_x \Delta k_y \Delta k_z} \frac{1}{L^3} = \frac{1}{4\pi^3} \tag{2.7}$$

where the factor 2 comes from spin degeneracy. For the parabolic dispersion relation, the velocity and energy components in tunneling direction obey

$$v_x = \frac{1}{\hbar} \frac{\partial E}{\partial k_x} = \frac{\hbar k_x}{m_{eff}}, E_x = \frac{\hbar^2 k_x^2}{2m_{eff}}, v_x dk_x = \frac{1}{\hbar} dE_x \quad (2.8)$$

Then Equation 2.4 can be rewritten as

$$dJ = \frac{q}{4\pi^3 \hbar} TC(E_x) dE_x \int_0^\infty \int_0^\infty f(E_x) dk_y dk_z \quad (2.9)$$

Next, let's transfer Equation 2.6 from Cartesian coordinate to Polar coordinate, which is

$$k_r = \sqrt{k_y^2 + k_z^2}, \theta = \arctan\left(\frac{k_z}{k_y}\right) \quad (2.10)$$

$$k_y = k_r \cos(\theta), k_z = k_r \sin(\theta)$$

So the 3D dispersion equations can be rewritten as,

$$E_r = \frac{\hbar^2 (k_y^2 + k_z^2)}{2m_{eff}} = \frac{\hbar^2 k_r^2}{2m_{eff}} \quad (2.11)$$

$$E_x = \frac{\hbar^2 k_x^2}{2m_{eff}}$$

As  $\int_0^\infty dk_y \int_0^\infty dk_z = \int_0^{2\pi} d\theta \int_0^\infty k_r dk_r$ , current density can be rewritten

as

$$J = \frac{4\pi q m_{eff}}{h^3} \int_{E_{min}}^{E_{max}} TC(E_x) dE_x \int_0^\infty f(E) dE_r \quad (2.12)$$

$$= \frac{4\pi q m_{eff}}{h^3} \int_{E_{min}}^{E_{max}} TC(E_x) dE_x \int_{E_x}^\infty f(E) dE$$

Here  $E = E_r + E_x$ , so  $dE = dE_r$ . The lower limitation 0 of  $\int_0^\infty f(E) dE_r$  becomes  $E_x$  for  $\int_{E_x}^\infty f(E) dE$ . Putting the equation of Fermi-Dirac

distribution  $f(E) = \frac{1}{e^{\frac{E-E_f}{\kappa T}} + 1}$  into Equation 2.12 results in

$$\begin{aligned}
J &= \frac{4\pi q m_{eff}}{h^3} \int_{E_{min}}^{E_{max}} TC(E_x) dE_x \int_{E_x}^{\infty} f(E) dE \\
&= \frac{4\pi q m_{eff}}{h^3} \int_{E_{min}}^{E_{max}} TC(E_x) dE_x \int_{E_x}^{\infty} \frac{1}{e^{\frac{E-E_f}{k_B T}} + 1} dE \\
&= \frac{4\pi q m_{eff}}{h^3} \int_{E_{min}}^{E_{max}} TC(E_x) dE_x k_B T \left( -\ln \left( e^{\frac{E-E_f}{k_B T}} + 1 \right) \right) \Big|_{E_x}^{\infty} \quad (2.13) \\
&= \frac{4\pi q m_{eff} k_B T}{h^3} \int_{E_{min}}^{E_{max}} TC(E_x) \ln \left( e^{\frac{E_x-E_f}{k_B T}} + 1 \right) dE_x
\end{aligned}$$

Now the general equation for Fowler-Nordheim tunneling current has been derived. In the next section, the formula for the tunneling probability  $TC(E_x)$  will be solved based on the WKB method.

### 2.3.2 The WKB method

The WKB method is an approach to get an approximate solution for a linear partial differential equation with spatially varying coefficient. It is also known as the LG or Liouville–Green method [43]. In the tunneling cases, this spatially varying coefficient is the slowly varying potential in the gate oxide. In this section, general formula for the tunneling probability  $TC(E_x)$  will be deduced, which is then put into Equation 2.13 to get the final general Fowler-Nordheim tunneling current formula. The derivation can be found in any quantum mechanics book. It should be pointed out that WKB method is not only used for Fowler-Nordheim tunneling current equation, it is also used for direct tunneling current equation. This will be elaborated in the following sections.

For simplicity, as shown in Figure 2.7, only formula in one dimension is considered, though the WKB method can be applied to 3D. Electrons move along x direction. Here electrons tunnel from left to right. There are three regions in this schematic. Region 1 is the incident region, region 2 is the



forbidden region and region 3 is the transmitted region. Here  $E_f$  is the Fermi level,  $E_B$  is the work function,  $W$  is the thickness of the gate oxide,  $V_x$  is the linear varying potential in the gate oxide.  $E_z$  is forbidden energy at the position of  $Z$  along  $x$  direction.

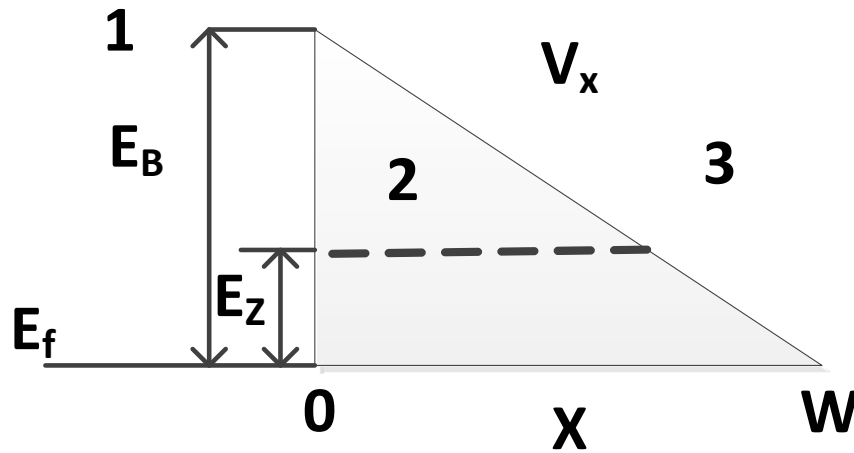


Figure 2.7 Schematic Illustrating for the WKB method.

Schrodinger equation can be solved under these boundary conditions.

The Schrodinger equation for an electron moving along  $x$  direction is

$$-\frac{\hbar^2}{2m} \frac{d^2\psi}{dx^2} + V(x)\psi(x) = E\psi(x) \quad (2.14)$$

Or

$$\frac{d^2\psi}{dx^2} + \frac{1}{\hbar^2} p^2(x)\psi(x) = 0 \quad (2.15)$$

where  $p(x)$  is the classical momentum along  $x$  direction,  $p(x) = \sqrt{2m(E - V(x))}$ .  $m$  is the effective mass along the tunneling direction, which is  $x$  direction here. For the forbidden region which is the gate oxide,  $V(x)$  varies linearly. It is easy to obtain the wave functions for the incident region and transmitted region respectively,

$$\psi_1(x) = \psi_{incident}(x) + \psi_{reflected}(x) = Ae^{ip_0x/\hbar} + Be^{-ip_0x/\hbar} \quad (2.16)$$

$$\psi_3(x) = \psi_{transmitted}(x) = Te^{ip_0x/\hbar} \quad (2.17)$$

where  $\psi_1(x)$  is the wave function in the incident region and  $\psi_3(x)$  is the wave function in the transmitted region.  $A$ ,  $B$  and  $T$  are the amplitudes of the incident, reflected and transmitted waves respectively.  $p_0 = \sqrt{2mE}$  is the momentum. The solution of the WKB method for the forbidden region assumes a form like,

$$\psi(x) = A(x)e^{iS(x)/\hbar} \quad (2.18)$$

where  $A(x)$  is the amplitude and  $S(x)$  is the phase, and they both are real functions. Substituting (2.18) into (2.15), we get

$$A\left[\frac{\hbar^2}{A} \frac{d^2\psi}{dx^2} - \left(\frac{dS}{dx}\right)^2 + p^2(x)\right] + i\hbar\left[2 \frac{dA}{dx} \frac{dS}{dx} + A \frac{d^2S}{dx^2}\right] = 0 \quad (2.19)$$

Only when both the real part and the imaginary part equal to 0, Equation 2.19 makes sense. Besides, since  $\hbar$  is a small number,  $\frac{\hbar^2}{A} \frac{d^2\psi}{dx^2}$  can be neglected. Thus,

$$\frac{dS}{dx} = \pm p(x) = \pm \sqrt{2m(E - V)} \quad (2.20)$$

$$2 \frac{dA}{dx} \frac{dS}{dx} + A \frac{d^2S}{dx^2} = 0 \quad (2.21)$$

Integrating Equation 2.20 gives

$$S(x) = \pm \int \sqrt{2m(E - V)} dx \quad (2.22)$$

Rewriting Equation 2.21 yields

$$2 \left( \frac{d}{dx} \ln A \right) p(x) + \frac{d}{dx} p(x) = 0$$

$$\xrightarrow{\text{yields}} \frac{d}{dx} (2 \ln A + \ln p) = 0 \quad (2.23)$$

$$\xrightarrow{\text{yields}} A = \frac{C}{\sqrt{|p(x)|}}$$

where  $C$  is a constant. Inserting Equation 2.22 and 2.23 into 2.18 indicates

$$\psi_{\pm}(x) = \frac{C_{\pm}}{\sqrt{|p(x)|}} \exp \left( \pm \frac{i}{\hbar} \int_{x_1}^x p(x') dx' \right) \quad (2.24)$$

Consider that  $E < V$ , which is known as the classically forbidden region, then (2.24) becomes,

$$\psi_2(x) = \frac{C}{\sqrt{|p(x)|}} \exp \left( -\frac{1}{\hbar} \int_{x_1}^x |p(x')| dx' \right) + \frac{D}{\sqrt{|p(x)|}} \exp \left( \frac{1}{\hbar} \int_{x_1}^x |p(x')| dx' \right) \quad (2.25)$$

Since  $\exp \left( \frac{1}{\hbar} \int_{x_1}^x |p(x')| dx' \right)$  increase exponentially with  $x$ , which is impossible in Physics, it is neglected for  $\psi_2(x)$ . Then,

$$\psi_2(x) = \frac{C}{\sqrt{|p(x)|}} \exp \left( -\frac{1}{\hbar} \int_{x_1}^x |p(x')| dx' \right) \quad (2.26)$$

Now the wave functions for three regions (incident region, forbidden region and transmitted region) are derived. The probability of tunneling (TC) can be expressed as

$$TC = \frac{v_{trans}}{v_{inc}} \frac{|\psi_{trans}(x)|^2}{|\psi_{inc}(x)|^2} = \frac{|T|^2}{|A|^2} \quad (2.27)$$

where the speed of incident ( $v_{inc}$ ) and the speed of transmitted ( $v_{trans}$ ) particles are equal. To get  $TC$ ,  $\psi_{inc}(x)$  and  $\psi_{trans}(x)$  must be solved. By using the continuity relations between incident region and forbidden region  $\psi_1(x_1) =$

$\psi_2(x_1)$  and  $\psi_1'(x_1) = \psi_2'(x_1)$  indicates

$$Ae^{ip_0x_1/\hbar} + Be^{-ip_0x_1/\hbar} = \frac{C}{\sqrt{|p(x_1)|}} \quad (2.28)$$

$$\frac{i}{\hbar}(Ae^{ip_0x_1/\hbar} - Be^{-ip_0x_1/\hbar}) = -\frac{C|p(x_1)|}{\hbar\sqrt{|p(x_1)|}} \quad (2.29)$$

Adding Equation 2.28 and 2.29, it yields

$$C = 2A\sqrt{|p(x_1)|}/(1 - \sqrt{|p(x_1)|}/ip_0) \quad (2.30)$$

Using the continuity relations between forbidden region and transmitted region  $\psi_2(x_2) = \psi_3(x_2)$  and  $\psi_2'(x_2) = \psi_3'(x_2)$  can obtain,

$$\frac{C}{\sqrt{|p(x_2)|}} \exp\left(-\frac{1}{\hbar} \int_{x_1}^{x_2} |p(x')| dx'\right) = Te^{ip_0x_2/\hbar} \quad (2.31)$$

$$-\frac{|p(x_2)|C}{\hbar\sqrt{|p(x_2)|}} \exp\left(-\frac{1}{\hbar} \int_{x_1}^{x_2} |p(x')| dx'\right) = \frac{ip_0}{\hbar} Te^{ip_0x_2/\hbar} \quad (2.32)$$

Inserting Equation 2.31 into 2.30 results in

$$\frac{T}{A} = \frac{2}{1 - \sqrt{|p(x_1)|}/ip_0} \sqrt{\frac{p(x_1)}{p(x_2)}} \exp(ip_0(x_1 - x_2)/\hbar) \exp\left(-\frac{1}{\hbar} \int_{x_1}^{x_2} |p(x')| dx'\right) \quad (2.33)$$

So the tunneling probability is

$$\begin{aligned} TC &= \left|\frac{T}{A}\right|^2 \\ &= \frac{4}{\frac{|p(x_2)|}{|p(x_1)|} + \frac{|p(x_1)||p(x_2)|}{p_0^2}} \exp\left(-\frac{2}{\hbar} \int_{x_1}^{x_2} \sqrt{2m(V(x) - E)} dx\right) \\ &\sim \exp\left(-\frac{2}{\hbar} \int_{x_1}^{x_2} \sqrt{2m(V(x) - E)} dx\right) \end{aligned} \quad (2.34)$$

Now the general tunneling probability from WKB method is obtained,

which is Equation 2.34. Next  $TC$  for Fowler-Nordheim tunneling current will be derived. For Fowler-Nordheim tunneling current, the potential barrier is like a triangle, so the tunneling probability for the Fowler-Nordheim tunneling current can be calculated. As shown in Fig. 2.7, it is assumed that the thickness of the barrier is  $W$ , the barrier height is  $E_B$ , the tunneling length of an energy of  $E_Z$  (which is relative to  $E_f$ ) is  $Z$ . Thus,

$$V(x) = \left(1 - \frac{x}{W}\right) E_B + E_f \quad (2.35)$$

So TC can be derived as

$$\begin{aligned} TC(E_Z + E_f) &= \exp\left(-\frac{\sqrt{8m}}{\hbar} \int_0^Z \sqrt{\left(1 - \frac{x}{W}\right) E_B - E_Z} dx\right) \\ &= \exp\left(-\frac{\sqrt{8m}}{\hbar} \left[-\frac{2W}{3E_B} \left(\left(1 - \frac{x}{W}\right) E_B - E_Z\right)^{3/2} \right]_0^Z\right) \\ &= \exp\left(\frac{\sqrt{8m}}{\hbar} \frac{2W}{3E_B} \left[\left(\left(1 - \frac{Z}{W}\right) E_B - E_Z\right)^{3/2} - (E_B - E_Z)^{3/2}\right]\right) \\ &= \exp\left(\frac{\sqrt{8m}}{\hbar} \frac{2W}{3E_B} \left[-(E_B - E_Z)^{3/2}\right]\right) \\ &\cong \exp\left(-\frac{2\sqrt{8mE_B}W}{3\hbar} \left(1 - \frac{3E_Z}{2E_B}\right)\right) \\ &= \exp\left(-\frac{2\sqrt{8mE_B}W}{3\hbar}\right) \exp\left(\frac{\sqrt{8mE_B}WE_Z}{\hbar E_B}\right) \\ &= T_0 \exp\left(\frac{E_Z}{E_0}\right) \end{aligned} \quad (2.36)$$

where

$$T_0 = \exp\left(-\frac{2\sqrt{8mE_B}W}{3\hbar}\right) \quad (2.37)$$

$$E_0 = \frac{\hbar E_B}{W\sqrt{8mE_B}}$$

Inserting Equation 2.36 into 2.13 gives

$$J = \frac{4\pi q m_{eff} k_B T}{h^3} T_0 \int_{E_{min}}^{E_{max}} \exp\left(\frac{E_x - E_f}{E_0}\right) \ln\left(e^{\left(\frac{E_x - E_f}{k_B T}\right)} + 1\right) dE_x \quad (2.38)$$

Here  $E_x - E_f = E_z$ . We assume  $E_{min} = -\infty$  and  $E_{max} = +\infty$ . We can obtain

$$J = \frac{4\pi q m_{eff} k_B T}{h^3} T_0 \int_{-\infty}^{+\infty} \exp\left(\frac{E_x - E_f}{E_0}\right) \ln\left(e^{\left(\frac{E_x - E_f}{k_B T}\right)} + 1\right) dE_x \quad (2.39)$$

Using the variable change  $u = e^{\left(\frac{E_x - E_f}{k_B T}\right)}$  and  $du = \frac{-1}{k_B T} u dE_x$  gives the current density,

$$\begin{aligned} J &= \frac{4\pi q m_{eff} k_B T}{h^3} T_0 (-k_B T) \int_{+\infty}^0 u^{-\frac{k_B T}{E_0} - 1} \ln(u + 1) du \\ &= \frac{4\pi q m_{eff} k_B T}{h^3} T_0 (k_B T) \int_0^{+\infty} u^{-\frac{k_B T}{E_0} - 1} \ln(u + 1) du \\ &= \frac{4\pi q m_{eff} k_B T}{h^3} T_0 (k_B T) \frac{\pi}{\left(\frac{k_B T}{E_0}\right) \sin\left(\frac{k_B T}{E_0} \pi\right)} \\ &= \frac{4\pi q m_{eff} (k_B T)^2}{h^3 \left(\frac{k_B T}{E_0}\right)^2} T_0 \frac{\left(\frac{k_B T}{E_0}\right) \pi}{\sin\left(\frac{k_B T}{E_0} \pi\right)} \end{aligned} \quad (2.40)$$

Since

$$\begin{aligned} T_0 &= \exp\left(-\frac{2\sqrt{8mE_B}W}{3\hbar}\right) \\ &= \exp\left(\frac{\sqrt{8m}2W}{\hbar3E_B} \left[-(E_B)^{\frac{3}{2}}\right]\right) \end{aligned} \quad (2.41)$$

and

$$E_B = qFW \quad (2.42)$$

where  $F$  is the electrical field in the insulator, Equation 2.40 can be written as

$$J = \frac{4\pi q m_{eff} \left(\frac{\hbar E_B}{W \sqrt{8m_{eff} E_B}}\right)^2}{\hbar^3 8\pi^3} \exp\left(-\frac{\sqrt{2m_{eff}}}{\hbar} \frac{4}{3} \frac{(E_B)^{3/2}}{qF}\right) \frac{\left(\frac{k_B T}{E_0}\right) \pi}{\sin\left(\frac{k_B T}{E_0} \pi\right)}$$

$$= \frac{q^3 F^2}{16\pi^2 \hbar E_B} \exp\left(-\frac{\sqrt{2m_{eff}}}{\hbar} \frac{4}{3} \frac{(E_B)^{3/2}}{qF}\right) \frac{\left(\frac{k_B T}{E_0}\right) \pi}{\sin\left(\frac{k_B T}{E_0} \pi\right)} \quad (2.43)$$

For the special case of  $T = 0$  K, the classic Fowler-Nordheim tunneling current formula without temperature influence can be obtained

$$J = \frac{q^3 F^2}{16\pi^2 \hbar E_B} \exp\left(-\frac{\sqrt{2m_{eff}}}{\hbar} \frac{4}{3} \frac{(E_B)^{3/2}}{qF}\right) \quad (2.44)$$

Now the derivation for the Fowler-Nordheim tunneling current is completed, but several things should be paid attention to,

- 1) The electrons in the emitted electrode are assumed to be free Fermi gas.
- 2) The barrier lowering due to the image force is neglected.
- 3) The effective mass in the formula is the effective mass in the forbidden region. Since the effective mass is related to energy which varies in the forbidden region slowly, it is usually averaged through the whole region.

## 2.4 Direct tunneling in MOS structure

Direct tunneling is a mechanism that the electrons tunnel directly into the other electrode instead of the conduction band of the insulator. Taking

MOS structure as an example, when the thickness of insulator ( $\text{SiO}_2$ ) is less than 4 nm, direct tunneling dominates. However when the thickness of insulator is more than 4 nm, Fowler-Nordheim tunneling current dominates. There are several different components of a direct tunneling current, depending on the gate voltage polarization and amplitude of voltages and the material of the conductors.

#### 2.4.1 Derivation of the direct tunneling formula

During the derivation of Fowler-Nordheim tunneling current formula, we use WKB method to calculate the tunneling probability which is only valid when the oxide layer is thicker than 4 nm. When the thickness of the oxide layer is less than 1 nm, the assumption that the barrier changes slowly, which is the fundamental assumption of the WKB method, may not be very accurate. For gate oxide thickness larger than 1 nm, we still can use WKB method for  $TC$ . There are also several alternative methods to derive the direct tunneling formula. The results from these methods are close and fit to the measurement well [44]. Here we only briefly introduce the transfer matrix method to calculate the tunneling probability.

The general direct tunneling current formula can also be derived by the Tsu and Esaki model. When deriving the FN tunneling formula, it is assumed that  $J_{2 \rightarrow 1}$  (the current from the conduction band of  $\text{SiO}_2$ ) can be ignored and obtain Equation 2.13. However for the direct tunneling,  $J_{2 \rightarrow 1}$  (the current from the conduction band of substrate) is kept, so the total net tunneling current is,

$$J = J_{2 \rightarrow 1} - J_{1 \rightarrow 2} = \frac{4\pi q m_{eff} k_B T}{h^3} \int_{E_{min}}^{E_{max}} TC(E_x) \ln \left( \frac{e^{\left(\frac{E_x - E_{f2}}{k_B T}\right)} + 1}{e^{\left(\frac{E_x - E_{f1}}{k_B T}\right)} + 1} \right) dE_x \quad (2.45)$$



where  $E_{f1}$  or  $E_{f2}$  is the Fermi level in the side 1 or 2. The next step is to find  $TC(E_x)$  using transfer matrix method. To apply transfer matrix method, the whole scattering barrier is partitioned into many small slab regions, and in every slab region the barrier is assumed constant so that the Schrodinger equation can be solved analytically. The transfer matrix between two neighboring slabs is obtained by applying the continuity of the wave functions and their derivatives at the boundaries, and the overall transfer matrix is obtained by multiplying all these transfer matrices. For example, a barrier shown in Figure 2.8 can be divided into small slabs. The wave functions of slab  $j$  and slab  $j+1$  are,

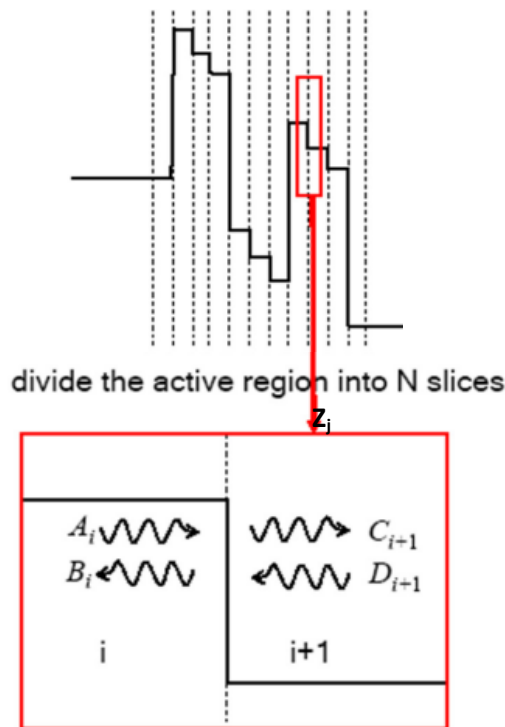


Figure 2.8 Transfer matrix method [45].

$$\psi_j(x) = A_j e^{ik_j x} + B_j e^{-ik_j x} \quad (2.46)$$

$$\psi_{j+1}(x) = C_{j+1} e^{ik_{j+1} x} + D_{j+1} e^{-ik_{j+1} x} \quad (2.47)$$

Using the continuity conditions,

$$\begin{aligned}\psi_j(Z_j) &= \psi_{j+1}(Z_j) \\ \frac{\partial\psi_j(Z_j)}{\partial Z} &= \frac{\partial\psi_{j+1}(Z_j)}{\partial Z}\end{aligned}\tag{2.48}$$

The transfer matrix  $T_j$  is

$$\begin{bmatrix} C_{j+1} \\ D_{j+1} \end{bmatrix} = T_j \begin{bmatrix} A_j \\ B_j \end{bmatrix}\tag{2.49}$$

Therefore, the overall transfer matrix  $TC$  is

$$TC = T_1 T_2 T_3 \cdots T_j \cdots T_{max}\tag{2.50}$$

It is obvious that we cannot get an analytic solution from transfer matrix method.

## 2.5 Summary

This chapter reviews the history of tunneling from the early 20 centuries' research on alpha radioactivity to recently extensive research on superconducting. Then MOS tunneling current is elaborated. First, three types of MOS tunneling current, Fowler-Nordheim tunneling current, direct tunneling current and trap-assist-tunneling current are introduced. Since the Fowler-Nordheim tunneling current and direct tunneling current are the main tunneling current in MOS capacitor, to deep understand these two types of tunneling current, the general tunneling current formula for these two types of tunneling current are derived. Two approaches to solve tunneling probability are discussed, which are WKB method and transfer matrix method. WKB method can be used in both Fowler-Nordheim tunneling current and direct tunneling current (which gate oxide thickness is larger than 1 nm and less than 4 nm), while transfer matrix method is mainly used in direct tunneling

current. The advantage of the WKB method is its simplicity and it is analytically expressed.

As shown in Chapter 4, the proposed experimental device's gate oxide is less than 4 nm, so direct tunneling current dominates. Therefore in Chapter 5, how to solve direct tunneling current based on this chapter as well as other factors like inversion layer energy quantization will be elaborated in detail.

## CHAPTER 3

### STRAIN EFFECTS IN SILICON

Chapter 2 discusses MOS tunneling current, especially the Fowler-Nordheim tunneling current and direct tunneling current. In this chapter, strain effects in silicon will be introduced. First, silicon band structure will be discussed, and then some concepts about stress and strain will be investigated. In the end, how strain affects band structure and eventually MOS tunneling current will be explored.

#### **3.1 Silicon band structure**

To calculate the band structure of a crystal like Silicon, the single electron Schrodinger equation must be solved [46],

$$H\psi(\mathbf{r}) = \left( \frac{p^2}{2m} + V(\mathbf{r}) \right) \psi(\mathbf{r}) = E\psi(\mathbf{r}) \quad (3.1)$$

where  $V(\mathbf{r})$  is the effective crystal potential,  $m$  is the effective mass.  $\mathbf{r}$  is the movement direction of electrons. The difference among different materials is  $V(\mathbf{r})$  and  $m$ . It is the single crystal silicon that is studied here. A crystal is constructed of replicas of lattice, which is an array of atoms or molecules repeating periodically in three dimensions. The lattice of silicon is face centered cubic (FCC) as shown in Figure 3.1. The FCC lattice is point symmetry, and there are a total of 48 symmetry operations. Since the arrangement of atoms influence effective crystal potential, the effective crystal

potential is also periodic and symmetric. Here we define lattice constant is  $a$ .

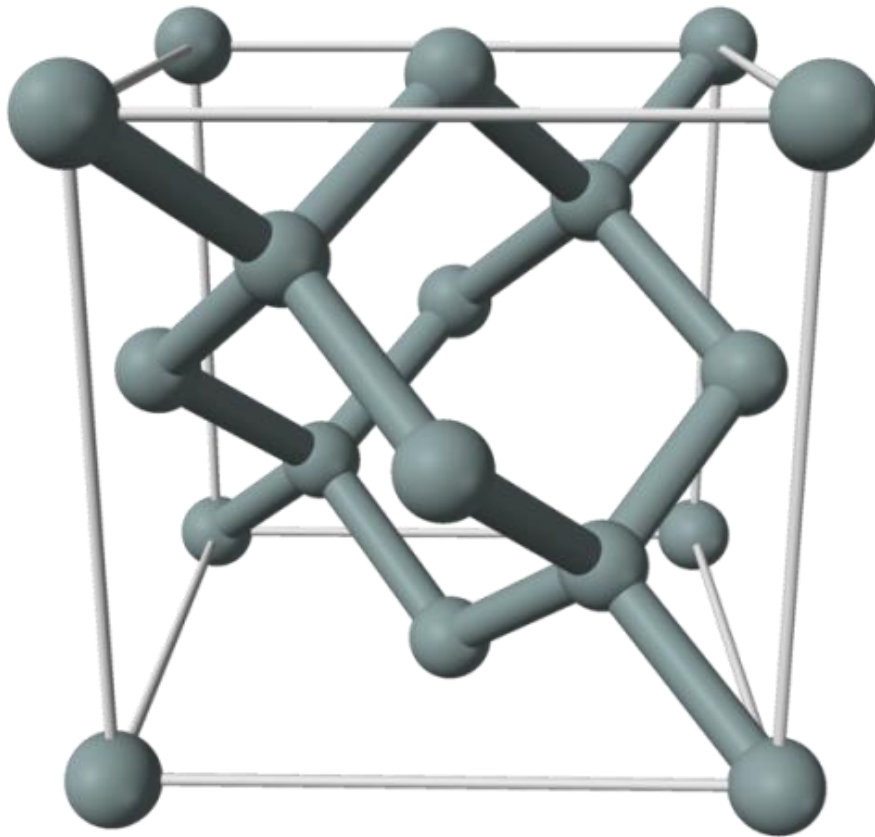


Figure 3.1 FCC lattice [47].

The band structure of Silicon solved by the Schrodinger equation is shown in Figure 3.2, which is constructed in the reciprocal space ( $k$  space) of the real lattice space. The reciprocal lattice for an FCC lattice is a body centered cubic (BCC) lattice. Due to the translation of the reciprocal lattice, it is conventionally only plotting the energy levels in the first Brillouin zone, which is defined as the space enclosed by the planes perpendicular to and bisecting the lines connecting a reciprocal lattice point and its neighbors. The first Brillouin zone of Silicon is shown in Figure 3.3. In the figure,  $\Gamma$  point is the center point of the first Brillouin zone. X point is located at  $2\pi/a(0, 1, 0)$

labeling the center of the square surfaces, and the direction from  $\Gamma$  to X is named as  $\Delta$ . L point is located at  $2\pi/a(0.5, 0.5, 0.5)$  labeling the center of the hexagonal surfaces, and the direction from  $\Gamma$  to L is labeled as  $\Lambda$ . Thus, the valley of valence band of Silicon is at the point of  $\Gamma$ , and its valley of conduction band is located between  $\Gamma$  and X along the direction of  $\Delta$ . Since there are six equivalent directions of  $\Delta$ , the valley of conduction band is six folded degenerated. The band gap is 1.12 eV for silicon [46, 48].

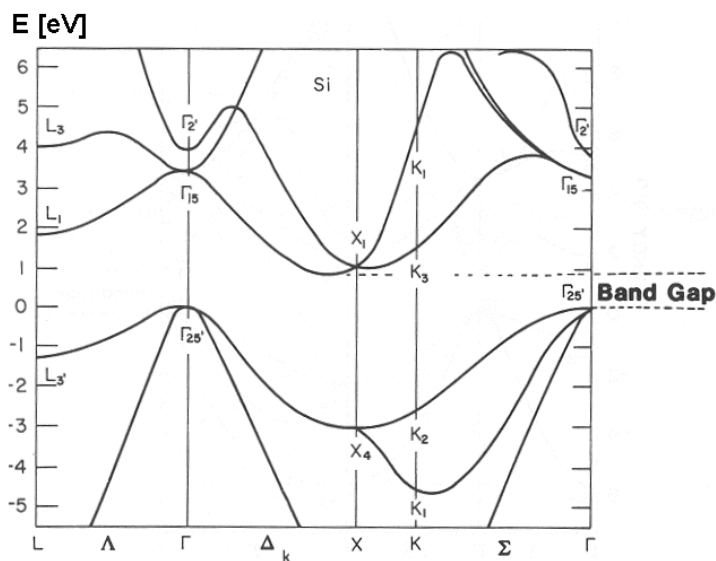


Figure 3.2 Band structure of Silicon [49].

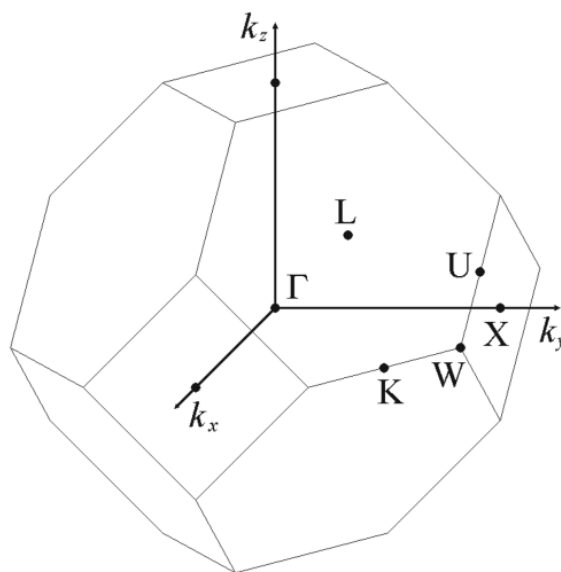


Figure 3.3 The first Brillouin zone of Silicon [50].

The band structure and the first Brillouin zone are based on the crystal lattice free of stress. The following sections will show how the stresses change the band structure of silicon.

### 3.2 Stress tensor

Tensors describe linear relations between two physical quantities. It can be a scalar, a vector or a matrix, depending on the order (rank) of the tensor. Stress is a force upon a unit area. The stress on an infinitesimal volume cube is shown in Figure 3.4.  $\sigma_{xx}$ ,  $\sigma_{yy}$  and  $\sigma_{zz}$  are normal stresses, which are along the direction of surface.  $\sigma_{xy}$  is defined as the shear stress along x direction at the surface which out-of-plane direction is along y direction. According to the force equilibrium principal,  $\sigma_{xy}=\sigma_{yx}$  and  $\sigma_{zy}=\sigma_{yz}$ .

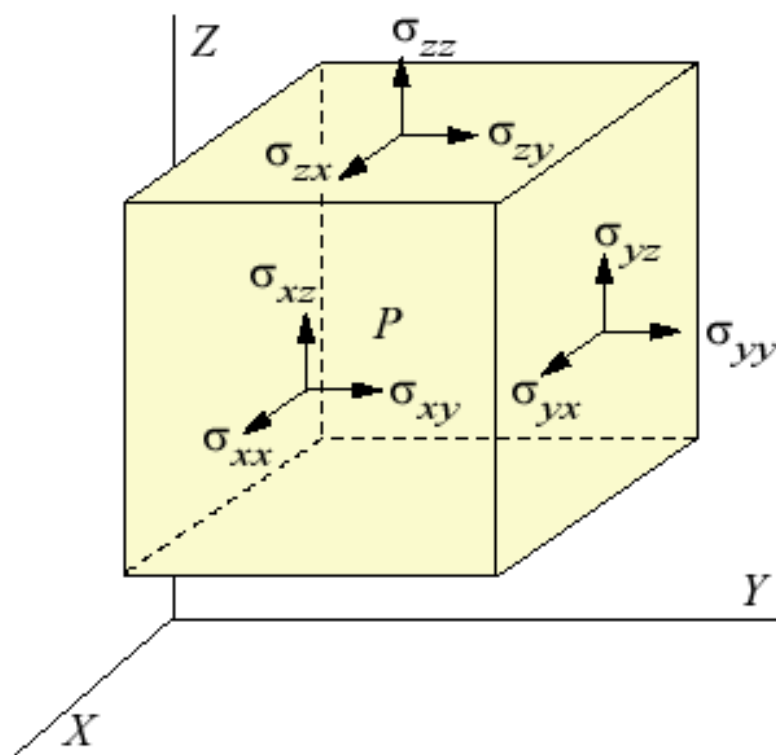


Figure 3.4 Stress components on the surfaces of an infinitesimal cube [51].

The Stress tensor is a second rank tensor of nine elements, including all of the normal stress and shear stress, which equals to,

$$\sigma = \begin{bmatrix} \sigma_{xx} & \sigma_{xy} & \sigma_{xz} \\ \sigma_{yx} & \sigma_{yy} & \sigma_{yz} \\ \sigma_{zx} & \sigma_{zy} & \sigma_{zz} \end{bmatrix} \quad (3.2)$$

### 3.3 Strain tensor

Strain is caused by deformation and representing the relative displacement between lattice point. The strain tensor is defined as following,

$$\varepsilon = \begin{bmatrix} \varepsilon_{xx} & \varepsilon_{xy} & \varepsilon_{xz} \\ \varepsilon_{yx} & \varepsilon_{yy} & \varepsilon_{yz} \\ \varepsilon_{zx} & \varepsilon_{zy} & \varepsilon_{zz} \end{bmatrix} \quad (3.3)$$

where  $\varepsilon_{xx}$ ,  $\varepsilon_{yy}$  and  $\varepsilon_{zz}$  represent the distortion of along the length, the other parts represent the distortion created by rotation. Like stress tensor, according to equilibrium principal,  $\varepsilon_{xy} = \varepsilon_{yx}$ ,  $\varepsilon_{xz} = \varepsilon_{zx}$  and  $\varepsilon_{yz} = \varepsilon_{zy}$ . Therefore, six elements should be enough to express stress tensor and strain tensor. We can rewrite the stress and strain tensors to,

$$\varepsilon = [\varepsilon_{xx} \quad \varepsilon_{yy} \quad \varepsilon_{zz} \quad \varepsilon_{yz} \quad \varepsilon_{zx} \quad \varepsilon_{xy}] \quad (3.4)$$

$$\sigma = [\sigma_{xx} \quad \sigma_{yy} \quad \sigma_{zz} \quad \sigma_{yz} \quad \sigma_{zx} \quad \sigma_{xy}] \quad (3.5)$$

In the linear elastic body, Hooke's law introduces a linear relation between stress and strain, so we can get a matrix expression for the relation between stress and strain, which is shown below,



$$\begin{bmatrix} \sigma_{xx} \\ \sigma_{yy} \\ \sigma_{zz} \\ \sigma_{yz} \\ \sigma_{zx} \\ \sigma_{xy} \end{bmatrix} = \begin{bmatrix} C_{11} & C_{12} & C_{12} & 0 & 0 & 0 \\ C_{12} & C_{11} & C_{12} & 0 & 0 & 0 \\ C_{12} & C_{12} & C_{11} & 0 & 0 & 0 \\ 0 & 0 & 0 & C_{44} & 0 & 0 \\ 0 & 0 & 0 & 0 & C_{44} & 0 \\ 0 & 0 & 0 & 0 & 0 & C_{44} \end{bmatrix} \begin{bmatrix} \varepsilon_{xx} \\ \varepsilon_{yy} \\ \varepsilon_{zz} \\ \varepsilon_{yz} \\ \varepsilon_{zx} \\ \varepsilon_{xy} \end{bmatrix} \quad (3.6)$$

where the coefficients  $C_{ij}$  are called elastic stiffness constants. The elastic stiffness constants are determined by materials. It has to be pointed out that there are only three independent components for the cubic crystal for its high symmetry. In most cases, it is more common to use the inverse of the elastic stiff tensor, the compliance tensor which is defined as,

$$S = \begin{bmatrix} S_{11} & S_{12} & S_{12} & 0 & 0 & 0 \\ S_{12} & S_{11} & S_{12} & 0 & 0 & 0 \\ S_{12} & S_{12} & S_{11} & 0 & 0 & 0 \\ 0 & 0 & 0 & S_{44} & 0 & 0 \\ 0 & 0 & 0 & 0 & S_{44} & 0 \\ 0 & 0 & 0 & 0 & 0 & S_{44} \end{bmatrix} \quad (3.7)$$

where  $S_{ij}$  is called the compliance. Therefore, the new relation between strain and stress is

$$\varepsilon = S\sigma \quad (3.8)$$

From this relation listed above, strain (or stress) can be calculated, if the stress (or strain) of a material is known.

A strain tensor can be decomposed into three separate tensors,

$$\begin{bmatrix} \varepsilon_{xx} & \varepsilon_{xy} & \varepsilon_{xz} \\ \varepsilon_{yx} & \varepsilon_{yy} & \varepsilon_{yz} \\ \varepsilon_{zx} & \varepsilon_{zy} & \varepsilon_{zz} \end{bmatrix} = \frac{1}{3} \begin{bmatrix} \varepsilon_{xx} + \varepsilon_{yy} + \varepsilon_{zz} & 0 & 0 \\ 0 & \varepsilon_{xx} + \varepsilon_{yy} + \varepsilon_{zz} & 0 \\ 0 & 0 & \varepsilon_{xx} + \varepsilon_{yy} + \varepsilon_{zz} \end{bmatrix} \\ + \frac{1}{3} \begin{bmatrix} 2\varepsilon_{xx} - (\varepsilon_{yy} + \varepsilon_{zz}) & 0 & 0 \\ 0 & 2\varepsilon_{yy} - (\varepsilon_{zz} + \varepsilon_{xx}) & 0 \\ 0 & 0 & 2\varepsilon_{zz} - (\varepsilon_{xx} + \varepsilon_{yy}) \end{bmatrix} \quad (3.9) \\ + \begin{bmatrix} 0 & \varepsilon_{xy} & \varepsilon_{xz} \\ \varepsilon_{yx} & 0 & \varepsilon_{yz} \\ \varepsilon_{zx} & \varepsilon_{zy} & 0 \end{bmatrix}$$

where the first one describes the effect of a hydrostatic strain, and the last two tensors represent the shear strain. For a cubic crystal, when a uniaxial stress is applied along  $\langle 100 \rangle$  axes, only the first type of shear strain is introduced. When there are stresses along  $\langle 110 \rangle$  or  $\langle 111 \rangle$ , the second type of shear strain exists plus first type of shear strain.

The hydrostatic strain only changes the volume of the cubic, the first shear strain changes the length of cubic along x, y and z, and the second shear strain rotates the axes. When only the first type shear strain is non-zero and  $\varepsilon_{xx} \neq \varepsilon_{yy} \neq \varepsilon_{zz}$ , the cubic deforms to an orthorhombic. If two of them equal, the orthorhombic degenerates to a tetragonal. When the second type shear strain exists and  $\varepsilon_{xy} \neq \varepsilon_{yz} \neq \varepsilon_{xz}$  the cubic becomes triclinic. However, if two of the shear strain are zero, the triclinic degenerates to an orthorhombic. For example, when a biaxial stress is applied, after decomposing the strain tensor, only the hydrostatic and the first type shear strain is not zero, plus  $\varepsilon_{xx} = \varepsilon_{yy}$ , so the cubic changes to an tetragonal. When a stress along  $\langle 110 \rangle$  is applied, all of the three strain tensors exist and  $\varepsilon_{yz} = \varepsilon_{xz}$ , so the cubic becomes the orthorhombic.

### 3.4 Strain effects on silicon band structure

If we know what kind of strain in silicon, how the band structure changes qualitatively can be predicted. It is possible to get a quantitative result for the band structure, but the solution requires group theory which is very complex [52], and therefore the quantitative solution will not be elaborated here. The following sections discuss two most common stresses, the biaxial stress and the  $\langle 110 \rangle$  uniaxial stress.

Assuming the biaxial stress is in the XY plane shown in Figure 3.5.

$\sigma_{xx} = \sigma_{yy} = T$  and the rest components equal to zero. According to the relation between strain and stress get,

$$\varepsilon_{xx} = \varepsilon_{yy} = (S_{11} + S_{12})T \quad (3.10)$$

$$\varepsilon_{zz} = 2S_{12}T \quad (3.11)$$

Thus the strain tensor becomes,

$$\varepsilon = \begin{bmatrix} \varepsilon_{xx} & 0 & 0 \\ 0 & \varepsilon_{xx} & 0 \\ 0 & 0 & \varepsilon_{zz} \end{bmatrix} \quad (3.12)$$

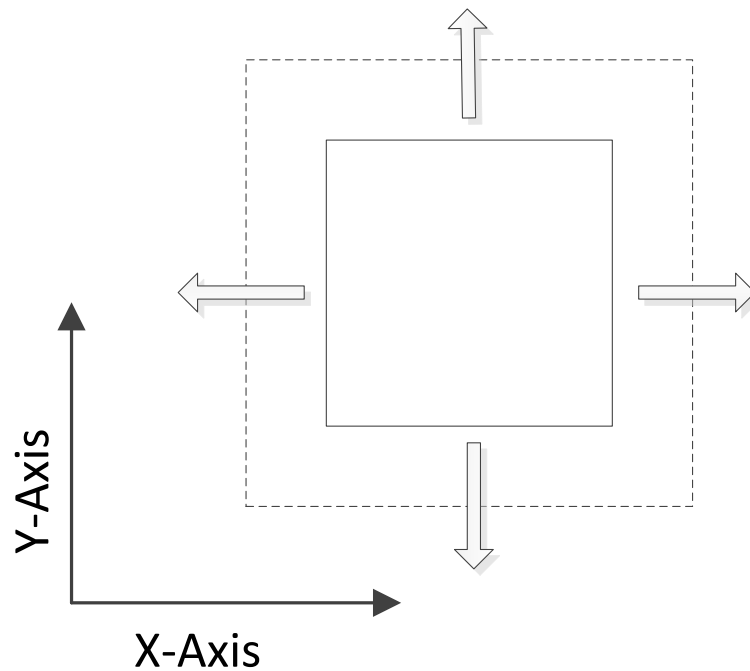


Figure 3.5 Biaxial stress .

It is obvious that only hydrostatic strain and the first shear strain exist, and the cubic lattice becomes tetragonal. For the hydrostatic strain, the shape doesn't change, but the distance between lattice points changes. As a result, the symmetry of the lattice does not change, as well as the symmetry of the

band structure, but the band gap changes. The shear strain degenerate the symmetry. The lattice constant along X and Y still equals, but the lattice constant along Z direction doesn't equal to lattice constant along X or Y, so the six degenerated  $\Delta$  valleys in the conduction band split into two groups,  $\Delta_2$  (longitudinal effective mass along  $\langle 001 \rangle$ ) and  $\Delta_4$  (longitudinal effective mass along  $\langle 100 \rangle$  and  $\langle 010 \rangle$ ). Besides the splitting of the conduction band, the degenerate heavy hole (HH) and light hole (LH) valence bands of Si also split into separate HH and LH bands. The band structure changing under a biaxial tensile stress is shown in Figure 3.6. For the conduction band,  $\Delta_2$  is lowered and  $\Delta_4$  is lifted. For the valence band, LH is lifted and HH is lowered.

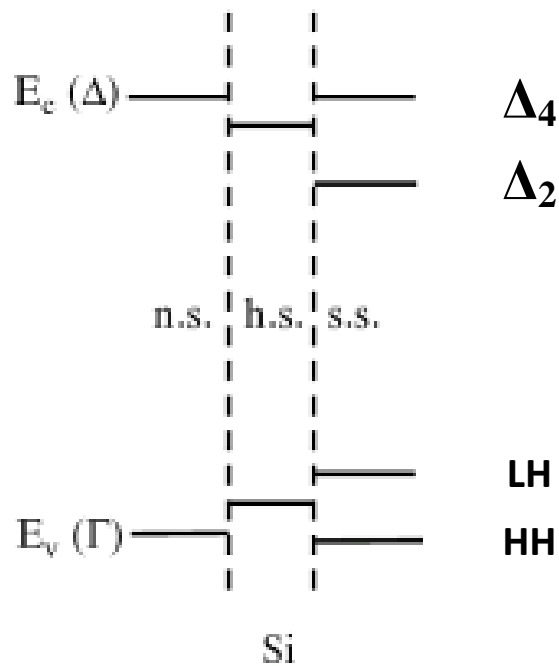


Figure 3.6 Band splitting of Si under biaxial tensile stress [52].

For a uniaxial stress along  $\langle 110 \rangle$  shown in Figure 3.7,  $\sigma_{xx} = \sigma_{yy} = \sigma_{xy} = T/2$  and the rest are zero. Thus

$$\begin{aligned}
\varepsilon_{xx} &= \varepsilon_{yy} = (S_{11} + S_{12})T/2 \\
\varepsilon_{xy} &= S_{44}T/2 \\
\varepsilon_{zz} &= S_{12}T
\end{aligned}
\tag{3.13}$$

Thus the strain tensor is,

$$\varepsilon = \begin{bmatrix} \varepsilon_{xx} & \varepsilon_{xy} & 0 \\ \varepsilon_{xy} & \varepsilon_{xx} & 0 \\ 0 & 0 & \varepsilon_{zz} \end{bmatrix}
\tag{3.14}$$

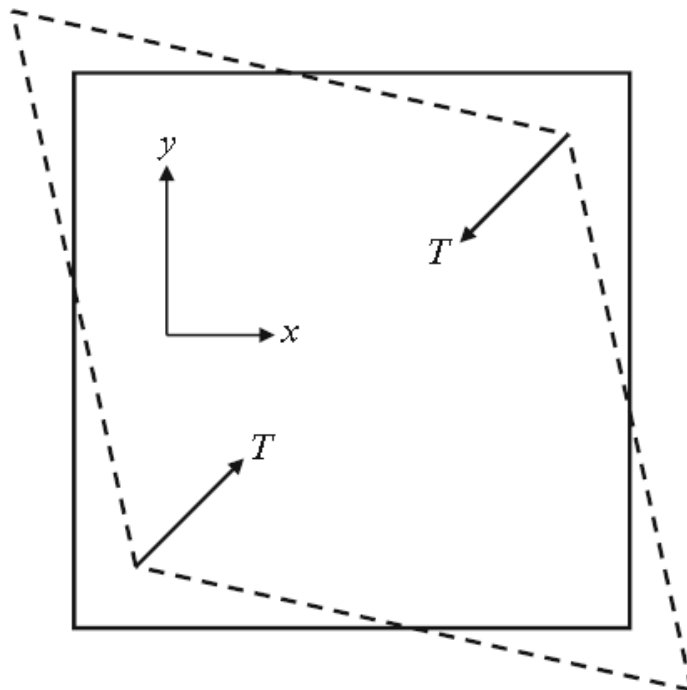


Figure 3.7 Uniaxial  $\langle 110 \rangle$  stress [52].

The uniaxial stress introduces all of the three strains. Due to lattice constant along X and Y still are the same, and the lattice constant along Z is different, it is not difficult to get a similar conclusion that the six degenerate conduction band valleys split into  $\Delta_2$  and  $\Delta_4$ , as well as the band gap changes and a splitting between the HH bands and LH bands. The band structure

under  $\langle 110 \rangle$  uniaxial compressive stress is shown in Figure 3.8.

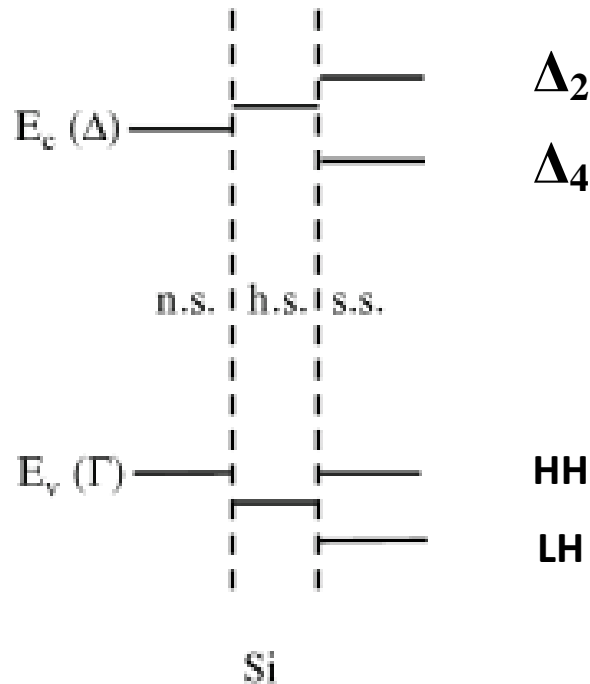


Figure 3.8 Band splitting of Si under uniaxial  $\langle 110 \rangle$  compressive stress [52].

Band warping is another phenomenon due to the strain. Taking the conduction band valleys of silicon for example, the  $\Delta_6$  valleys are at the axes from  $\Gamma$  to X. Since X is at the center of the square surface, the constant energy surface at the valleys should be symmetrical around the axes, which makes the constant energy surface an ellipsoid. When a  $\langle 110 \rangle$  uniaxial stress is applied to Si, the XY plane of the FCC lattice shifts from square to prismatic. The constant energy surface is no longer symmetrical around  $\langle 001 \rangle$ , so the constant energy surface becomes an ellipse with major and minor axes along  $\langle 110 \rangle$ . Figure 3.9 shows band warping under  $\langle 110 \rangle$  uniaxial stress.

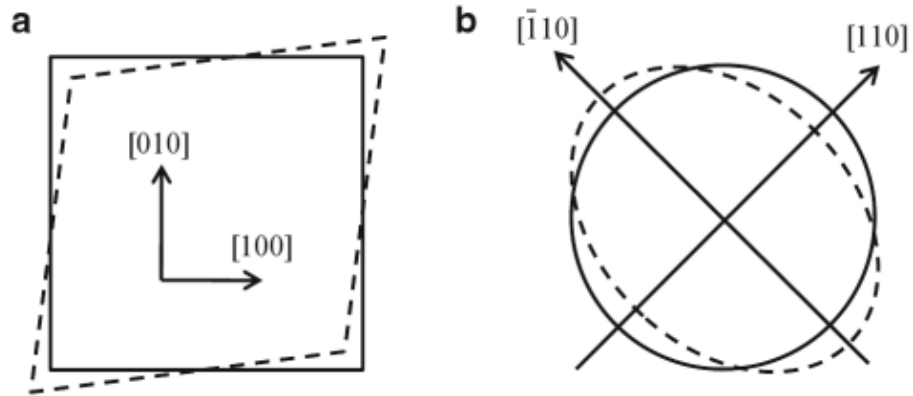


Figure 3.9 Uniaxial stress on constant energy surface. (a) Deformation under uniaxial  $\langle 110 \rangle$  stress. (b) Constant energy contour in (001) plane [52].

### 3.5 Summary

Chapter 3 discusses silicon lattice and band structure, stress tensor and strain tensor, and how stress changes silicon lattice and band structure. Because silicon has an FCC cubic crystal, silicon lattice poses high symmetry. The conduction band valleys are six folded degenerated. Strain in silicon diminishes this high symmetry. Every strain tensor has three different components. They are hydrostatic strain and two types of shear strain. Hydrostatic strain does not change symmetry, only changes band gap. Shear strain destroys symmetry, which then splits degenerated bands valleys and warp bands.

## CHAPTER 4

### EXPERIMENTS ON MOS TUNNELING CURRENT

#### **4.1 Introduction**

This chapter will experimentally investigate MOS tunneling current strain sensor. Two approaches are employed. One is DC method. Another one is AC method. For the DC method, a semiconductor parameter analyzer Hp4156c is used, which applies DC voltage and measures DC current. For the AC method, a function generator is used to generate an AC voltage which is applied to MOS tunneling strain sensor and a TTL reference signal to the lock in amplifier. The tunneling current of MOS tunneling strain sensor is then fed into a pre-amplifier and then a lock-in amplifier. The MOS tunneling current strain sensor is made on a cantilever, which is deformed by a micrometer at the free end, and the MOS capacitor is near the fixed end. The readout of the micrometer can be converted to strain.

As discussed in Chapter 3, uniaxial  $\langle 110 \rangle$  stress in silicon splits both conduction band valleys and valence band valleys, changing band gaps and warping band structure. Among these three effects, the first two influence tunneling current more than the band structure warping. The following sections will focus on uniaxial  $\langle 110 \rangle$  stress influence on tunneling current.

When the gate oxide is less than 4 nm and the gate voltage is lower than 2.5V, direct tunneling current dominates. When a positive gate voltage is



applied, the gate current comes from the electrons tunneling from Si to Al. There are two different kinds of tunneling current in gate current. One is electrons tunneling from conduction band, named as ECB tunneling current. Another one is electrons tunneling from valence band, named as EVB tunneling current.

As shown in Figure 2.4, ECB tunneling current is comprised of two parts, the two-fold degenerate  $\Delta_2$  group which longitudinal effective mass is along the  $\langle 001 \rangle$  direction and the four-fold degenerate  $\Delta_4$  group which transverse effective mass is along the  $\langle 001 \rangle$  direction. When NMOS is in inversion region, electrons limited in the 2D surface become quantized. Since the longitudinal effective mass is larger than the transverse effective mass,  $\Delta_2$  group has lower energy levels than that of  $\Delta_4$  group. Therefore, electrons are mainly located in the ground state of  $\Delta_2$ , which dominates ECB tunneling current. The MOS capacitor's tunneling current through the Silicon dioxide is mainly determined by the energy barrier height between the Silicon conduction band edge and the SiO<sub>2</sub> conduction band edge [28, 53, 54].

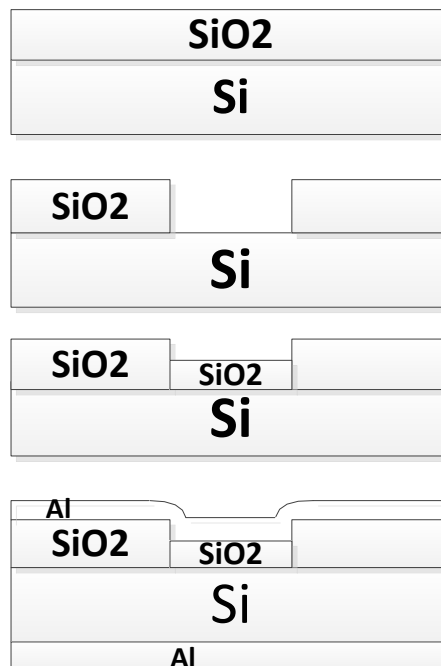
For EVB tunneling current, electrons in valence band are not confined in a 2D layer at the surface, so there is no quantization. Since valence band is full of electrons, especially when positively biased, there is no repopulation when uniaxial stress is applied. EVB tunneling current is also comprised of two components,  $J_{hh}$  and  $J_{lh}$ .  $J_{hh}$  has a heavy hole effective mass.  $J_{lh}$  has a light hole effective mass. Like ECB tunneling current, EVB tunneling current is also determined by barrier height which is the difference between SiO<sub>2</sub> conduction band and Si valence band, and out-of-plane effective mass.

When a negative voltage is applied on Al, the tunneling current is

composed by electrons tunneling from Al to Si and holes tunneling from Si to Al as shown in Fig. 2.4 (b). Because the barrier height of holes in Si is higher than that of electrons in Al, the tunneling current mainly depends on the electrons from Al. The tunneling current is then only determined by Al's work function. Uniaxial tensile strain causes Al's work function to decrease, so the tunneling current increases. Uniaxial compressive strain causes Al's work function to increase, so the tunneling current decreases.

#### 4.2 Fabrication and Measurement setup

Figure 4.1 shows the fabrication process of a cantilever beam with a tunneling oxide. The starting wafer is a heavily doped P-type (100) Silicon wafer, which is around 500  $\mu\text{m}$  thick. A 500 nm thick thermally grown oxide layer is patterned by wet etching. Then, a thin oxide layer (around 3.8 nm) is grown with an area of 1  $\text{mm}^2$ . Finally, Aluminum is sputtered and patterned as contacts. The length of the device is around 2 cm, and the width is 0.5 cm.



(a)



(b)

Figure 4.1 Fabrication process and the figure of MOS tunneling current strain sensor. (a). Fabrication process; (b). Picture of the device.

To minimize noise in MOS tunneling current, a very high quality gate oxide is desired. Four different methods are employed to grow gate oxide. They are PECVD, ALD, RTP and dry oxidation in furnace. Among these methods, it is found that dry oxidation in furnace provides the highest quality. At 800 °C, a heavily doped p type wafer grows 2.4 nm thick oxide in one minute. The uniformity of gate oxide can be characterized by an ellipsometer. Figure 4.2 shows that five positions on a wafer are chosen for the uniformity measurement. Table 3 gives the measurement result.

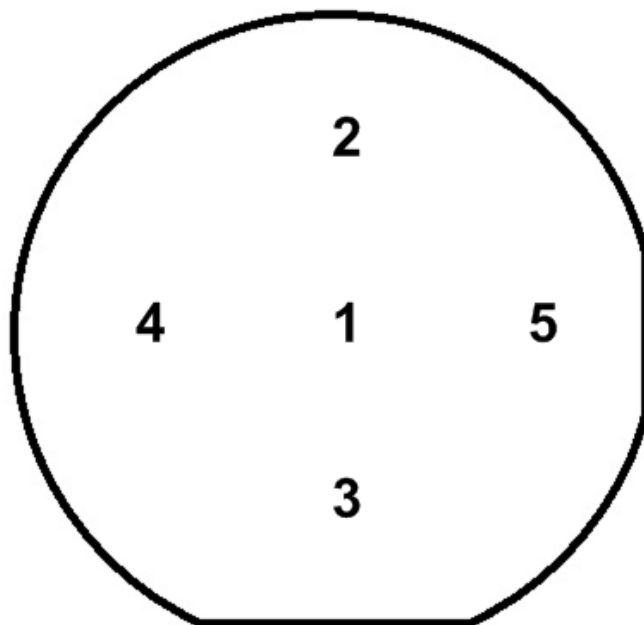


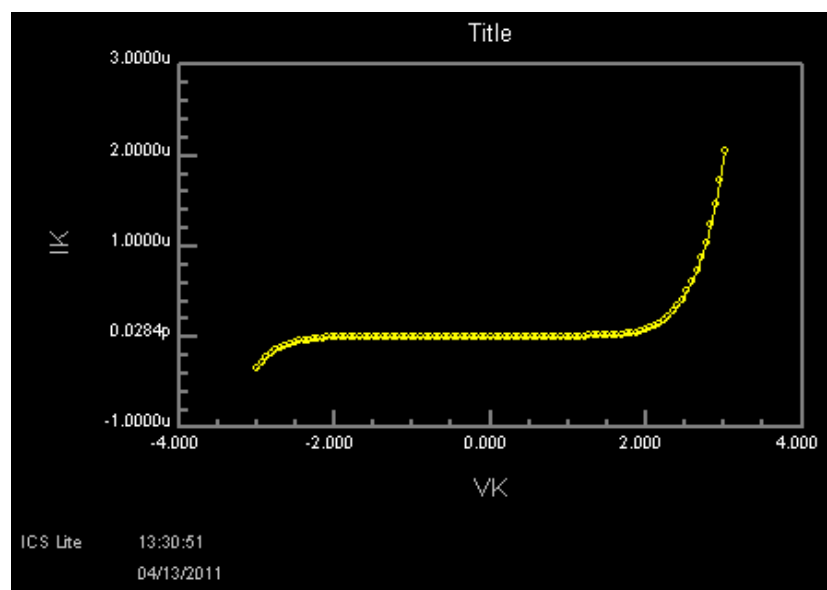
Figure 4.2 P type wafer for uniformity measurement using ellipsometer.

Table 3

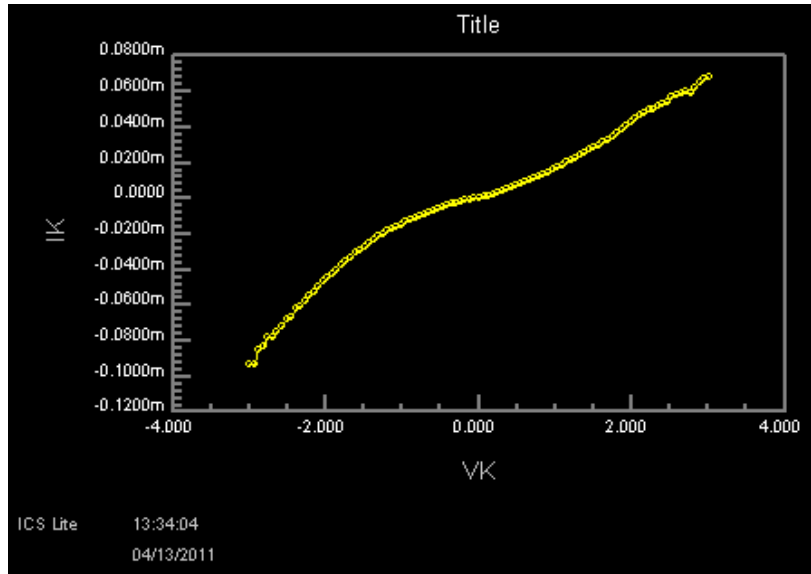
Uniformity measurement result

Positions	Thickness (nm)
1	2.38
2	2.45
3	2.39
4	2.41
5	2.39

One quick method to know whether the gate oxide is good or not is to measure current vs. gate voltage (IV curve). Figure 4.3 (a) shows a good gate oxide, which IV curve is more like log function. Figure 4.3 (b) shows a bad gate oxide, which IV is close to linear function. Besides, the current of good device is much smaller than the bad device. However, a device with a log function like IV curve does not mean the device has a very high quality gate oxide. Further measurement like noise characterization is needed, which will be discussed in later sections.



(a)



(b)

Figure 4.3 IV curve for MOS capacitor. (a). Good device; (b). Bad device.

Figure 4.4 shows the measurement setup. One end of the beam was glued to a metal stage by conductive epoxy, while the other end was deformed by scrolling a micrometer. The MOS capacitor is located in the fixed end. The micrometer positions are converted to strain. The tunneling current was recorded by an HP4156c Semiconductor Parameter Analyzer. Both uniaxial tensile strain and uniaxial compressive strain are in the  $\langle 110 \rangle$  direction.



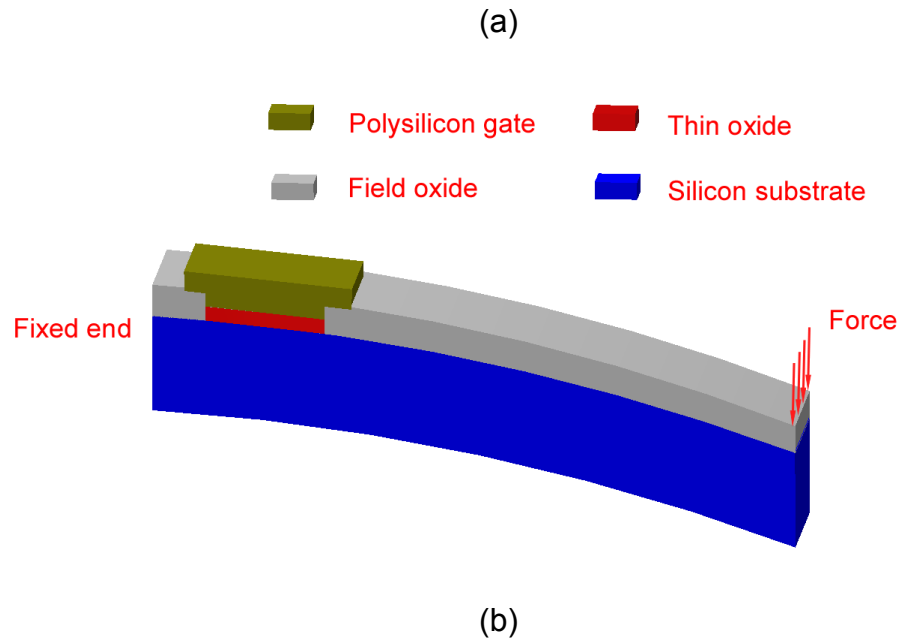


Figure 4.4 Photograph of measurement setup, and illustration of MOS tunneling current strain sensor using cantilever beam. The MOS device is near the fixed end. (a). Measurement setup; (b). Illustration of MOS tunneling current strain sensor using cantilever beam.

All the measurements were done by increasing the strain from 0% to 0.112% at the step of 0.016%, and then decreasing the strain from 0.112% to 0% at the step of 0.016%. During each step, there are 25 samples with a sampling time of 2 seconds.

### 4.3 DC experiments of strain effects on tunneling current

The results of tensile strain and compressive strain are given in the Table 4, Figures 4.5 & 4.6 and Figures 4.7 & 4.8 respectively. The blue solid lines are the measured tunneling currents, which drifts with time. Since in the beginning the currents decrease or increase sharply, only data captured after 50 seconds which is stable, is considered. To calculate noise and sensitivity, drift has to be removed which is shown as the red dot line. There are some

spikes in the measured results of 1V, 0.5V and -1V. These spikes appear at the time that the strains are changed, which are introduced by human body and are ignored in the analysis.

Table 4

Analysis of experiment data

Voltages (V)	Avg (nA)	SD (A)	$\frac{SD}{avg}$ (%)	$\frac{\Delta I_g}{I_g}$ 200 MPa (%)	GF	Drift rate (% per minute)
2 (tensile)	76.22	1.7E-11	0.022	-2.5	22.3	0.456
1.5	14.17	5E-12	0.03	-2.0	17.8	0.413
1	1.415	1.0E-13	0.007	-2.2	19	0.124
0.5	0.031	2.3E-13	0.7			-0.104
-1	0.147	3.6E-13	0.24	0.38	3.4	-0.52
2 (compressive)	75	2.0E-11	0.026	2.1	19	0.416
1	1.085	4.4E-13	0.04	1.8	16	0.608
0.5	0.039	1.5E-14	0.038	1.2	11.2	-0.464
-1	0.155	1.1E-13	0.07	-0.38	3.4	-1.48

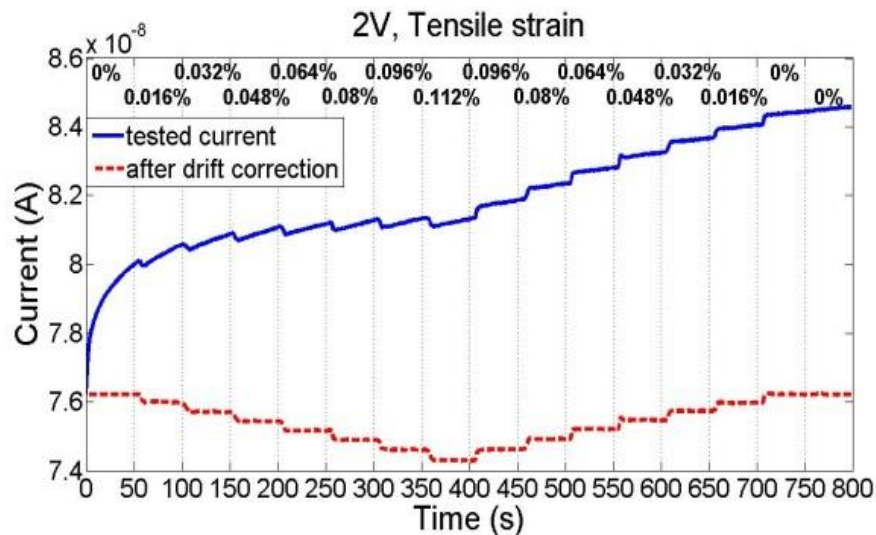
Table 4 analyzes noise (SD or SD/avg), sensitivity ( $\Delta I_g/I_g$  or GF) and drift. Here avg is the average tunneling current of 25 samples with a sampling time of two seconds at zero strain. SD is standard deviation of 25 samples with a sampling time of two seconds at zero strain. Drift which unit is % per minute is calculated from 50 seconds to 800 seconds. Drift shows that tunneling current changes slowly even when there is no strain. GF is the gauge factor which equals to  $\frac{\Delta I_g/I_g}{\varepsilon}$ , where  $\varepsilon = 0.112\%$ .

#### 4.3.1 Tensile strain

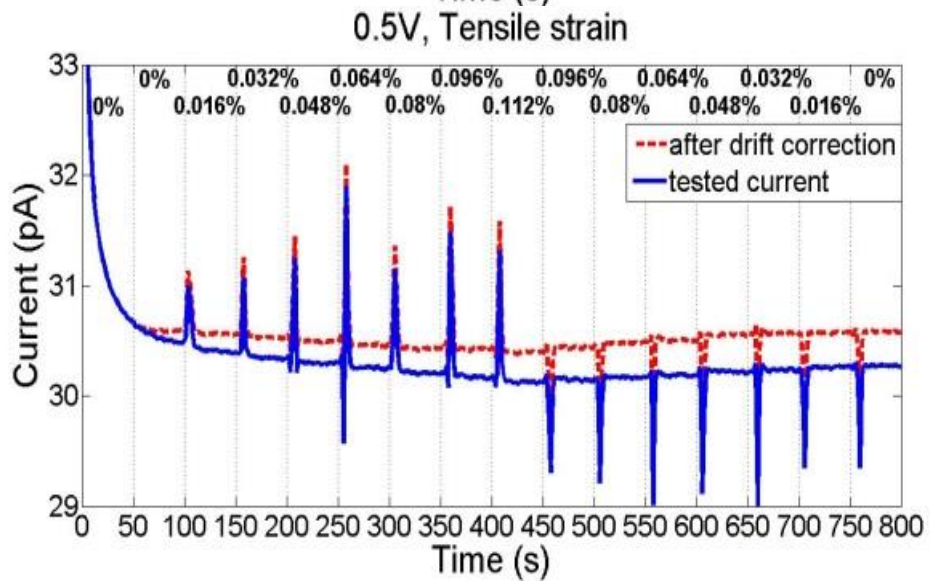
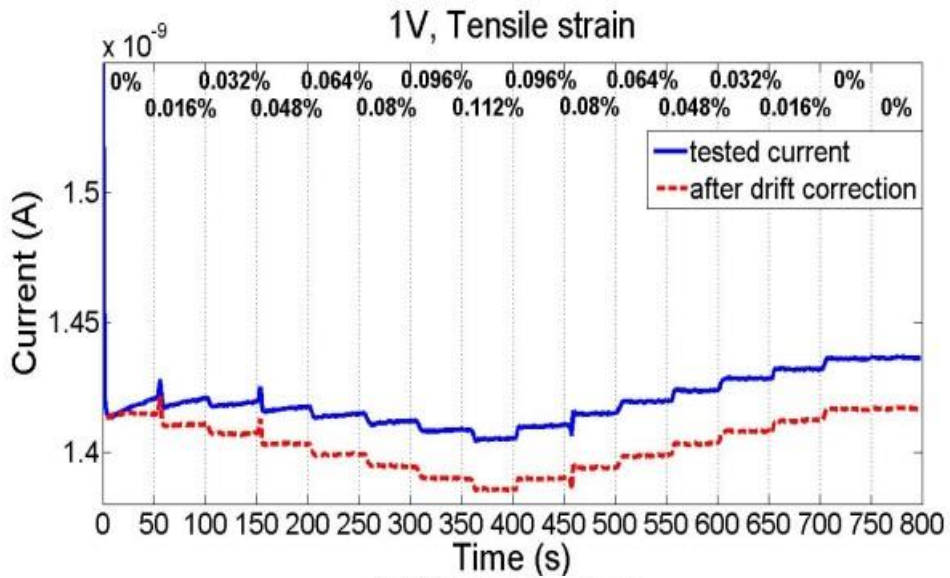
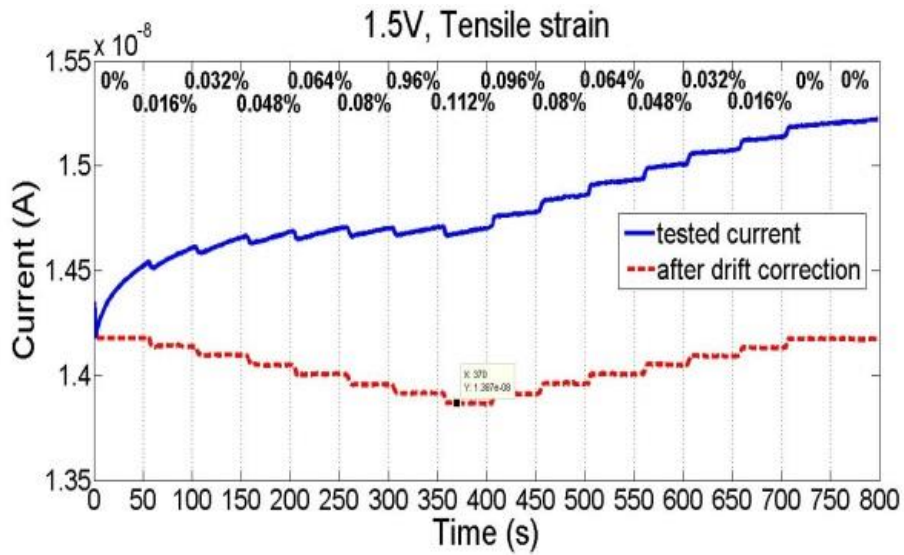
From the analysis in the Table 4 and Figure 4.5, it can be seen that tunneling current increases as gate voltage increases. The noise or SD decreases two orders of magnitude from 0.5V to 1V, and it keeps the same order of magnitude from 1V to 2V. SD/avg at 2V is 0.022%, which means a

strain induced current changing less than 0.022% at 2V cannot be measured. The sensitivity at 2V at the strain of 0.112% is -2.5%. Therefore, if minimum detectable strain at 2V equals to  $0.112\% / (2.5\% / 0.022\%)$ , which is 0.001%. Likewise, the minimum detectable strain at 1V is around 0.0005%. The minimum detectable strain at 0.5V and -1V are around 0.112%, which are large.

The current drifting is observed. Table 4 and Figure 4.5 show that the drift rate changes from negative to positives as gate voltage increases from 0.5V to 2V. From 1V to 2V of tensile experiment, it seems like drift rate increases. However, as find in compressive experiment, from 1V to 2V, drift rate decreases a little bit. Since the same device is used, the drift rate should show the same result, but it did not. Therefore, drift in tunneling current need more experiment to characterize.







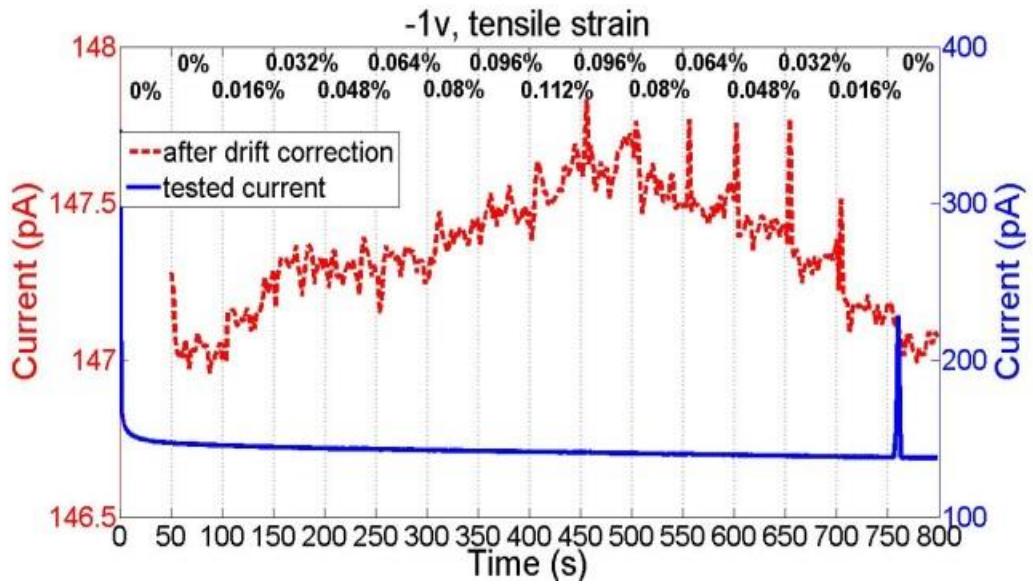
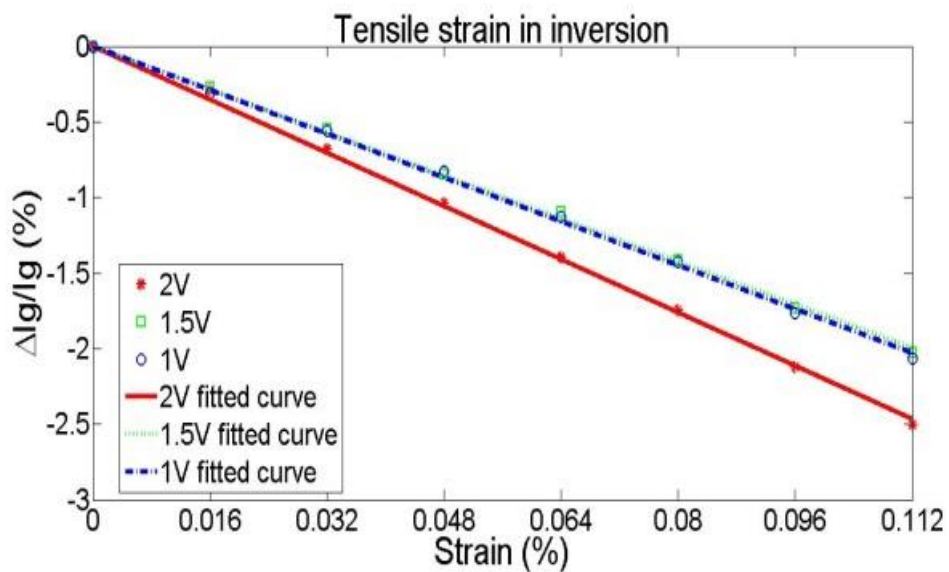


Figure 4.5 Tunneling current versus time at different gate voltages and different tensile strain.

In Figure 4.6, as the theories predict, tensile stress causes the MOS tunneling current to decrease at the positive voltage. In the other hand, tensile stress causes the MOS tunneling current from metal to Silicon to increase at the negative voltage. The sensitivity ( $\Delta I_g/I_g$ ) and gauge factor decreases from 1V to 1.5V, but increases from 1.5V to 2V.



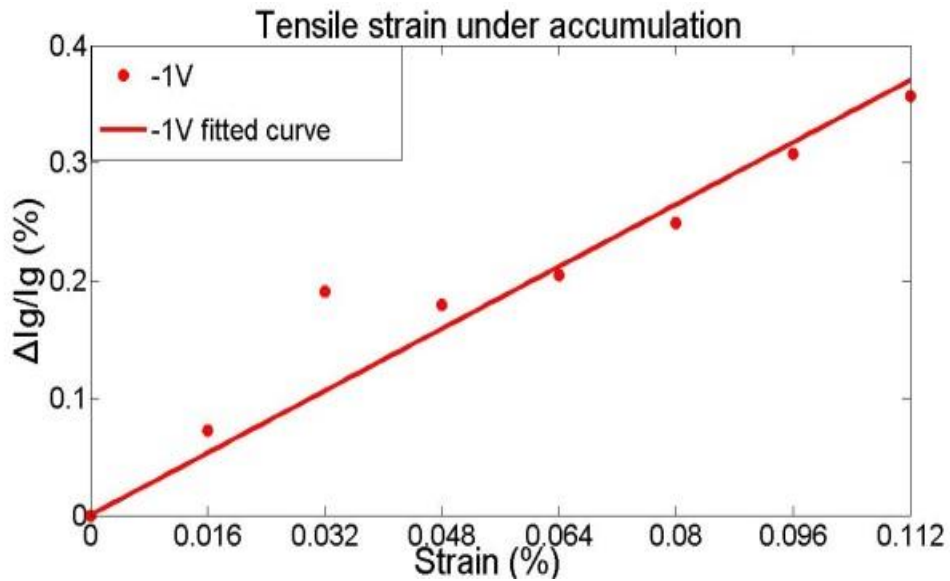
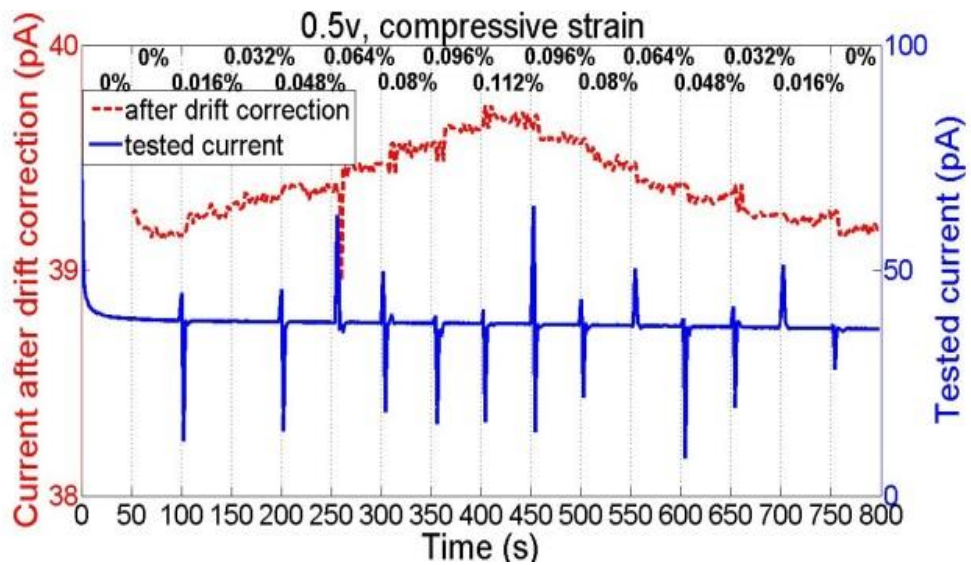
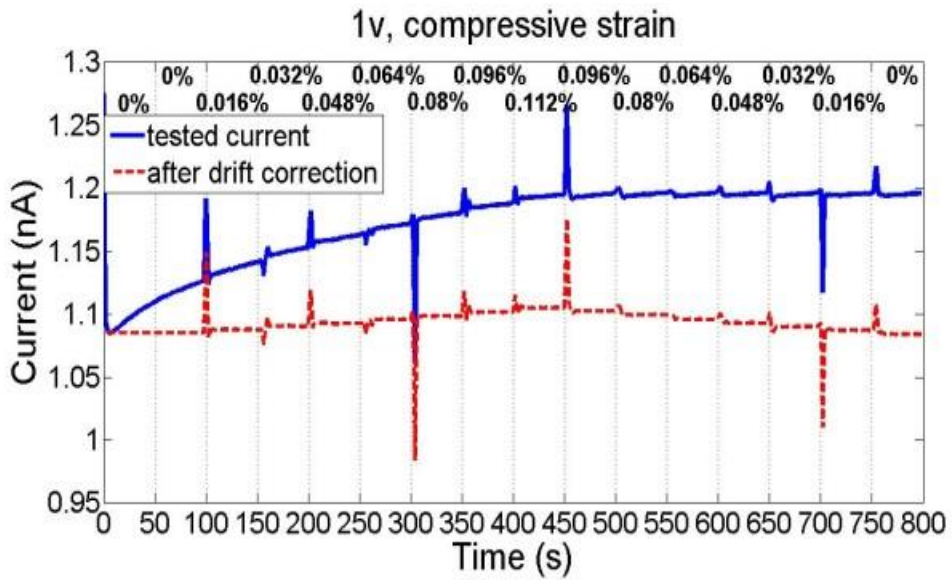
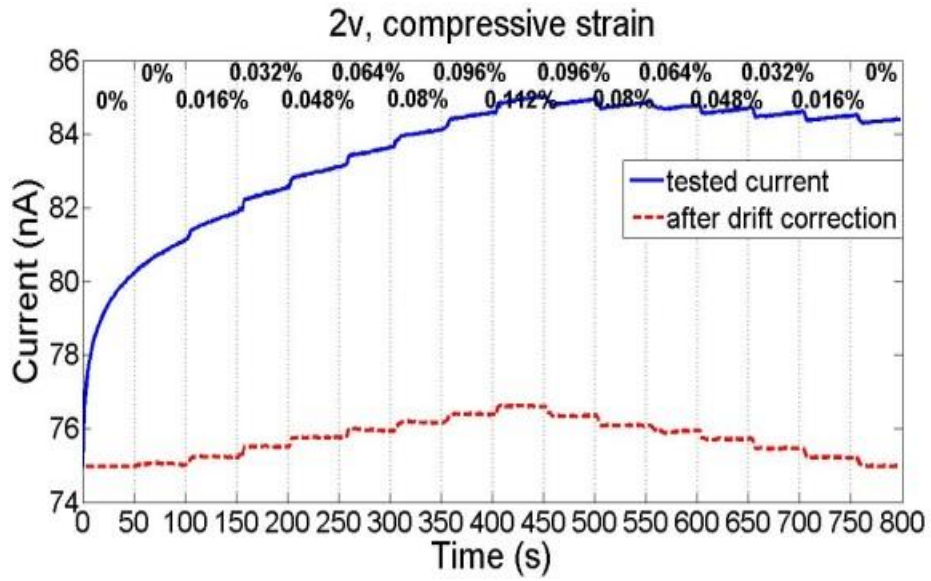


Figure 4.6 Tunneling current change versus tensile strain.

#### 4.3.2 Compressive strain

Figures 4.7 & 4.8 show that the compressive stress responses are contrary to the tensile stress responses. Compressive stress causes MOS tunneling current to increase at positive gate voltages, while decrease at negative gate voltages.

Since the same device is used for both tensile and compressive stress measurement, the SD should be close to those of tensile strain. However, the SD at 1V is four times larger than that of tensile strain, while the SD at 0.5V is ten times smaller and the SD at -1V is three times smaller. The difference may come from the electrode contact or environment like temperature, since the compressive strain measurement was conducted at different time. Sensitivity at 2V and 1V are better than those at 0.5V and -1V.





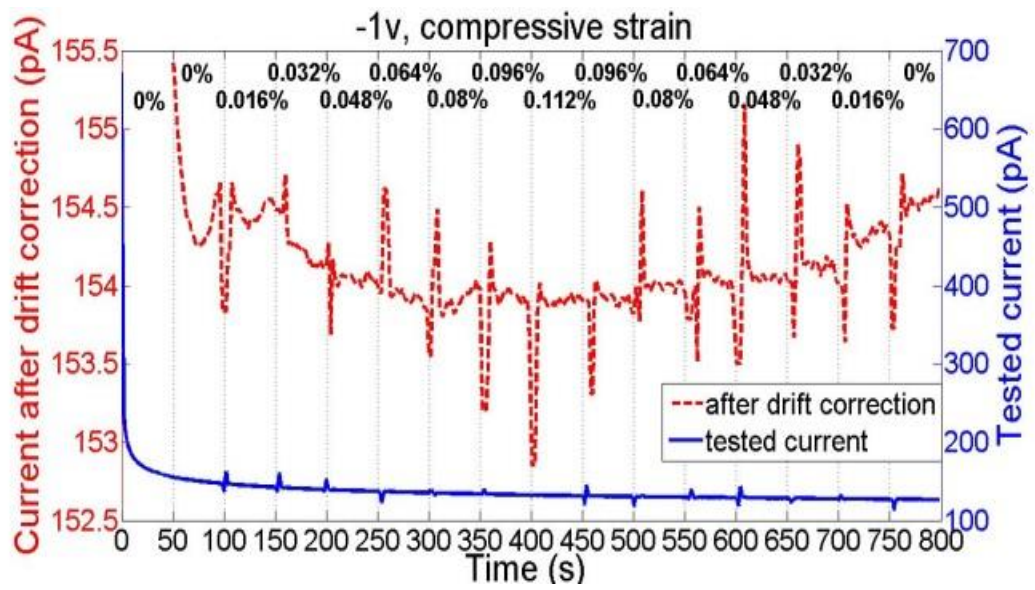
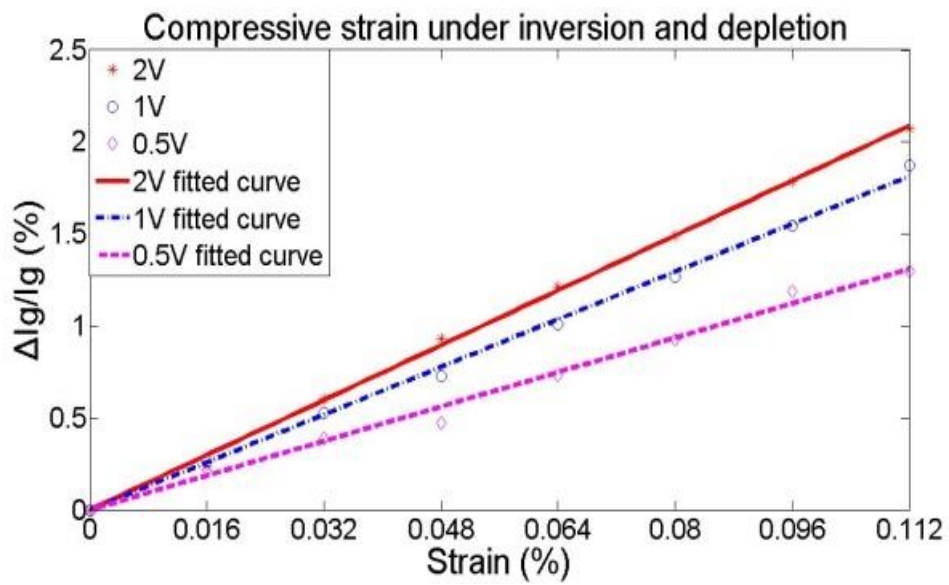


Figure 4.7 Tunneling current versus time at compressive strain.



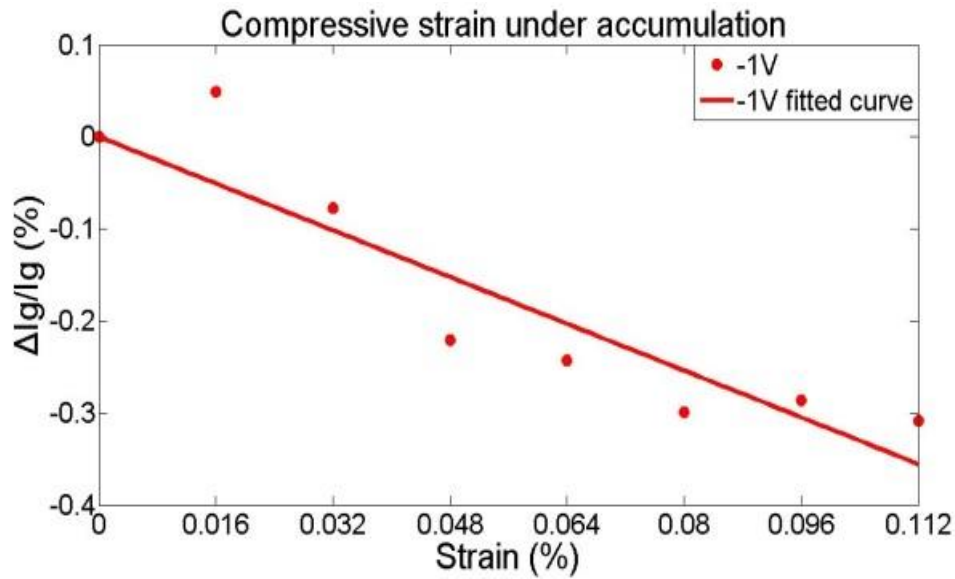


Figure 4.8 Tunneling current change versus compressive strain.

### 4.3.3 Discussion

As part of the experiment, noise, sensitivity and drift of MOS tunneling current strains sensor were studied. Noise of positively biased tunneling current is less than that of negatively biased tunneling current. Besides, noise decreases as gate voltage increases. Tensile stress decreases positively biased MOS tunneling current, and increases negatively biased MOS tunneling current. Compressive stress shows an opposite effect on MOS tunneling current. Sensitivity of MOS tunneling current strain sensor increases as gate voltage increases. However, under tensile stress, sensitivity of positively biased MOS tunneling current strain sensor decreases a little and then increases. Drift does not show a clear pattern from the experiment, which requires further study.

Since it is preferred for noise as small as possible, it is better to let MOS tunneling current strain sensor work in inversion region. The following sections will show the building of models for ECB tunneling current and EVB

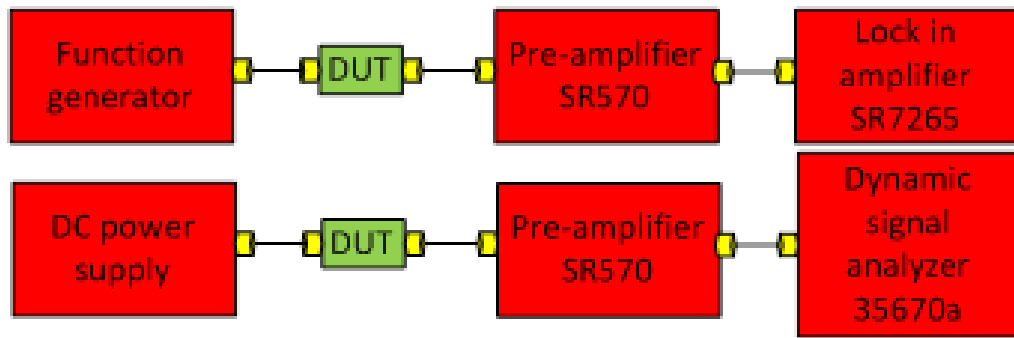
tunneling current to theoretically study sensitivity of MOS tunneling current strain sensor in inversion region.

#### **4.4 AC experiments of strain effects on tunneling current**

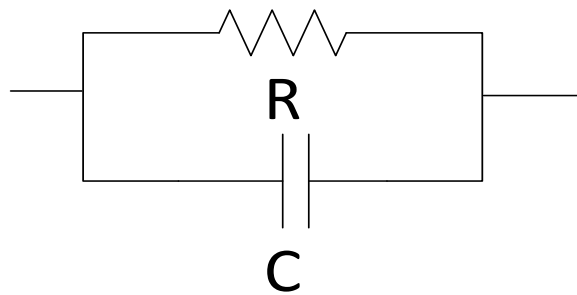
During the DC experiment of strain effects on tunneling current, strain was measured by measuring the strain-induced tunneling current changing through a Metal-Oxide-Semiconductor sandwich from a DC voltage. To overcome the electronic noise, substantial averaging was utilized. In this section an improved method of measuring the strain from the tunneling current is demonstrated in which an AC signal is utilized, and the AC current is measured. This approach substantially reduces the noise by avoiding the  $1/f$  noise. The optimal conditions for the AC technique are to use a high frequency to avoid  $1/f$  noise and a low DC bias. The MOS tunneling current strain sensor used to compare the performance has a 2.3 nm thick  $\text{SiO}_2$  gate oxide. To compare the performance, both DC method and AC method are performed. Only uniaxial  $\langle 110 \rangle$  tensile stress at positive bias is studied, which is enough to compare the performance to DC method. The way to apply stress to the device is the same as Figure 4.4.

##### **4.4.1 The principle of AC measurement**

The setup of the AC measurement is shown in Figure 4.9. A function generator is used to generate a sine wave AC voltage and a TTL reference signal. The AC voltage is applied to the device. Tunneling current from the device is fed into a pre-amplifier and lock-in amplifier. The silicon cantilever is deformed by a micrometer at the free end, and the micrometer positions are converted to strain.



(a)



(b)

Figure 4.9 (a) The top one is the setup for strain measurement and the bottom one is the setup for noise spectrum measurement. (b) The equivalent circuit for a MOS tunneling sensor.

A lock in amplifier is an efficient tool to extract signal from noise. The noise reduction depends on the bandwidth (time constant,  $\tau$ ) of low pass filter and the modulation frequency. The general principal of lock in amplifier can be described by the following equations. The equivalent circuit of the MOS tunneling device is a RC network in parallel (Figure 4.9(b)), so the signal from the preamplifier and the reference from the function generator are,

$$V_s = V_0 \cos(\omega_0 t) + V_1 \sin(\omega_0 t) + \delta_t \quad (4.1)$$



$$V_{ref} = \cos(\omega_0 t + \phi) \quad (4.2)$$

where  $V_0 \cos(\omega_0 t)$  is the signal from the resistor,  $V_1 \sin(\omega_0 t)$  is the signal from the capacitor,  $\delta_t$  is the noise,  $\phi$  is the phase delay between reference channel and signal channel and  $V_{ref}$  is the reference signal. After supplying both signal and reference to the lock in amplifier have

$$\begin{aligned} V_s V_{ref} &= (V_0 \cos(\omega_0 t) + V_1 \sin(\omega_0 t) + \delta_t) \cos(\omega_0 t + \phi) \\ &= 1/2 V_0 \cos(\phi) + 1/2 V_0 \cos(2\omega_0 t + \phi) \dots \\ &\quad + 1/2 V_1 \sin(\phi) + 1/2 V_1 \sin(2\omega_0 t + \phi) \dots \\ &\quad + \delta_t \cos(\omega_0 t + \phi) \end{aligned} \quad (4.3)$$

After a low pass filter, the final signal becomes,

$$V = 1/2 V_0 \cos(\phi) + 1/2 V_1 \sin(\phi) \quad (4.4)$$

The signal is  $1/2 V_0 \cos(\phi)$ , however due to the phase delay, the final signal includes a signal from the capacitor. If  $V_1$  is close to  $V_0$ , the influence from the capacitor could be very large, and it will harm the accuracy of measurement. There are several sources causing this phase delay, like the amplifiers and the BNC cables. In our measurement, the major phase delay comes from the function generator, Agilent 33220a, which means the phase of the AC voltage and the TTL reference signal are not same. This phase delay varies with frequencies. For example, there is a 15 degree delay at 1 kHz compared to 1 Hz. In order to get an accurate signal, it is necessary to exclude the phase delay by adjusting the phase of the reference channel of the lock in amplifier.

## 4.4.2 Results and discussion

### 4.4.2.1 Noise and drift current

Before using lock in amplifier, a proper modulation frequency must be determined by the analysis of the noise spectrum of the device. The noise spectrum at a DC voltage of 0.7 V is shown in Figure 4.10. From the noise spectrum, we find that there is a  $1/f$  noise in the low frequency region. It should be expected that as the modulation frequency moves from the low frequency region to the white noise region, the noise should drop.

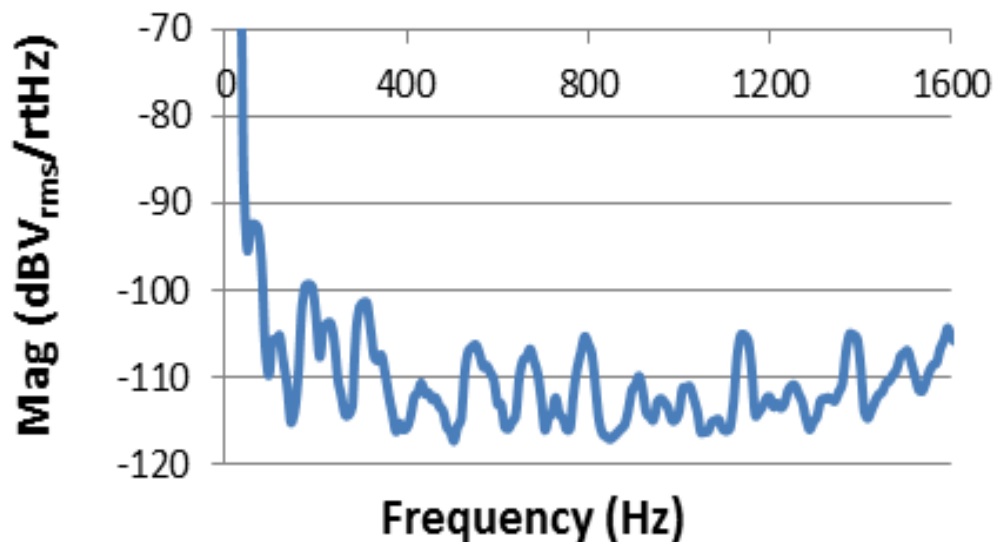


Figure 4.10 Noise spectrum.

The modulation frequencies we choose are 10 Hz, 100 Hz and 1 kHz, and the time constant is kept at 100 ms. The gain of the preamplifier is 5  $\mu\text{A/V}$ , which provides a 10 kHz band width. The measurement results are shown in Figure 4.11, and the standard deviations/average (SD/avg) are given in Table 5. Both standard deviation and average are calculated from 50 continuous samples. It is clear that when the modulation frequency changes from the  $1/f$  noise region to the white noise region, the noise decreases.

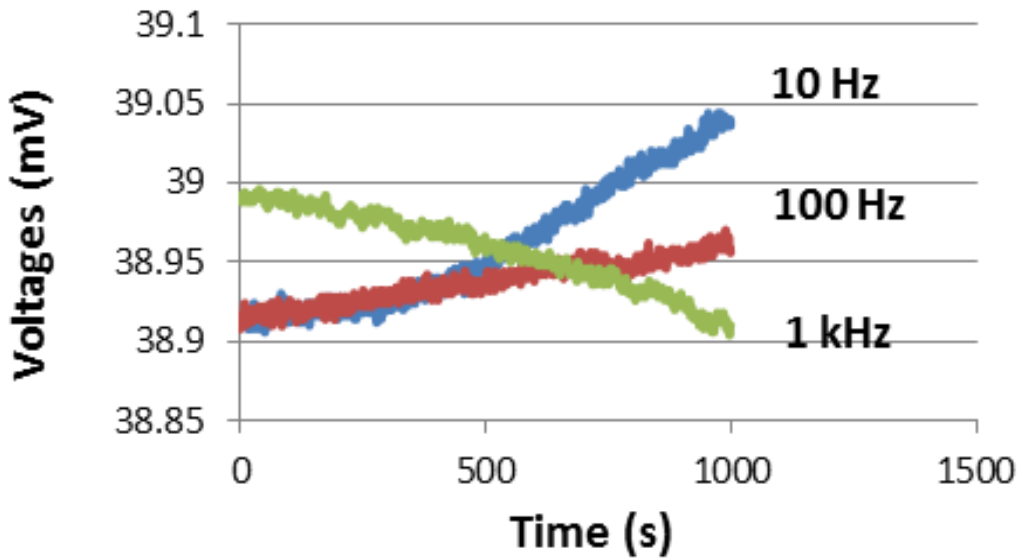


Figure 4.11 AC measurement at different frequencies when the time constant is 100 ms.

Table 5

Noise measurement at different frequencies

	10 Hz	100 Hz	1 kHz
SD/avg	0.012%	0.009%	0.002%

Figure 4.11 also show that the drift tunneling current observed in the DC method is not improved by the AC measurement, which can be explained by the following equations. Adding a modulation signal to (4.1) and only consider the resistor part get

$$V_s' = \cos(w_1 t) V_0 \cos(w_0 t) \quad (4.5)$$

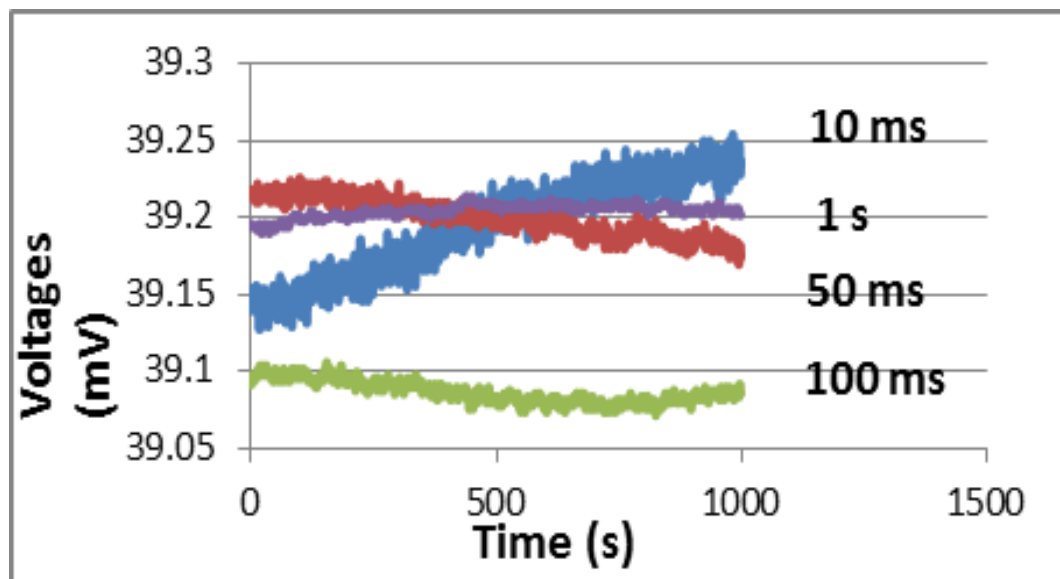
where  $\cos(w_1 t)$  is introduced by the drift tunneling current and  $w_1$  is usually a very small frequency which is far less than  $w_0$ . The drift tunneling current may not be a simple sine wave, but if the drifting is very slow, an assumption of a

sine wave is enough for the analysis. According to our experiment, it is true that the drifting is at a very low frequency which is far less than 1 Hz. The output of lock in amplifier is,

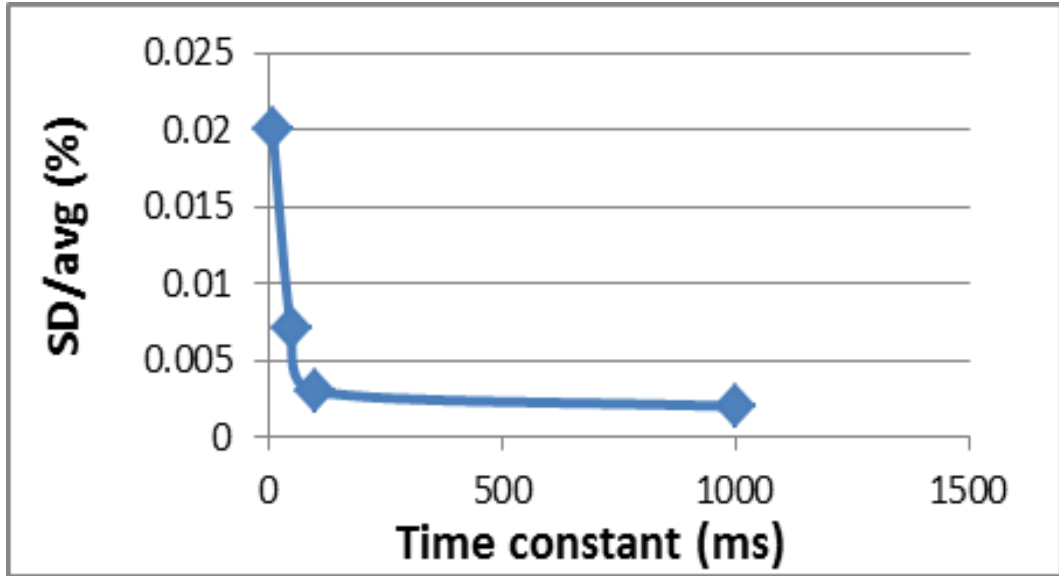
$$V = 1/2 \cos(\omega_1 t) V_0 \cos(\phi) \quad (4.6)$$

Thus the AC measurement using lock in amplifier cannot get rid of the drift tunneling current.

To see the effects of the time constant, 1 kHz is chosen as the modulation frequency and vary time constant  $\tau$  from 10 ms to 1 s. Figure 4.12 and Table 6 show the results. The noise decreases substantially as the time constant is increased. In Table 6, the noise observed from the DC measurement (Figure 4.14(a)) is also included. The time constant of DC measurement is 0.6 s, and its noise is close to that of the AC method at 0.08 s. To have a noise of 0.005%, AC method is almost eight times faster than the DC method. Figure 4.12(b) shows that noise reduction below 100 ms is more efficient.



(a)



(b)

Figure 4.12 (a) AC measurement of different time constant at 1 kHz; (b) SD/avg vs. time constant.

Table 6

Noise measurement at different time constant

	10 ms	50 ms	100 ms	1 s	DC
SD/avg	0.02%	0.007%	0.003%	0.002%	0.005%
SD/avg/ $\tau$	2%	0.14%	0.03%	0.002%	0.008%

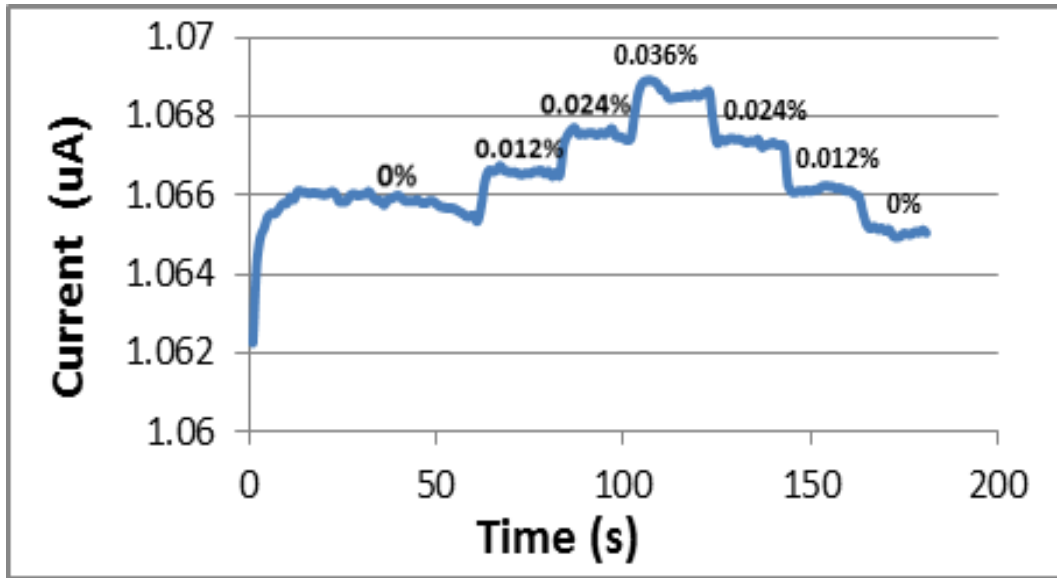
#### 4.4.2.2 Sensitivity

The sensitivity for both the DC and the AC method is defined as  $\Delta I_g/I_g$ , where  $I_g$  is the tunneling current. Although it is the voltage from the lock in amplifier that is measured for the AC method,  $\Delta I_g/I_g$  equals  $\Delta V_g/V_g$ .

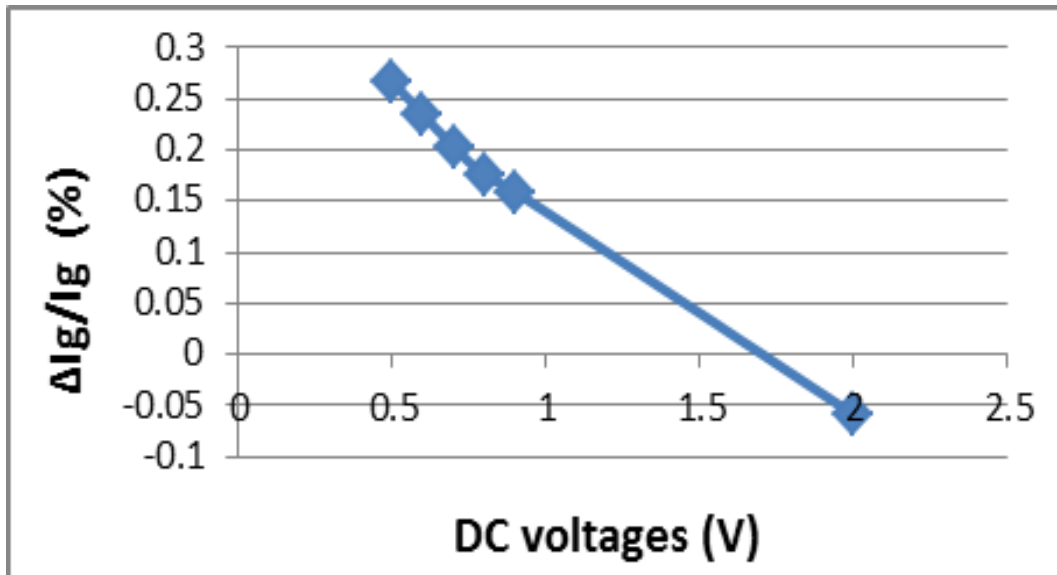
Figure 4.13(a) presents how the tunneling current at  $V_{dc}=0.7$  V changes with the tensile strain which is along [110] direction. The strain is increased from 0% to 0.036% and then decreased to 0% at a step of 0.012%. The same procedure is also applied to the DC voltages at 0.5 V, 0.6 V, 0.8 V,

0.9 V and 2 V. Figure 4.13(b) shows how the sensitivity changing with the DC voltages at the strain of 0.012%. As the theory predicts, the sensitivity drops and eventually becomes negative.

The amplitudes of AC voltages chosen for the AC measurements are 20 Vrms, 50 Vrms, 100 Vrms and 200 Vrms, while the device is biased at 0.7 V. The results are given in Figure 4.14. The measurement procedure is the same as the DC measurement. Figure 4.14(b) shows that the sensitivity of AC method first increases, but then decreases with the increasing of the AC amplitude. This can be explained by that the AC method measures the slope of the current vs. voltage curve of the DC method. Taking 20 mV as an example, as the amplitude is small, the current is determined by both the high peak  $0.7+0.028=0.728$  V and the low peak  $0.7-0.028=0.672$  V. At tensile strain, the sensitivity at the low peak is larger than that of the high peak, which in turn reduces the slope changing, so the sensitivity is reduced. As the amplitude increases, the influence from the low peak weakens and the sensitivity tries to increase, but the sensitivity at high peak decreases, so there is a competition. When the amplitude is smaller than 100 mV, the low peak weakening has more influence on the sensitivity, so we see the sensitivity increase. When the amplitude is larger than 100 mV, the sensitivity at high peak dominates, decreasing sensitivity is observed. As a result, the AC method will have a lower sensitivity than the DC method at the same DC offset.

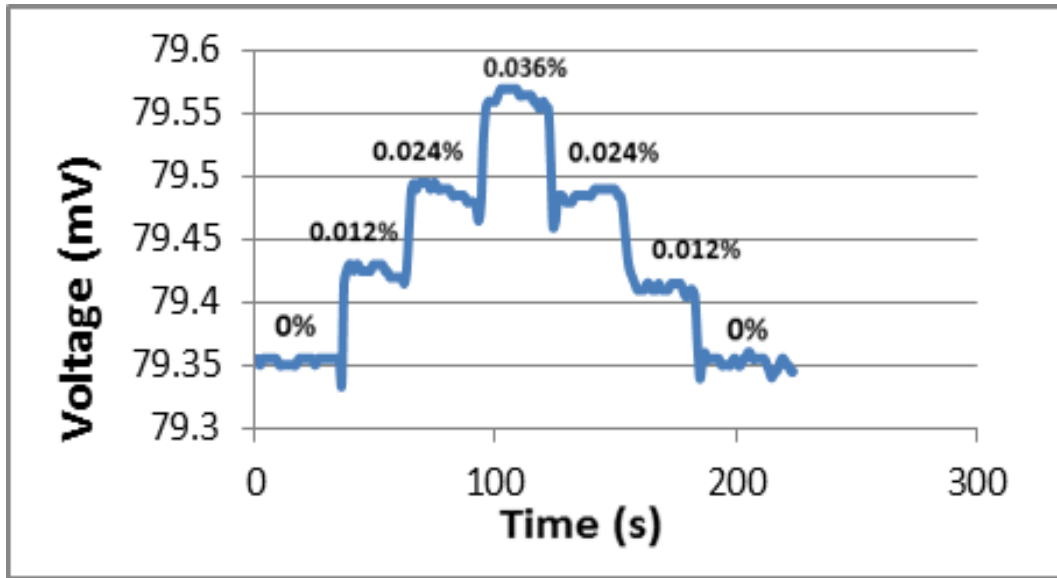


(a)

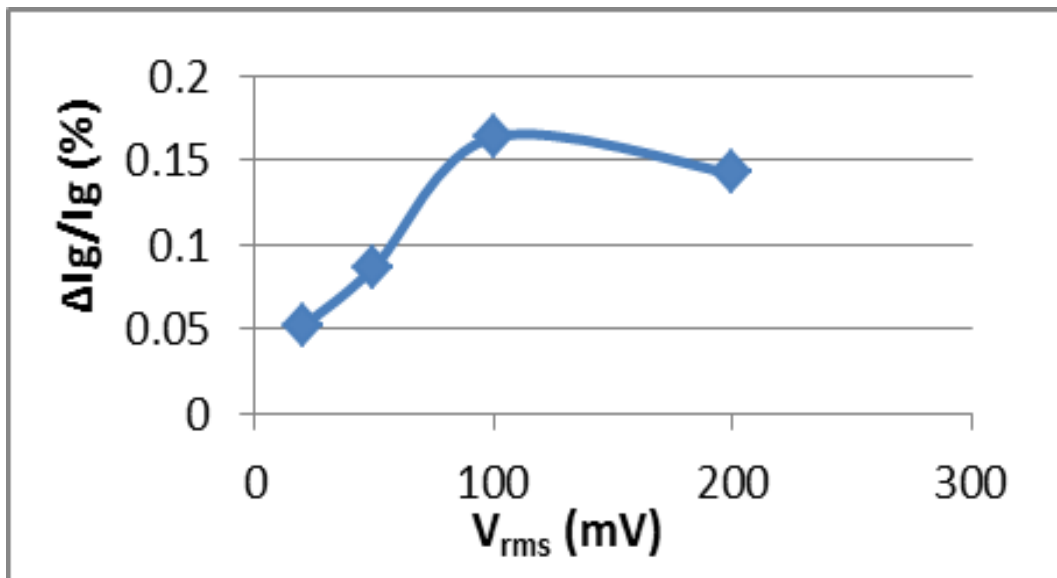


(b)

Figure 4.13 DC method. (a) tunneling current at  $V_{dc}=0.7$  V; (b) strain response at different DC voltages at the strain of 0.012%.



(a)



(b)

Figure 4.14 AC method. (a) tunneling current at  $V_{rms}=100$  mV,  $V_{dc}=0.7$  V and 1 kHz; (b) strain response at different DC voltages at the strain of 0.012%.

#### 4.4.3 Conclusions

The DC and the AC measurement techniques for the MOS tunneling strain sensor are compared, and it is found that AC method has a better performance in noise reduction. When the modulation frequency used in the AC measurement is far from the  $1/f$  noise, the AC measurement technique is



found to eight times faster than the DC measurement to get a same level of noise. The sensitivity of AC method is close to the sensitivity of the DC technique. However, a drift current is observed in both methods, and it is impossible to be removed by the AC method.

CHAPTER 5  
MOS STRAIN SENSOR SENSITIVITY STUDY BASED ON ECB AND E.B  
MODELING

**5.1 Introduction**

This chapter builds simulation models for MOS tunneling current strain sensor. The purpose of modeling is to provide an explanation for the experimental results, and to better understand how to optimize a tunneling current strain sensor.

The tunneling current through an MOS structure has been well studied. However, there is very little literature on the change of the tunneling current with respect to strain. Several groups have studied the change of the NMOS gate current in the inversion region, but they only considered tunneling from the conduction band of the substrate to the gate (ECB tunneling) [55-57]. ECB tunneling has been successfully applied to explain the gate tunneling current in NMOS transistors for zero strain, or for a strained MOSFET with low substrate doping concentrations. This chapter will show that the valence band tunneling (EVB tunneling) is necessary to explain the sensitivity of a MOS tunneling current strain sensor, especially when the substrate doping concentration is high to minimize series resistance, or when a large gate voltage is applied. The tunneling current was calculated using both ECB and EVB tunneling, and the effects of doping concentration were studied. The

model used is appropriate for a NMOS tunneling current strain sensor made on a (001) silicon wafer which is positively biased to the inversion region.

Section 5.2 and Section 5.3 discuss ECB modeling and EVB modeling and verify the modeling results with experiment results from other groups. Then Section 5.4 uses models to simulate the proposed devices used in DC measurement. Section 5.5 studies the influence from substrate doping concentration.

## **5.2 ECB modeling**

For ECB tunneling current, Thompson's group built a model to simulate the stress altered gate current by self-consistently solving Schrodinger equation and Poisson equation for the quantized carrier layers and solving the tunneling probability using the transfer-matrix-method [17, 55]. The model requires a lot of effort and time to compute. To predict how MOS tunneling current changes with strain in the inversion region quickly and accurately, computationally efficient models are built. Here approximate methods are used to solve the energy quantization and the WKB method to solve the tunneling probability. The strain induced energy shift can be expressed by deformation potential theory [58]. Two approximate methods to solve the energy quantization are employed and compared. For the energy quantization, the tunneling current is computed as a function of stress for each method.

The models are built for n-type MOS capacitor on a (001) wafer with a heavily doped n-type poly-silicon gate. The gate current and electron energy quantization are along the <001> direction or Z direction. As shown in Figure 5.1, the MOS capacitor is positively biased to the inversion region, in which

the electrons' energies are quantized. The six degenerate conduction band minimum are divided into two groups, the two-fold degenerate  $\Delta_2$  group whose longitudinal effective mass is along the  $\langle 001 \rangle$  direction, and the four-fold degenerate  $\Delta_4$  group whose transverse effective mass is along the  $\langle 001 \rangle$  direction. Since the longitudinal effective mass is larger than the transverse effective mass, the  $\Delta_2$  group has lower energy levels. The MOS capacitor's tunneling current through the silicon dioxide is determined by (1) the energy barrier height between the silicon conduction band edge and the  $\text{SiO}_2$  conduction band edge; and (2) the electrons' out of plane effective mass. When a  $\langle 110 \rangle$  uniaxial tensile strain is induced, the band gap of silicon is decreased and conduction band edge of silicon is lowered. In addition, the  $\Delta_2$  valleys are lowered in energy and the  $\Delta_4$  valleys are raised in energy. As a result, both effects decrease the tunneling current. In contrast, as a  $\langle 110 \rangle$  compressive strain is applied, the tunneling current is increased.

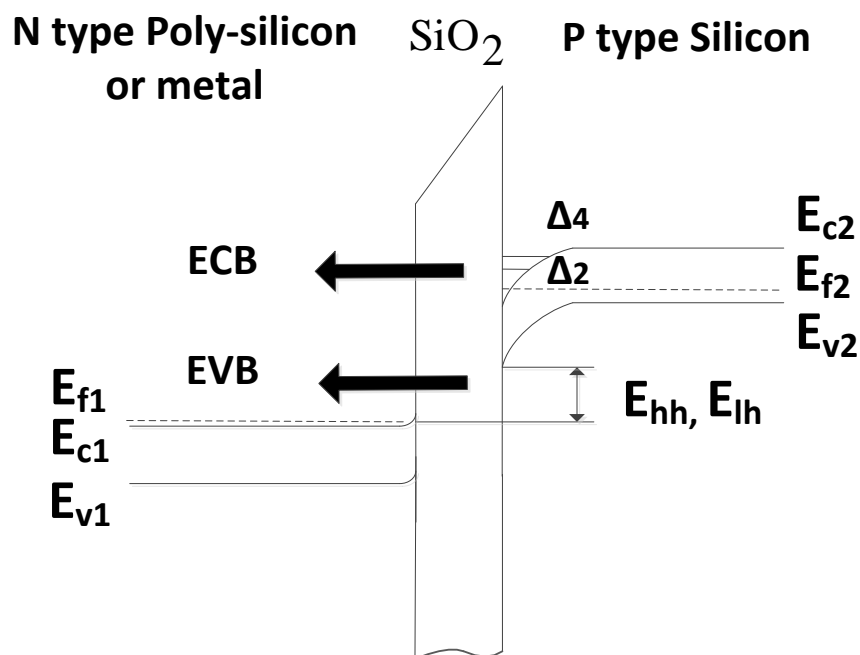


Figure 5.1 NMOS in inversion region.

### 5.2.1 Approximate methods for quantized inversion layer

The sub-bands of inversion layer of NMOS capacitor can be obtained by self-consistently solving the Schrodinger equation and Poisson equation. Using the effective mass approximation, the electronic wave function can be written as [59],

$$\psi_{i,j}(x, y, z) = \zeta_{i,j}(z)e^{i\theta z}e^{ik_1x+ik_2y} \quad (5.1)$$

where  $\psi_{i,j}(x, y, z)$  is the envelope of the  $i$ th energy level,  $\zeta_{i,j}(z)$  is the envelope along the  $z$  direction,  $\theta$  is determined by  $k_1$  and  $k_2$ ,  $i$  denotes  $\Delta_2$  and  $\Delta_4$  and equals to 2 for  $\Delta_2$  or 4 for  $\Delta_4$ ,  $j$  denotes the sub-bands levels. This approximation decouples the 3D Schrodinger equation into a 1D equation,

$$\left[ -\frac{\hbar^2}{2m_{z,i}} - \frac{d^2}{dz^2} + eV(z) \right] \zeta_{i,j}(z) = E_{i,j}\zeta_{i,j}(z) \quad (5.2)$$

where  $E_{i,j}$  is the sub-band energy level (the conduction band edge at the surface is the relative 0 eV),  $e$  is the electron charge,  $\hbar$  is Plank's constant,  $m_{z,i}$  is the electron effective mass in the  $z$ -direction, and  $V(z)$  is the potential well which is determined by the Poisson equation,

$$\frac{d^2V(z)}{dz^2} = -\rho(z)/\epsilon_{Si} \quad (5.3)$$

where  $\rho(z)$  is the charge density including both depletion layer and inversion layer, and  $\epsilon_{Si}$  is the dielectric constant of silicon. Since the charge density solved from the Schrodinger equation will influence the potential well and the potential well in turn determines the charge density, a self-consistent way to solve Schrodinger equation and Poisson equation is needed. To obtain accurate results, a numerical method to solve differential equations may be

employed which is quite time consuming and costly. Alternatively, a triangular potential well approximation method may be used to simplify the self-consistent coupling, which leads to the well-known Airy equation solutions [60],

$$\zeta_{i,j}(z) = A_{i,j}(2m_z e F_s / \hbar^2)^{1/3} [z - E_{i,j} / e F_s] \quad (5.4)$$

$$E_{i,j} = (\hbar^2 / 2m_{z,i})^{1/3} [3/2\pi e F_s (j + 3/4)]^{2/3} \quad (5.5)$$

Where

$$Z_{i,j} = 2E_{i,j} / 3eF_s \quad (5.6)$$

$$F_s = \frac{e(N_{depl} + N_{inv})}{\epsilon_{Si}} \quad (5.7)$$

$$N_{depl} = \sqrt{2\epsilon_{Si}\psi_d N_a / e} \quad (5.8)$$

$$N_{inv} = \sum_{i,j} N_{inv i,j} \quad (5.9)$$

$$N_{inv i,j} = \frac{k_B T m_{d,i} g_{\Delta 2/4}}{\pi \hbar^2} \ln[1 + e^{-\frac{(E_{i,j} - E_f)}{k_B T}}] \quad (5.10)$$

$$\psi_d = \psi_s - \frac{k_B T}{e} - e N_{inv} Z_{av} / \epsilon_{Si} \quad (5.11)$$

$$Z_{av} = \sum_{i,j} N_{inv i,j} Z_{i,j} / N_{inv} \quad (5.12)$$

$$E_f = -E_g + e\psi_s - k_B T \ln(N_v / N_a) \quad (5.13)$$

where  $Z_{i,j}$  is the penetration distance of the inversion layer carriers

from the surface,  $F_s$  is the surface electric field,  $N_{depl}$  is depletion layer charge concentration,  $N_{inv}$  is the total inversion layer charge concentration,  $\psi_d$  is the surface band bending without contribution of inversion layer,  $N_a$  is substrate doping concentration,  $N_{inv,i,j}$  is the sub-bands charge concentration,  $k_B$  is the Boltzmann constant,  $T$  is the temperature,  $m_{d,i}$  is the density of states effective mass per valley,  $g_{\Delta_{2/4}}$  is the valley degeneracy,  $E_f$  is the Fermi level relative to the surface conduction band edge,  $\psi_s$  is the surface potential,  $Z_{av}$  is the average distance inversion layer carriers from the surface,  $E_g$  is the band gap and  $n_i$  is the intrinsic carrier concentration. However, this triangular potential well method only provides good approximate results when the inversion layer charge density is smaller than the depletion charge density. A variational method was proposed by assuming that most of charges occupy the ground sub band and using a trial eigenfunction. The ground energy levels can be described as [60, 61],

$$E_{i,1} = \left(\frac{3}{2}\right)^{\frac{5}{3}} \left(\frac{e^2 \hbar}{m_{z,i} \frac{1}{2} \epsilon_{Si}}\right)^{\frac{2}{3}} \frac{(N_{depl} + \frac{55}{96} N_{inv})}{(N_{depl} + \frac{11}{32} N_{inv})^{1/3}} \quad (5.14)$$

$$Z_{i,1} = \left(\frac{9 \epsilon_{Si} \hbar^2}{4 m_{z,i} e^2 (N_{depl} + \frac{11}{32} N_{inv})}\right)^{\frac{1}{3}} + 4Na \left(\frac{9 \epsilon_{Si} \hbar^2}{4 m_{z,i} e^2 (N_{depl} + \frac{11}{32} N_{inv})}\right)^{2/3} / \quad (5.15)$$

$$9 \left(N_{depl} + \frac{11}{32} N_{inv}\right)$$

This equation can be applied to both  $\Delta_2$  and  $\Delta_4$  by using different out of plane effective masses,  $m_{z,i}$ , for  $\Delta_2$  and  $\Delta_4$ . Since the higher states have less influence, we still use (5.5) & (5.6) for the higher states. Table 7 gives the value of parameters used in the modeling.  $m_e$  is the free space electron mass.

Table 7

Values of effective masses used in this paper.

$m_{z,2}$	$0.98m_e$
$m_{z,4}$	$0.19m_e$
$m_{d,2}$	$0.19m_e$
$m_{d,4}$	$0.417m_e$

Figure 5.2 shows the sub-bands and the Fermi level for the triangle approximation method and the variational method, as well as the self-consistent method solving differential equations using Schred [62].  $E_{21}$  is the ground state for the  $\Delta_2$  valley, and  $E_{41}$  is the ground state for the  $\Delta_4$  valley. From Figure 3, it is observed that at low voltages the sub-bands from the two approximate methods are close to the results from Schred. However, the difference between the approximate methods and Schred becomes large as the voltage increases. It is clear that compared with the triangle approximate method, the variational method gives a better fit.

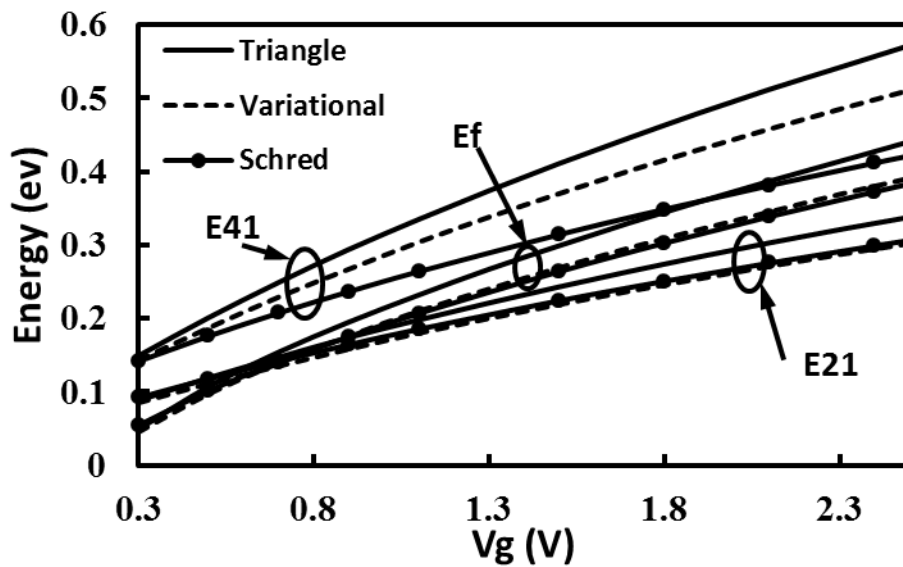




Figure 5.2 Sub-bands vs. gate voltage. The doping concentration of p-type substrate is  $1e17 \text{ cm}^{-3}$ . The doping concentration of n-type poly gate is  $1e20 \text{ cm}^{-3}$ . The thickness of gate oxide is 2.19 nm.

### 5.2.2 ECB tunneling current using WKB approximation

After obtaining the sub-bands, the WKB approximation method is used to obtain the direct tunneling current,

$$J = \sum_{i,j} \frac{qN_{inv i,j}}{\tau_{i,j}} \quad (5.16)$$

where

$$\tau_{i,j} = \frac{j\pi\hbar}{E_{i,j}TR} \quad (5.17)$$

Here TR is the modified WKB approach tunneling probability [56, 57, 63].  $TR_{i,j}$  is the modified WKB approach tunneling probability, which is expressed as [57]:

$$TR = WKB_{i,j}T_{i,j} \quad (5.18)$$

where  $WKB_{i,j}$  is the classic WKB approach tunneling probability for each sub-bands.  $T_{i,j}$  is the correction factor considering reflection within the gate oxide.  $WKB_{i,j}$  and  $T_{i,j}$  are expressed below:

$$WKB_{i,j} = e^{-\frac{E_g\sqrt{2m_{ox}}}{4\hbar qF_{ox}} \left[ 2\left(1 - \frac{2E_{ox}}{E_g}\right) \sqrt{E_{ox}\left(1 - \frac{2E_{ox}}{E_g}\right) + \sqrt{E_g} \sin\left(1 - \frac{2E_{ox}}{E_g}\right)} \right]} \Bigg|_{E_{ox}=\psi_{an}}^{E_{ox}=\psi_{cath}} \quad (5.19)$$

$$T_{i,j} = \frac{4vs1_{i,j}v_{oxcath_{i,j}}}{vs1_{i,j}^2 + v_{oxcath_{i,j}}^2} \frac{4vs2_{i,j}v_{oxan_{i,j}}}{vs2_{i,j}^2 + v_{oxan_{i,j}}^2} \quad (5.20)$$

where the Franz dispersion relation is used to calculate  $WKB_{i,j}$ .  $E_g$  is the gate oxide band gap, which is equal to 9.3 eV.  $m_{ox}$  is the electron effective

mass, which equals to  $0.38m_0$  for an Al gate and  $0.55m_0$  for a poly-Silicon gate, where  $m_0$  is free space electron mass.  $F_{ox}$  is electrical field in oxide.  $E_{ox}$  is electron energy referred to the gate oxide conduction band edge, which equals to  $\psi_{cath} = q\chi_c - E_{i,j}$  at the cathode side and  $\psi_{an} = q\chi_c - E_{i,j} - qF_{ox}t_{ox}$  at the anode side.  $\chi_c$  is the tunneling barrier between the edge of oxide conduction band and the edge of Silicon conduction band, which equals to 3.1 eV. This analysis ignores the electron kinetic energy parallel to interface.

Using the parabolic dispersion relation,  $vs1_{i,j} = \sqrt{\frac{2E_{i,j}}{m_{i,z}}}$  and  $vs2_{i,j} = \sqrt{\frac{2E_{i,j} + qF_{ox}t_{ox}}{m_{i,z}}}$  are the electron group velocity incident and leaving the oxide, respectively, where  $m_{i,z}$  is the electron out-of-plane effective mass. Under the

Franz dispersion relation,  $voxcath_{i,j} = \frac{1}{2\psi_{cath}/E_g} \sqrt{\frac{2\psi_{cath}(1-\psi_{cath}/E_g)}{m_{ox}}}$  and  $voxan_{i,j} = \frac{1}{2\psi_{an}/E_g} \sqrt{\frac{2\psi_{an}(1-\psi_{an}/E_g)}{m_{ox}}}$  are the group velocity of electrons at the

cathode and the anode within gate oxide. Other parameters used in modeling are the same as [64]. Details about TR refer to Chapter 2.

Figure 5.3 shows the gate current from modeling and experiment. Both methods give a gate current that is similar compared to the experimental result for voltages larger than 1 V. There is minimal difference between the two modeling methods from the gate current modeling with zero stress.

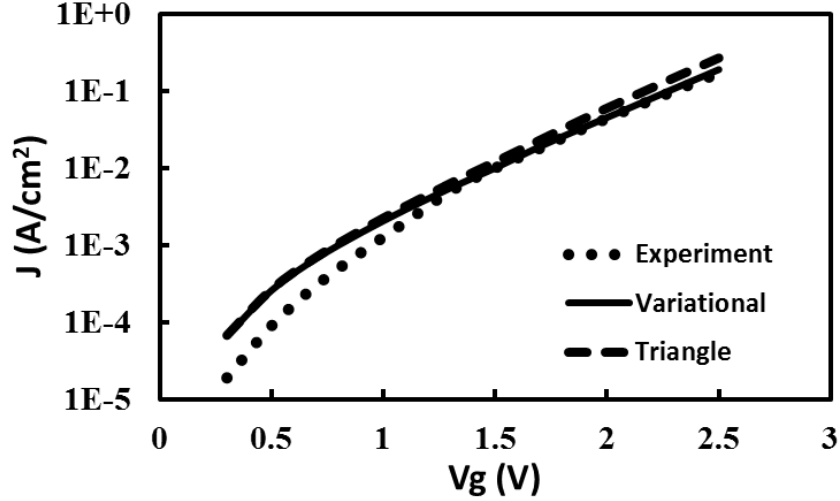


Figure 5.3 Gate current density vs. gate voltage. The device parameters are the same as used in Figure 5.2. The experiment results are from [65].

### 5.2.3 Strain induced ECB tunneling current changing

Considering an  $\langle 110 \rangle$  uniaxial stress is applied to the wafer, and applying deformation potential theory, the sub-bands with stress can be obtained,

$$E'_{2,j} = E_{\Delta_{2,j}} + \left( \varepsilon_d + \frac{\varepsilon_u}{3} \right) (S_{11} + 2S_{12})\sigma + \left( \frac{\varepsilon_u}{3} \right) (S_{12} - S_{11})\sigma \quad (5.21)$$

$$E'_{4,j} = E_{4,j} + \left( \varepsilon_d + \frac{\varepsilon_u}{3} \right) (S_{11} + 2S_{12})\sigma - \left( \frac{\varepsilon_u}{6} \right) (S_{12} - S_{11})\sigma \quad (5.22)$$

where  $\varepsilon_d = 1.13 \text{ eV}$  ,  $\varepsilon_u = 9.16 \text{ eV}$  ,  $S_{11} = 7.68 \text{ e} - 12 \text{ m}^2/\text{N}$  ,  $S_{12} = -2.14 \text{ e} - 12 \text{ m}^2/\text{N}$ . As a result, the tunneling current with stress can be obtained by substituting the sub bands with stress into (5.16), which is,

$$J'(\sigma) = \sum_j \frac{qN'_{inv2,j}(\sigma)}{\tau'_{2,j}(\sigma)} + \sum_j \frac{qN'_{inv4,j}(\sigma)}{\tau'_{4,j}(\sigma)} \quad (5.23)$$

The change in tunneling current can be expressed as,

$$\Delta J/J(\sigma) = \frac{J'(\sigma) - J}{J} \quad (5.24)$$

Figure 5.4 shows the comparison between triangle potential approach and the variational approach for  $\Delta J/J(\sigma)$ , as well as the comparison to the experimental results for both approaches. Figure 5.4 indicates that the variational approach is closer to the experimental results.

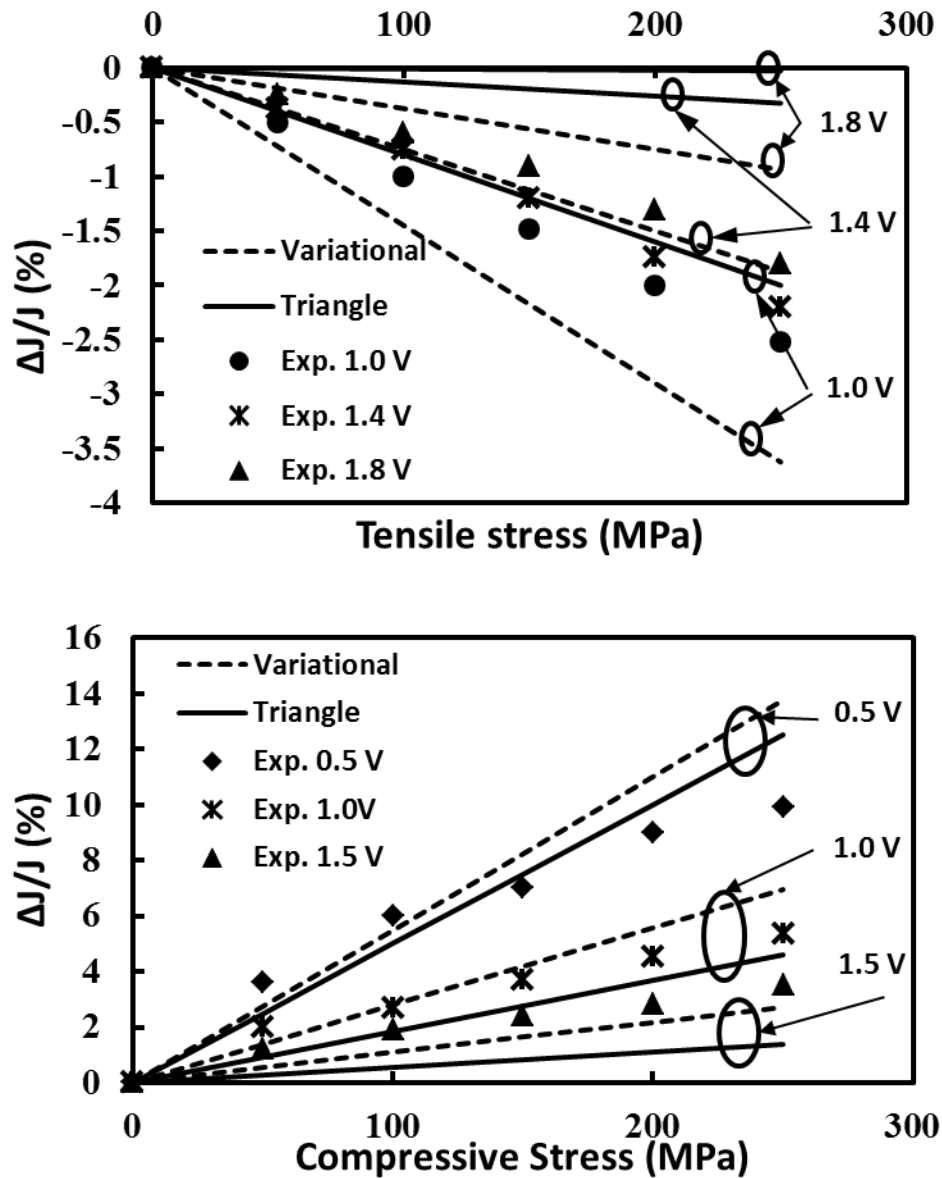


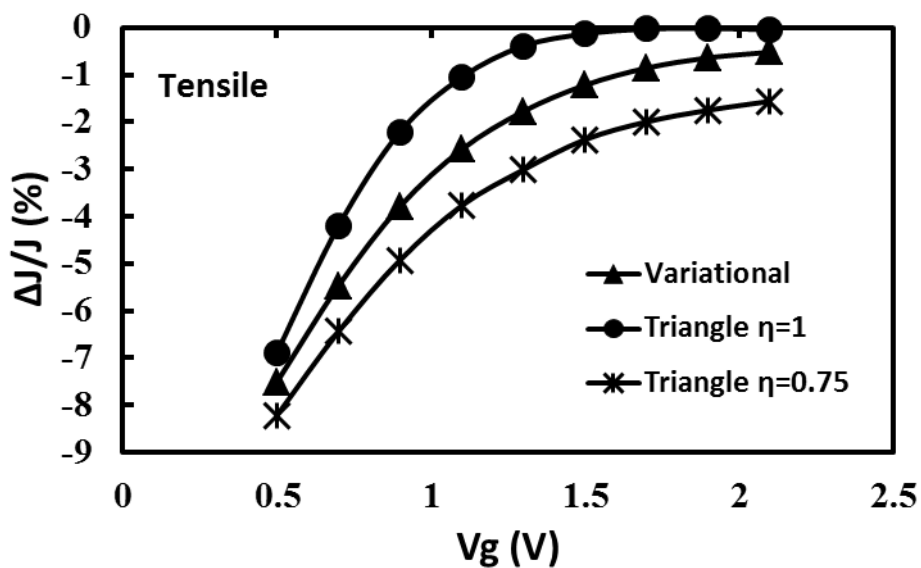
Figure 5.4 Modeling vs. experimental results. For the tensile case, the doping concentration is  $5e17 \text{ cm}^{-3}$  for the p-type substrate and  $1e20 \text{ cm}^{-3}$  for the n-type poly gate. The thickness of gate oxide is 1.3 nm. The experimental

data for the tensile is from [55]. For the compressive case, the doping concentration is  $1e17 \text{ cm}^{-3}$  for the p-type substrate and  $1e20 \text{ cm}^{-3}$  for the n-type poly gate. The thickness of gate oxide is 1.3 nm. The experimental data for the tensile is from [66].

In some papers, a correction coefficient  $\eta$  is used in (5.7), which is modified to,

$$F_s = \frac{e(N_{depl} + \eta N_{inv})}{\epsilon_{Si}} \quad (5.25)$$

It is typically some number between 0.5 and 1 [66-68]. In Figure 5.5,  $\Delta J/J$  vs. voltage are plotted for  $\pm 200 \text{ MPa}$  stress. The sensitivity decreases as the voltage increases for both tensile stress and compressive stress. The triangle method with  $\eta = 0.75$  has a larger change in current than for  $\eta = 1$ . The correction factor may be chosen to fit experiment, but it is not known *a priori*.



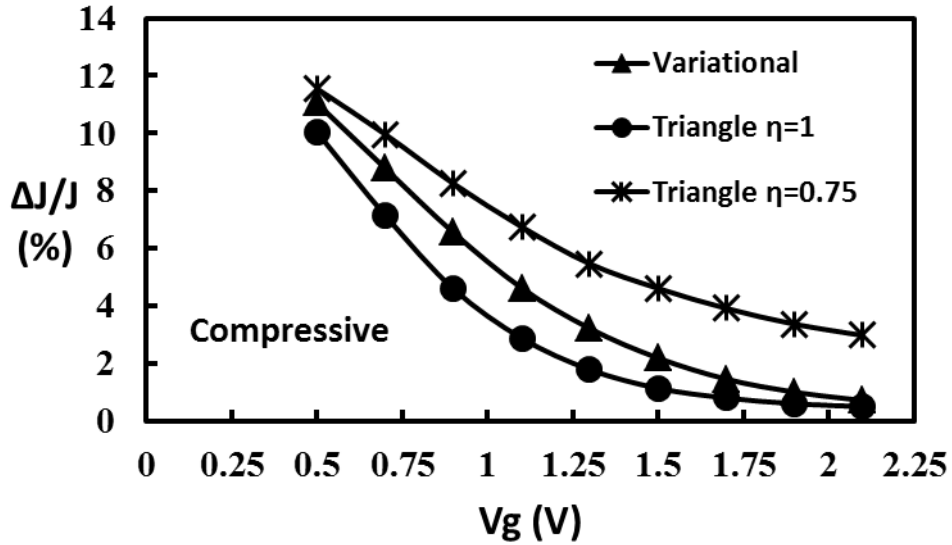


Figure 5.5 Percent change in current density versus voltage. The tensile and compressive stress are both 200 MPa. The parameters are the same as Figure 5.4.

#### 5.2.4 Summary of ECB tunneling current modeling

For this study, two computationally efficient models are built to study stress induced gate current changing for NMOS capacitor which is biased to inversion region. The computational efficiency comes from the adoption of approximate method for the sub-bands and WKB method for the tunneling probability. The sub-bands from these two models are compared with Schred which solves differential equations self-consistently, which shows that the results from the variational method are closer to Schred than the triangle approximate method. The two approximation methods provide nearly the same current without stress, but when stress is applied, the variational method provides an answer that is much closer to experiment. This model can be used to better model and understand MOS tunneling current sensors.

#### 5.3 EVB modeling

Unlike ECB tunneling current, the electrons in the valence band are not

confined in a 2D layer at the surface, so quantization is not necessary. As shown in Figure 5.1, the Fermi level at gate,  $E_{f1}$ , is set to be the relative 0 energy level.  $E_{f2}$  is the Fermi level in substrate.  $E_{c1}$  and  $E_{c2}$  are the conduction band edges of the gate and substrate, respectively.  $E_{v1}$  and  $E_{v2}$  are the valence band edges of the gate and substrate, respectively.

$E_{hh}$  and  $E_{lh}$  are the difference between  $E_{v2}$  and  $E_{f1}$  for the heavy hole band and the light hole band. When there is no stress,  $E_{hh} = E_{lh} = E_{v2} - E_{f1}$ . When there is uniaxial stress, the heavy hole band and the light hole band are split. For a metal gate, there is no band gap, so  $E_{hh}$  and  $E_{lh}$  do not have to be larger than 0 for tunneling to occur. The EVB tunneling current can be expressed as:

$$J_{evb} = J_{hh} + J_{lh} \quad (5.26)$$

where  $J_{hh}$  is the component in which electrons have a heavy hole effective mass and  $J_{lh}$  is the component in which electrons have a light hole effective mass. Adopting a model from Tsu and Esaki [69],  $J_{hh}$  and  $J_{lh}$  may be obtained:

$$\begin{aligned} J_{hh} &= \frac{4\pi q m_{hh}}{h^3} \int_{E_{min}}^{E_{hh}} TR_{hh}(E_x) dE_x \int_0^{E_{hh}-E_x} (1 - f_1(E)) f_2(E) dE_r \\ &= \frac{4\pi q m_{hh}}{h^3} \int_{E_{min}}^{E_{hh}} TR_{hh}(E_x) (1 - f_1(E)) (E_{hh} - E_x) dE_x \end{aligned} \quad (5.27)$$

$$\begin{aligned} J_{lh} &= \frac{4\pi q m_{lh}}{h^3} \int_{E_{min}}^{E_{lh}} TR_{lh}(E_x) dE_x \int_0^{E_{lh}-E_x} (1 - f_1(E)) f_2(E) dE_r \\ &= \frac{4\pi q m_{lh}}{h^3} \int_{E_{min}}^{E_{lh}} TR_{lh}(E_x) (1 - f_1(E)) (E_{lh} - E_x) dE_x \end{aligned} \quad (5.28)$$

where  $m_{hh}$  equals  $0.49m_0$  and  $m_{lh}$  equals  $0.16m_0$ .  $f_1(E)$  and  $f_2(E)$  are

the Fermi-Dirac distribution for electrons in the gate and the substrate, respectively, where  $E = E_x + E_r$ . In the inversion region, because the difference between  $E_{f2}$  and  $E_{v2}$  is much larger than  $k_B T$ ,  $f_2(E) \approx 1$ , where  $k_B$  is Boltzmann's constant and  $T$  is room temperature.  $TR_{hh}$  and  $TR_{lh}$  are modified WKB approach tunneling probability similar to  $TR$  used for ECB tunneling current modeling, but for the valence band. The tunneling barrier in  $TR_{hh}$  and  $TR_{lh}$  is the difference between the oxide conduction band edge and  $E_{v2}$ , which equals to 4.15 eV. For the aluminum gate, without a band gap in the gate,  $E_{min}$  could be less than 0 eV. In (5.27) and (5.28),  $E_r$  is assumed to be neglectable in  $f_1(E)$  and  $f_2(E)$ .

Figure 5.6 shows EVB modeling results compared with a compact model [70]. Since it is poly-gate, (5.26), (5.27) and (5.28) are only valid, when  $E_{hh}$  and  $E_{lh}$  are  $\geq 0$  eV. Besides,  $E_{min} = 0$  eV.

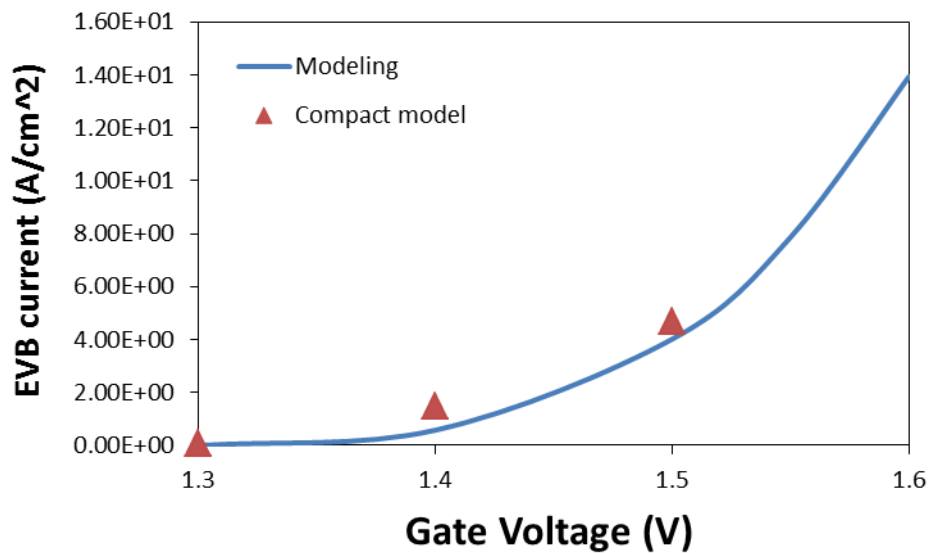


Figure 5.6 EVB modeling. The parameters used in EVB modeling are the same as those in Figure 2 in [70].



When <110> uniaxial stress is applied, the heavy hole band and light hole band are split as follows:

$$E_{hh} = E_{v2} - E_{f1} + \Delta E_{hh} \quad (5.29)$$

$$E_{lh} = E_{v2} - E_{f1} + \Delta E_{lh} \quad (5.30)$$

where  $\Delta E_{hh} = -0.035 * 10^{-9} \sigma$  and  $\Delta E_{lh} = 0.018 * 10^{-9} \sigma$ .  $\Delta E_{hh}$  and  $\Delta E_{lh}$  are the band shift for heavy hole band and light hole band, respectively. It is difficult to get an analytic equation for the valence band shift under uniaxial stress. For this work, the valence band shift was interpolated from the simulation results from [71]. The sensitivity expression for EVB tunneling current is similar to (5.24).

#### 5.4 ECB and EVB tunneling current modeling for the MOS tunneling current strain sensor used in the DC measurement

In the previous sections, models for ECB and EVB tunneling current are built. The section uses these models to simulate the MOS tunneling current strain sensor used in the DC measurement. The device is NMOS capacitor with Al gate. The thickness of gate oxide is 3.7 nm. The substrate doping concentration is  $2.0 \times 10^{18} / \text{cm}^3$ . Table 8 give sensitivity vs. gate voltage from DC measurement in Chapter 4. The models discussed later fit this table.

Table 8

Sensitivity vs. gate voltage from our group's experiment.

Gate voltage (V)	Sensitivity (%)
1	-2.2
1.5	-2.0
2	-2.5

Figure 5.7 shows the current density versus gate voltage. It is clear that at a low voltage, the ECB tunneling current dominates. However as the gate voltage increases, the EVB tunneling current increases rapidly and becomes nearly the same as the ECB tunneling current. Then the total current density is determined by both ECB tunneling current and EVB tunneling current. As discussed in the following section, the sensitivity is also expected to be determined by the ECB tunneling at low voltage, but the influence from the EVB tunneling current becomes more important as the gate voltage increases.

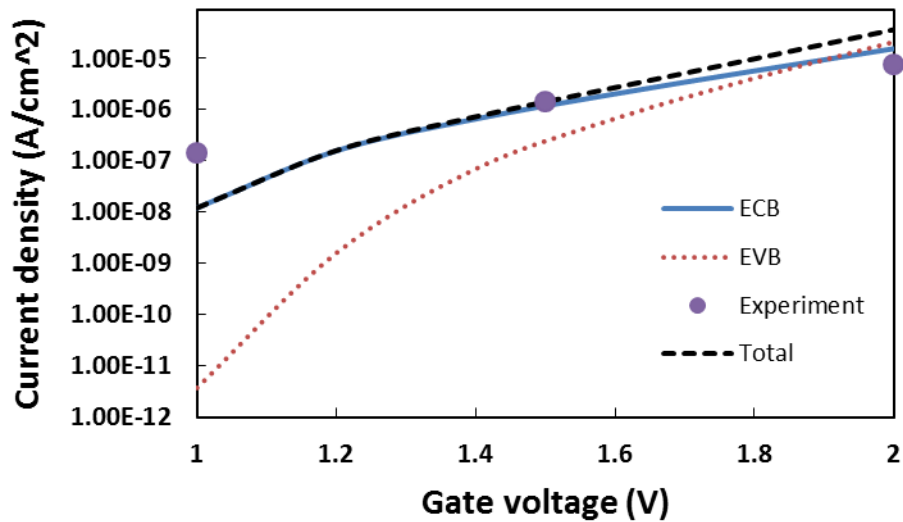


Figure 5.7 Calculated current density for the MOS strain sensor without strain, including the ECB tunneling current, EVB tunneling current, and the total tunneling current. A comparison to the experimental results are also shown.

Figure 5.8 shows sensitivity vs. gate voltage for ECB under 200 MPa <110> uniaxial tensile stress. It is clear that sensitivity decreases with increasing gate voltage for ECB.

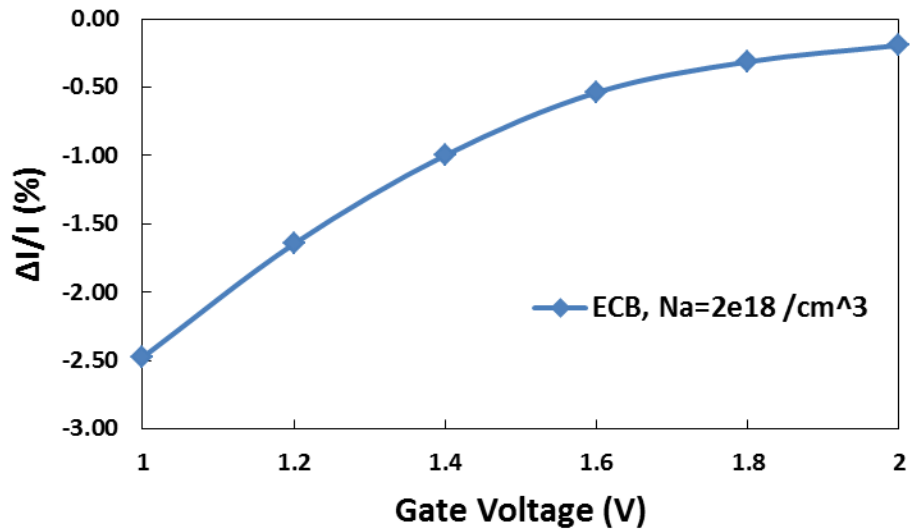


Figure 5.8 Sensitivity vs. gate voltage for ECB.

Figure 5.9 shows the sensitivity versus gate voltage for EVB tunneling current under 200 MPa  $\langle 110 \rangle$  tensile stress. Like the sensitivity versus gate voltage for ECB tunneling current, the sensitivity for EVB tunneling current also decreases as gate voltage increases. However, the sensitivity is much greater than for the ECB tunneling current, and never drops below 4%.

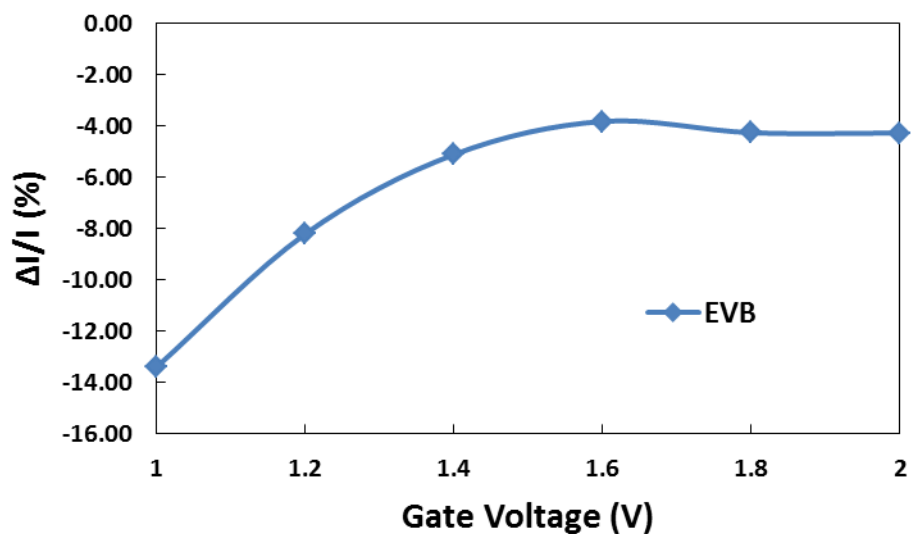


Figure 5.9 Calculated sensitivity vs. gate voltage for EVB tunneling current.

The NMOS tunneling current is comprised of both the ECB tunneling current and the EVB tunneling current and are discussed in this section. The total current density,  $J$ , equals  $J_{ecb} + J_{evb}$ .  $J'(\sigma)$  is the total current density under stress. Similar to (5.24), the sensitivity is expressed as:

$$\Delta J/J(\sigma) = \frac{(J'(\sigma) - J)}{J} \quad (5.31)$$

Figure 5.10 shows the calculated sensitivity versus the gate voltage for our group's device, which agrees with the tensile results in our experiment. The total sensitivity does not simply decrease as the gate voltage increases, even though it decreases for both ECB tunneling current and EVB tunneling current. It is noticed that at the same gate voltage, the sensitivity for EVB tunneling current is larger than ECB tunneling current. When the gate voltage is small, the ECB tunneling current dominates total tunneling current, so its sensitivity dominates the total sensitivity. As the gate voltage increases, the EVB tunneling current becomes close to the ECB tunneling current, so the influence of the EVB sensitivity increases. Because the EVB tunneling current sensitivity is larger than ECB tunneling current sensitivity, it should be expected that the overall sensitivity increases as the gate voltage increases.

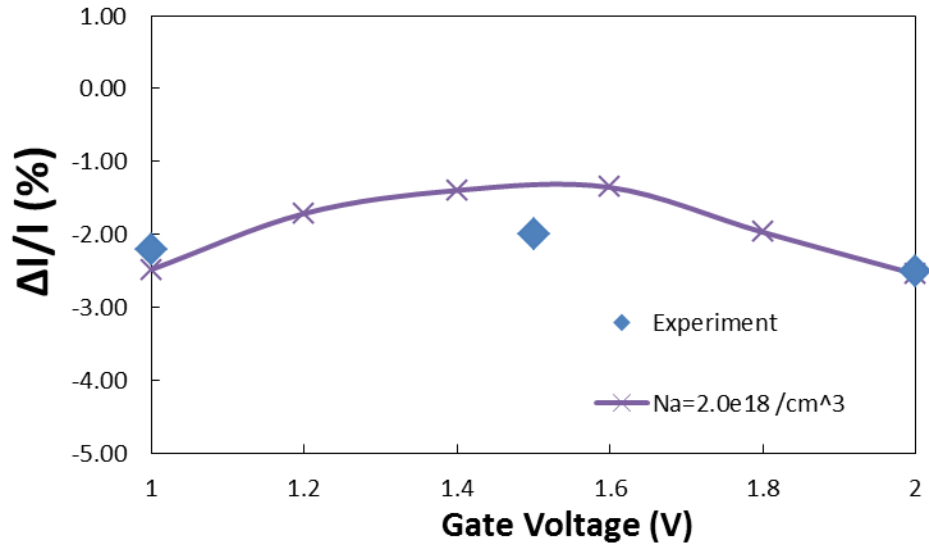
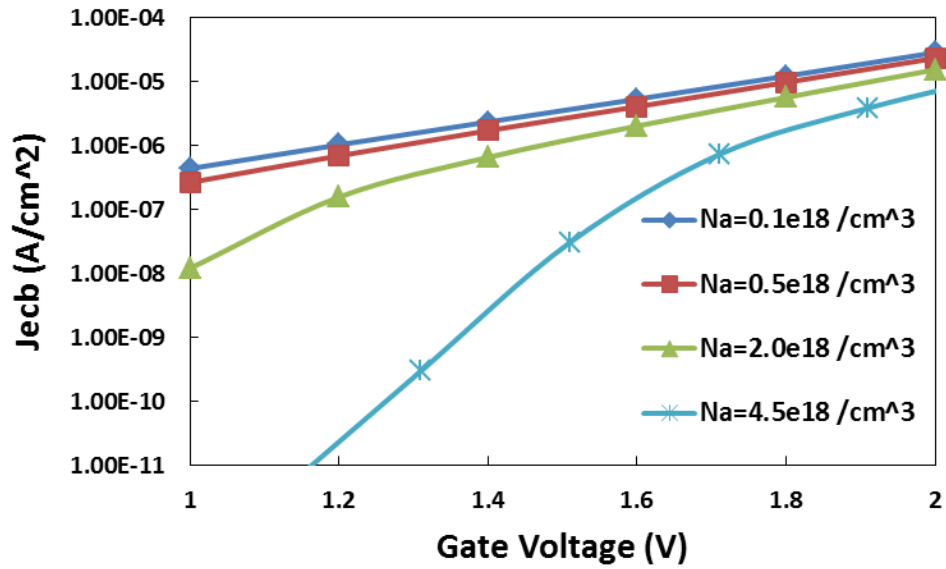


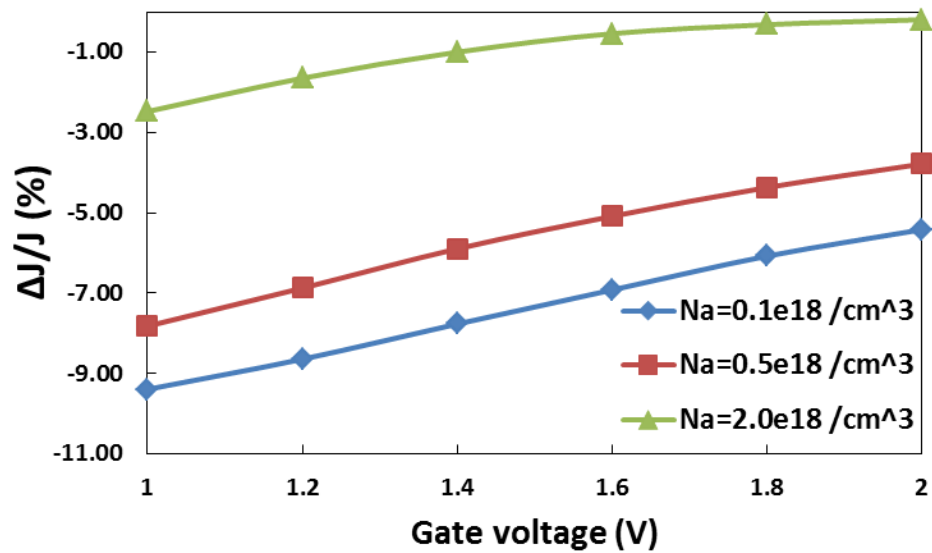
Figure 5.10 Sensitivity vs. gate voltage for total tunneling current. The line is calculated from the model, and the diamonds are the measured experimental results.

### 5.5 Different doping concentration

Doping concentration's influence on sensitivity is studied in this section. Figure 5.11 shows current density and sensitivity vs. gate voltage for ECB for different doping concentration. As doping concentration increases, both current density and sensitivity for ECB decrease.



(a)

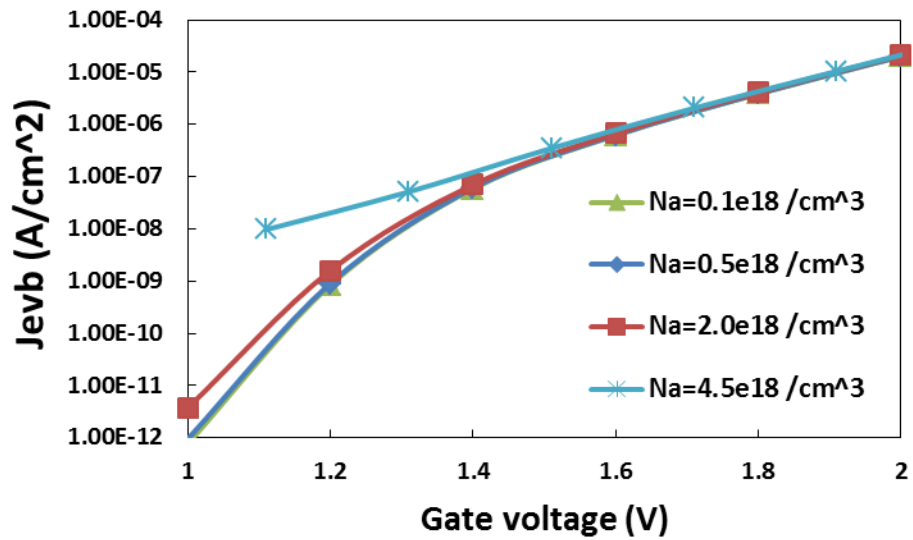


(b)

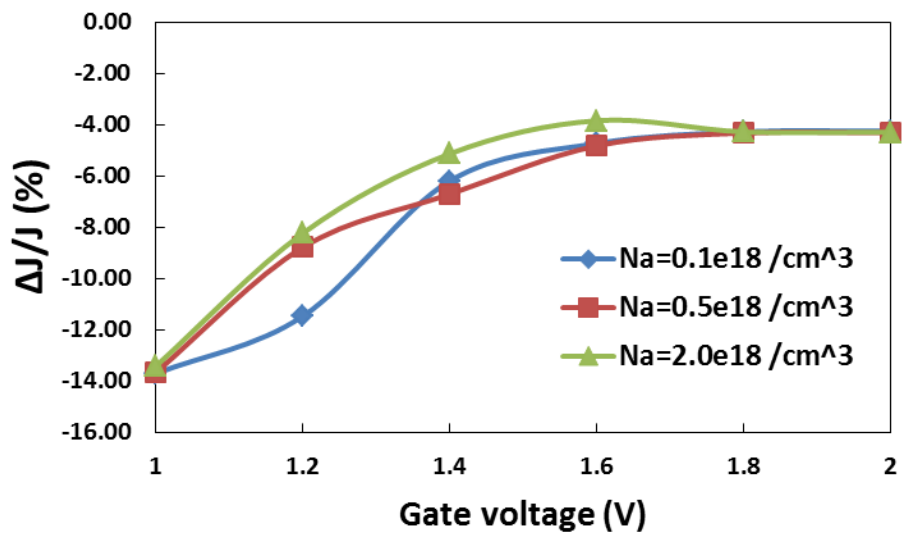
Figure 5.11 ECB modeling for different doping concentration. Parameters are the same as MOS tunneling current strain sensor in DC measurement. (a). Current density vs. gate voltage for ECB; (b). Sensitivity vs. gate current for ECB.

Figure 5.12 shows current density and sensitivity vs. gate voltage for

EVB for different doping concentration. For EVB current density, doping concentration has larger influence at lower voltage, but less influence at higher voltage. For sensitivity, unlike ECB, doping concentration has little influence on EVB.



(a)



(b)

Figure 5.12 EVB modeling for different doping concentration. Parameters are the same as MOS tunneling current strain sensor in DC measurement. (a).

Current density vs. gate voltage for EVB; (b). Sensitivity vs. gate current for EVB.

Figure 5.13 shows the total gate current sensitivity vs. gate voltage at different doping concentration. The same device from MOS tunneling current strain sensor in DC measurement is used here. At low doping concentration, sensitivity decreases as gate voltage increases, which is similar to [55]. At high doping concentration, sensitivity decreases and then increases as gate voltage increases, which is similar to Table 7.

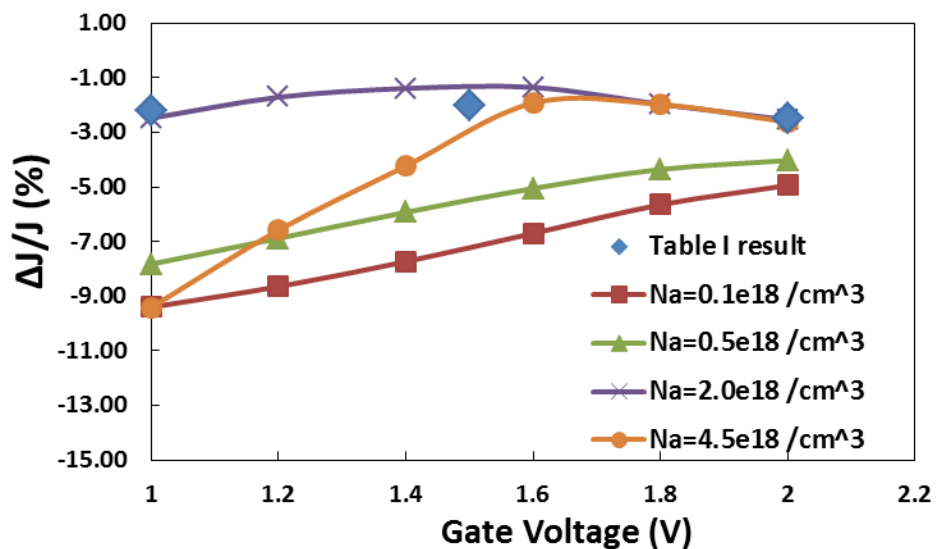


Figure 5.13 Total sensitivity vs. gate voltage at different doping concentration. Parameters are the same as MOS tunneling current strain sensor in DC measurement.

The difference comes from doping concentration, which changes both ECB and EVB and sensitivity. To explain this result, gate voltage and doping concentration are divided into three groups, low doping concentration (0.1e18



and  $0.5e18 / \text{cm}^3$ ), low voltage and high doping concentration ( $2e18$  and  $4.5e18 / \text{cm}^3$ ), and high voltage and high doping concentration.

- 1) At low doping concentration, ECB current density is much larger than EVB current density at low voltage, and comparable to EVB current density at high voltage. In the same time, ECB sensitivity is larger than EVB sensitivity. Therefore, ECB has a larger influence on total gate current sensitivity at low doping concentration, which makes total gate current sensitivity decreases like ECB.
- 2) At low voltage and high doping concentration, ECB is larger than EVB, and its sensitivity is larger than that of EVB, so ECB has a larger influence on sensitivity, which decreases.
- 3) At high voltage and high doping concentration, EVB and ECB becomes comparable, and EVB sensitivity is larger than that of ECB, so EVB sensitivity makes total gate current sensitivity increase.

As doping concentration continues to increase, we should expect that EVB dominates eventually in total MOS tunneling current, and its sensitivity will also eventually dominates which makes total gate current sensitivity decreases.

## **5.6 Summary**

To better understand the sensitivity, we built computationally efficient models for both ECB tunneling current and EVB tunneling current. The computational efficiency comes from the adoption of approximate methods for the sub-bands for ECB tunneling current and WKB method for the tunneling probability for both ECB tunneling current and EVB tunneling current. The modeling results fit both this dissertation and other groups' experiments. From

modeling, it is seen that at low voltages, ECB tunneling current dominates total tunneling current. However, at high voltages, EVB tunneling current becomes very important and comparable to ECB tunneling current, which will influence both total tunneling current and total sensitivity. Substrate doping concentration also changes the total tunneling current and total sensitivity. Therefore, when calculating the sensitivity for a MOS tunneling current strain sensor, it is important to consider both the ECB and EVB tunneling currents, especially for high voltages or high doping concentrations. These results are consistent with the measured results in this dissertation.

## CHAPTER 6

### BULK ACOUSTIC LONGITUDINAL RF RESONATOR BASED ON MOS TUNNELING CURRENT STRAIN SENSOR

#### **6.1 Introduction to RF MEMS resonator**

The measurements in Chapter 4 shows that drift cannot be removed in both DC method and AC method. However, instead of measuring amplitude of MOS tunneling current, we can measure frequency changing by making a resonator sensor based on MOS tunneling current strain sensor.

Resonator has been used vastly in oscillators, filters and sensors [72-77]. Due to its high quality factor (Q), compatibility with CMOS process, low power, low cost batch fabrication and easy to miniaturize, RF MEMS resonator has been attractive alternative to Quartz crystal and SAW devices. RF MEMS resonator can also be integrated to CMOS circuit in one chip to reduce parasitic impedance and time delay for high frequency applications. Quartz crystal resonator and SAW resonator offer a large Q, great temperature stability and high reliability. However they cannot be made on-chip and suffer from poor resistance to shock [78-83].

There are basically three categories of RF MEMS resonator. They are capacitive resonator, piezoelectric and piezoresistive resonators. Capacitive resonator usually actuates resonance using electrostatic force and senses resonance through capacitance changing during resonance. The benefit of

capacitive sensing is low temperature dependence. However the capacitance changes can be extremely small, which can be buried in noise and parasitic capacitance [84-86]. Piezoelectricity is a phenomenon that in some materials an electrical field can be generated when these materials are subject to mechanical deformation. Piezoelectric sensing only applies to applications under non-static strain. Piezoelectric resonators usually adopt metal - piezoelectric material - metal sandwich structure. The most common piezoelectric materials used in RF MEMS resonators are aluminum nitride. The disadvantage of piezoelectric resonators is that it is not able to integrate with IC in one die [87-89]. Piezoresistive sensing detects resistance changing due to resonance. Although the theory and fabrication process of these accelerometers are simple, the temperature sensitivity and poor noise limit the performance [90, 91].

According to shapes, anchors and actuation, there are several different categories of resonators [92]. Table 9 lists some common types of resonators. Each type has several different modes depends on how it is actuated. For example, when the electrode pad of a clamp – free resonator is placed below the beam, beam vibrates up and down. However if the electrode is placed along the beam and at the free end, the beam vibrates longitudinally.

Table 9

## Summary of vibrating shapes

<b>Resonator types</b>	<b>Description</b>	<b>Performance</b>
Clamp – clamp [93]	An electrode is placed in plane or under the clamp – clamp beam to form transducer capacitor.	1 MHz - 100MHz; Q degraded due to anchor dissipation at high frequency.
Clamp – free [94]	The clamp can be at one end or in the middle of the beam.	High Q; lower anchor dissipation.
Free – free [95]	The anchor is located at the vibration node point and suspended by other beams.	10 MHz – 100 MHz; high Q at high frequency.
Square [96]	A square plate is suspended. It can zooming in and out in-plane or vibrate out-of-plane.	10 MHz - 500MHz; high output power; high Q at high frequency.
Disk [97]	A disk plate is suspended. It is like square plate.	20 MHz – 1.5 GHz; high output power;
Ring [98]	A ring is suspended like square plate.	100 MHz – 5 GHz; Q is around 1 K – 10 K.

This chapter proposes a new type of RF MEMS resonator based on MOS tunneling current strain sensor. This new type of RF MEMS resonator will be thoroughly discussed from design, fabrication to measurement.

## **6.2 Bulk Acoustic RF resonator based on MOS tunneling current strain sensor**

The goal is to demonstrate a RF resonator based on MOS tunneling current strain sensor. A simple structure which can provide enough strain is preferred. Therefore, the bulk acoustic resonator, which is easy to fabricate, provides high Q and enough strain is adopted. The following sections will thoroughly discuss this type of resonator, including basic theories about resonators.

### 6.2.1 Principle of bulk acoustic RF resonator

Figure 6.1 shows the 3D structure of a bulk acoustic RF resonator and a schematic showing work principle. In Figure 6.1 (a), the green parts represent beam, electrodes and anchor. The white parts are insulators which isolate beam and electrodes. The yellow part is the substrate. The anchor is located in the middle of the beam, which is the vibration node point. The beam and anchor are normally grounded, while the driving signal is feed on the electrodes on both sides. As shown in Figure 6.1 (b), under electric static force, the two ends of the beam move along opposite direction. One of the benefits of this type of structure is less energy dissipation to anchor and substrate, which leads to high quality factor.

The lowest resonance frequency ( $f_0$ ), effective mass ( $m$ ), damping coefficient ( $\gamma$ ) and the spring constant ( $k$ ) can be expressed as

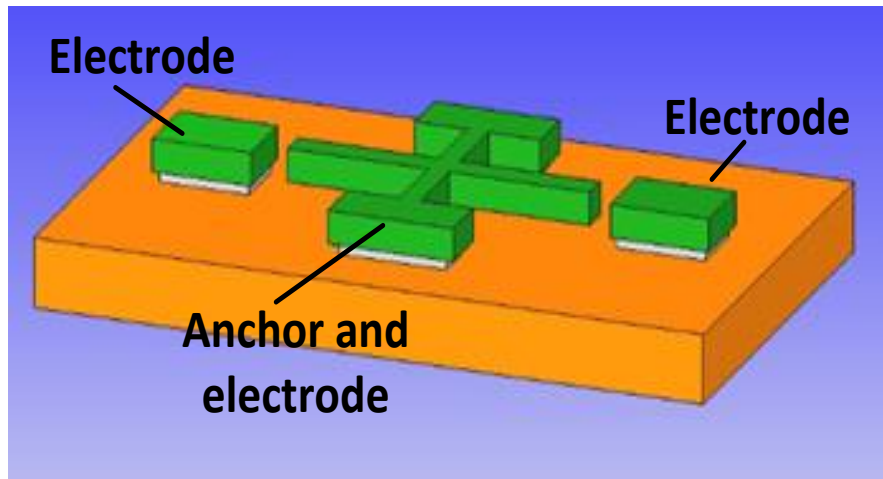
$$f_0 = \frac{1}{2L} \sqrt{\frac{E}{\rho}} \quad (6.1)$$

$$m = \frac{\rho AL}{2} \quad (6.2)$$

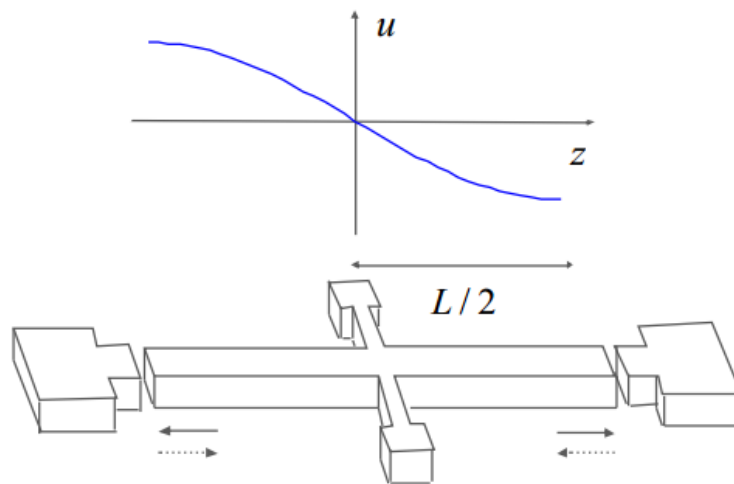
$$\gamma = \frac{bAL}{2} \quad (6.3)$$

$$k = \frac{\pi^2 EA}{2L} \quad (6.4)$$

Where  $\rho$  is the material density,  $A$  is the beam cross sectional area,  $L$  is the length of the beam,  $b$  is the viscous damping losses,  $E$  is the Young's modulus.



(a)



(b)

Figure 6.1 (a) 3D structure of a bulk acoustic RF resonator; (b) a schematic showing working principle of longitudinal mode beam resonator [9].

### 6.2.2 Fabrication of Bulk Acoustic RF resonator based on MOS tunneling current strain sensor

A silicon on insulator (SOI) wafer is used to make the device. The SOI wafer has a lightly doped P-type substrate, a 1  $\mu\text{m}$  thick oxide layer and a 20  $\mu\text{m}$  heavily doped P-type top layer silicon. The resistivity of top layer silicon is

0.01 Ohm-cm, while the resistivity of the substrate is 20 Ohm-cm. It is easy to fabricate a bulk acoustic RF resonator using standard MEMS process on SOI wafer. It is also very easy to make MOS capacitors. Therefore, there is no need to elaborate every process. However, it is very tricky to make a resonator together with a MOS capacitor on the resonator beam. Several issues during fabrication and what we do to solve these issues are discussed here.

- 1) If DRIE is done first to etch silicon to form the resonator, there will be 20  $\mu\text{m}$  thick steps on the surface. It is difficult to spin on photoresist smoothly on such surface, thus it is difficult to pattern MOS capacitors on the beams. Therefore, the MOS capacitors have to be made first
- 2) Another issue is contact. A perfect contact of electrodes between metal gate and silicon requires none oxide and clean silicon surface. Since we thin gate oxide has to be grown for the MOS capacitors, there is also gate oxide grown on the contact pads. One way to remove gate oxide on the contact pads is to use one more mask to pattern a protection layer for MOS capacitors and etch thin gate oxide for electrode, however this step may damage MOS capacitors during BOE. Besides, lift off for metal has to be performed, after sputtering. This step would also damage MOS capacitors. Therefore, gate oxide on the contact pads has to be kept. After the fabrication is completed, a high DC voltage can applied on the contact pads to break this thin oxide.
- 3) Traditionally, people usually do BOE to etch oxide layer in SOI to release resonator beams. Since this step takes several hours, it could be a serious threat to MOS capacitors. Therefore, one more step to etch

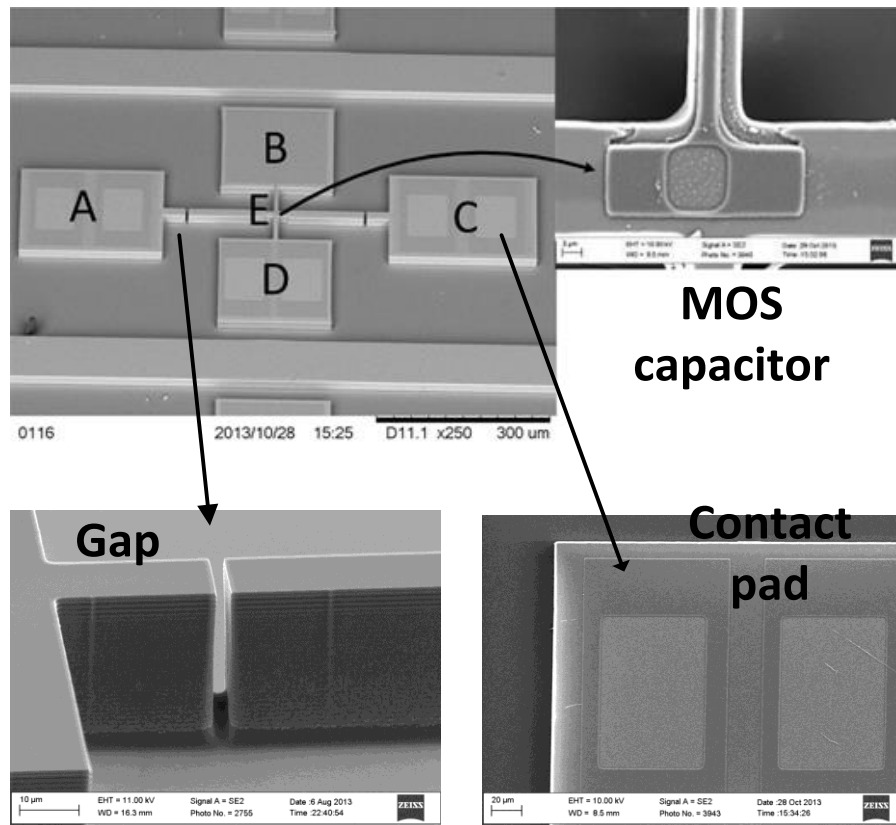


substrate silicon layer to open a window is proposed, which makes the etching oxide layer much faster through the bottom.

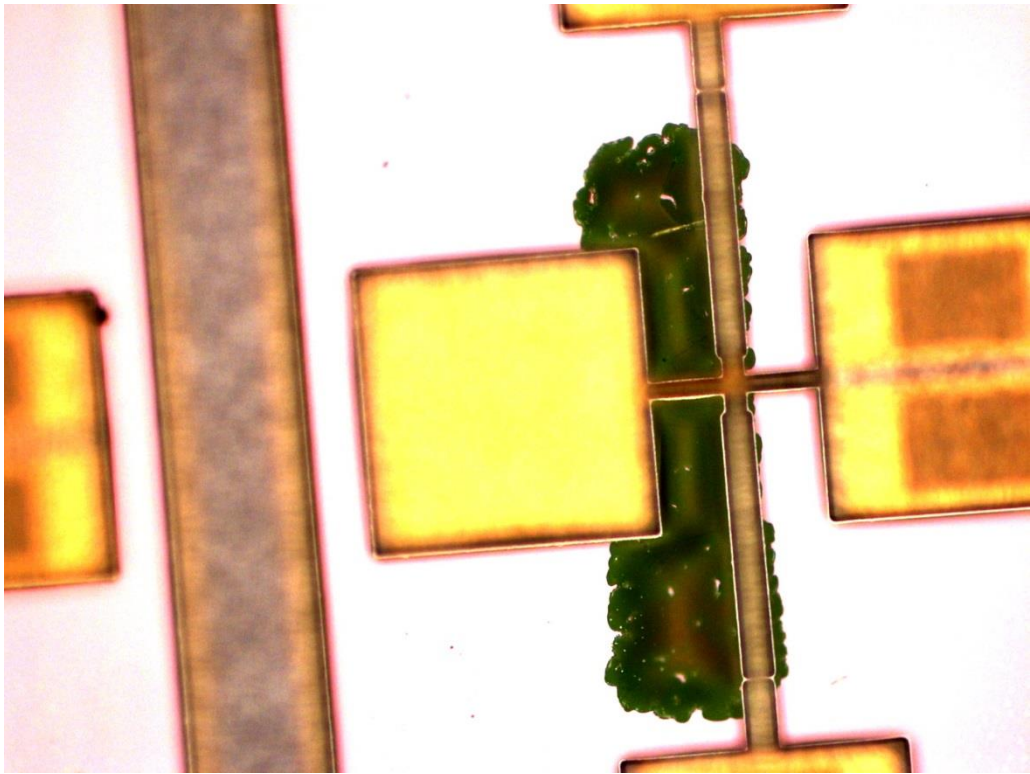
- 4) It is also a problem when comes to which silicon layer to etch first. To etch a 400  $\mu\text{m}$  thick silicon layer, it could take several hours. If we etch bottom layer first, the photoresist on the top layer could be deteriorated badly, which was supposed to be perfect for DRIE for resonators. If the top layer of silicon is etched to form resonators before substrate etch, this long time DRIE could also damage the shape of resonators. A very good protection layer covering top layer after top layer is etch probably a better choice than the deterioration of the photoresist on the top layer. Therefore, it is proposed that top layer is etched first and then the bottom substrate.
- 5) After open a window in the substrate, there are two options to etch the sacrificial oxide layer. One is BOE. Another one is RIE. Both need protection layer. Since some dies could be etched off during DRIE, it is difficult to spin photoresist layer as a protection layer. Therefore, a crystal bond is used as the protection layer. BOE will not attack silicon, so it can preserve the shapes of resonators. RIE is an isotropic way to etch  $\text{SiO}_2$  which also etches silicon more or less depending on the precursors, so RIE could damage the devices. Therefore, BOE is chosen to etch sacrificial layer of SOI wafer.

As a summary of the process, first, the MOS capacitors are made and then make resonators. When the resonators are made, the top layer is etched first and then substrate layer. Both use DRIE. Before etching the sacrificial layer in BOE, the top layer is covered with crystal bond. In the end, acetone is

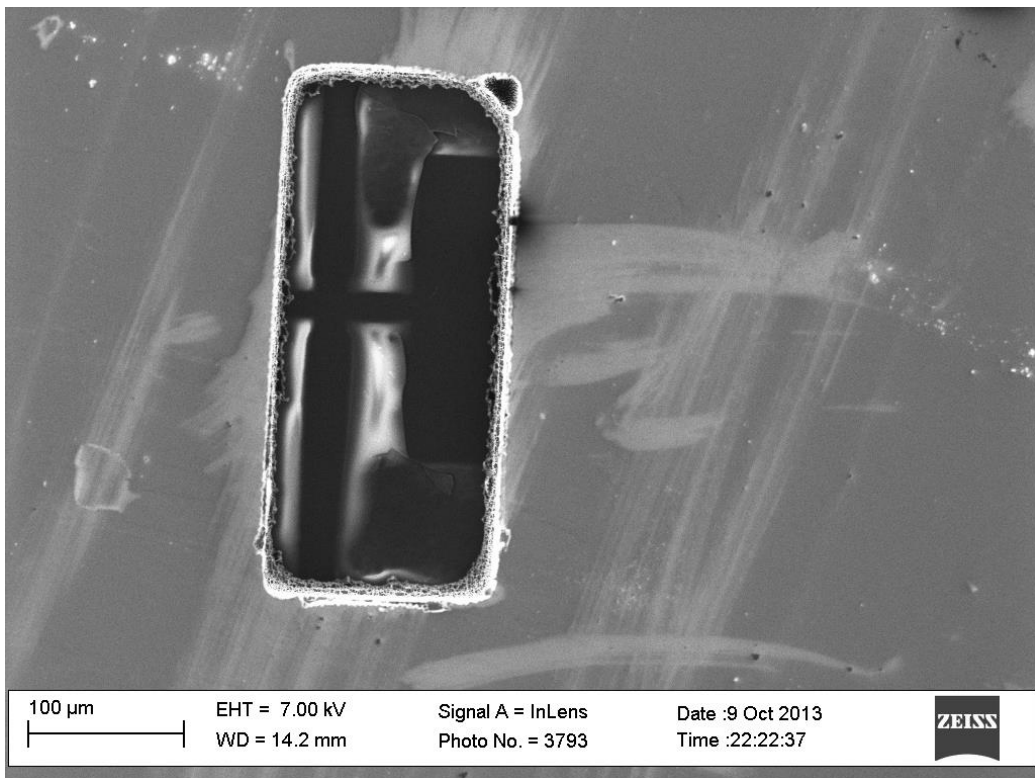
used to remove crystal bond. However, it should be pointed out that every step in DRIE and BOE could damage MOS capacitors. Figure 6.2 (a) shows the resonators with MOS capacitors before the sacrificial layer is etched. Figure 6.2 (b) to Figure 6.2 (d) shows the final device. Unfortunately, there is a misalignment between top layer and the substrate. The resonator should be located in the middle of the substrate window. The misalignment comes from misalignment of the optical system of bottom side alignment (BSA) in Karl SUSS Mask Aligner MA6/BA6. This misalignment of the optical system should not happen, if a routine maintenance is carried. This misalignment make most beams' release fail, like devices in Figure 6.2 (b) & (c). Even if some beams are released fully, the resonators could suffer from energy dissipation to anchors due to loss of symmetry, like device in Figure 6.2 (d). Figure 6.2 (e) shows the packaged device for testing.



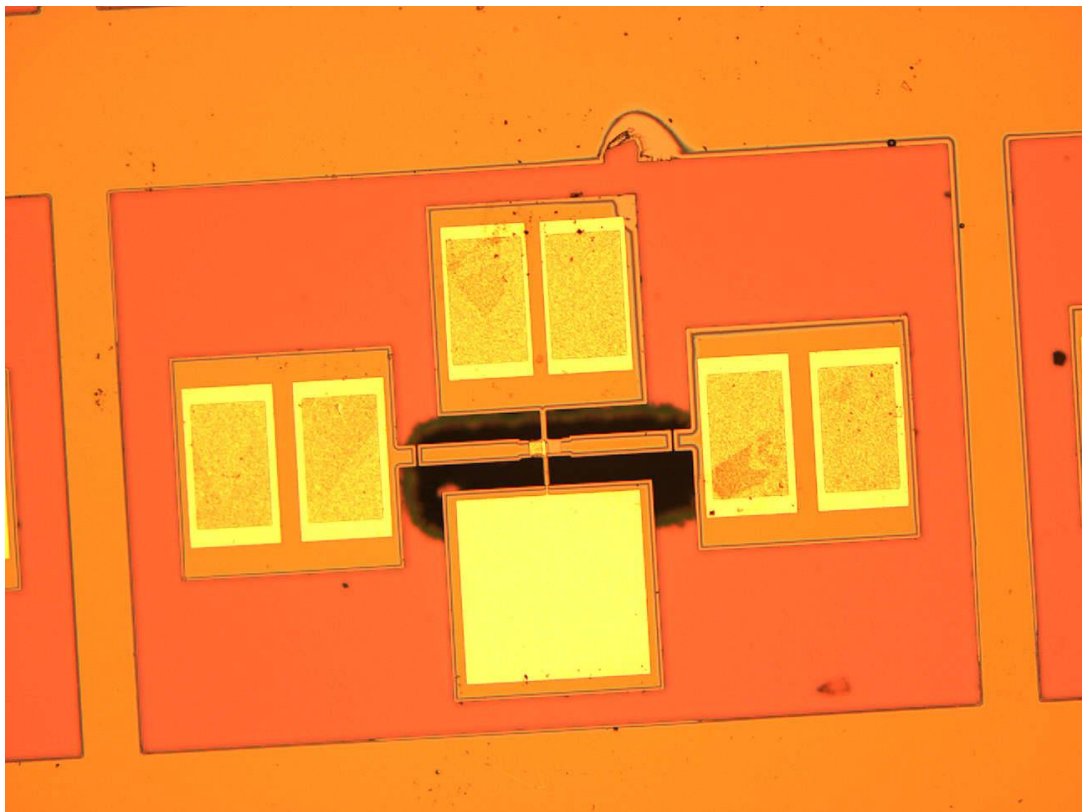
(a)



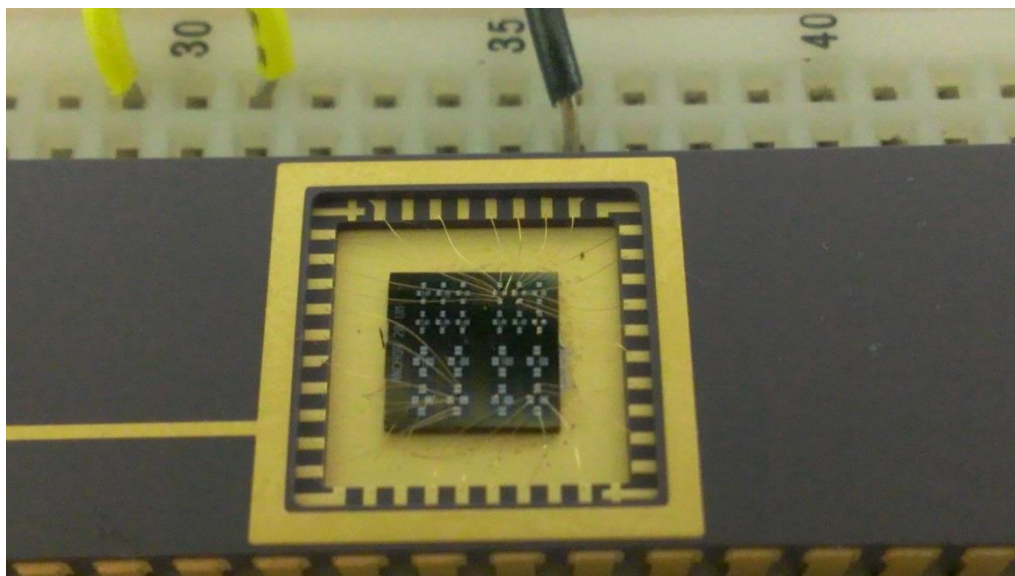
(b)



(c)



(d)



(e)

Figure 6.2 SEM picture and microscope picture of fabricated devices. (a) SEM pictures for top layer before etching sacrificial layer of SOI wafer. (b)

Optical microscope picture for the final device which is misaligned and not fully released. (c) SEM picture of substrate layer for the final device which is misaligned. (d) Optical microscope picture of the final device which is misaligned but full released. (e) Packaged devices for testing.

In Figure 6.2 (a), the contact pads for the AC driving voltage are labelled as A & C, pad B is DC input on the MOS capacitor, pad D is the ground, and E is the place where the MOS capacitor is. Aluminum on pads A, C & D is sputtered onto a thin oxide which will be broken through high voltage. Between aluminum and silicon on pad B, there is a 315 nm thick SiO<sub>2</sub>. Table 10 gives dimensions of the resonator. On each die, there are several devices. There are two grounds on the device. One is pad D, and another one is the substrate layer on the bottom. A ground on the substrate layer is necessary to minimize the driving voltage crosstalk with pad B & D through the substrate layer.

Table 10

Parameters of the resonator

Parameter	Definition	Value
L	The length of pads	340 $\mu\text{m}$
L1	The length of Al contact of pad B	300 $\mu\text{m}$
T1	The thickness of oxide layer of SOI wafer	1 $\mu\text{m}$
T2	The thickness of oxide layer of pad B	315 nm
l	The length of beam	310 $\mu\text{m}$
w	The width of beam	35 $\mu\text{m}$
h	The height of beam	20 $\mu\text{m}$
g	The gap between beam and pad A or C	2 $\mu\text{m}$
LL	The length of one die	6 mm

An equivalent circuit for MOS tunneling current sensing method including equivalent circuit for resonator, driving circuit and parasitic components is shown in Figure 6.3. Table 11 explains the definition of the components in the equivalent circuit, and gives the theoretical number from fabrication. Here A, B, C and D in the definition mean silicon on these pads.

Table 11

Definition of components used in equivalent circuit

Component	Definition	Value
Ca	Capacitor between A and resonator beam	3.1 fF
Cag	Capacitor between A and handler layer	4 pF
Cbb	Capacitor between Aluminum contact and beam on pad B	9.861 pF
Cbdg	Capacitor between B and handler layer in parallel with capacitor between D and handler layer	8 pF
Cc	Capacitor between C and beam	3.1 fF
Ccg	Capacitor between C and handler layer	4 pF
Cg	Capacitor between handler layer and package	400 pF
Cmos	The MOS capacitor between B and beam	6.9 pF, 17.2 pF, 20.7 pF, 100.1 pF (Dependent on area)
Rmos	The MOS capacitor's resistance	Dependent on area & voltage
Rg	The resistor between substrate and package	>220 (10 MHz)
R1	The resistor at the DC input	Best close to Rmos

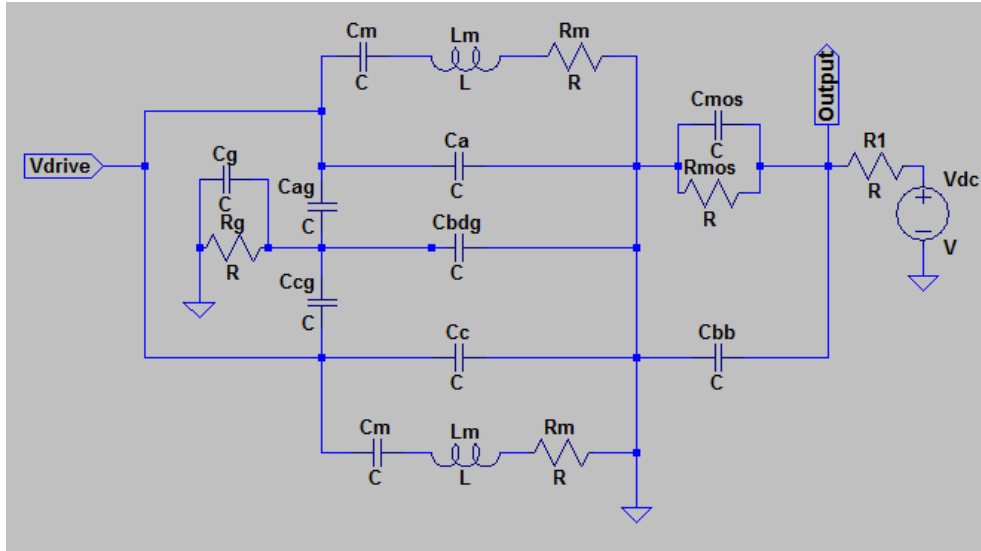


Figure 6.3 Equivalent circuit for MOS tunneling current sensing method.

$C_{mos}$  depends on the area of MOS capacitors and thickness of gate oxide. Here they are calculated for 2 nm thick gate oxide and several different areas.  $R_{mos}$  not only depends on the area of MOS capacitors and thickness of gate oxide, but the gate voltage, since gate voltage vs. tunneling current is not linear.

The resistor at the DC input,  $R_1$ , should be chosen carefully to output a detectable AC voltage. Assuming DC supply is  $V$  and  $R_{mos}$  equals  $R(1 + \alpha \cos \theta)$  at resonance, where  $\theta = 2\pi f t$ ,  $\alpha$  is related to stress, which is far less than 1. Thus,

$$V_{mos} = V \frac{R_{mos}}{R_{mos} + R_1} = V \frac{R(1 + \alpha \cos \theta)}{R(1 + \alpha \cos \theta) + R_1} \quad (6.5)$$

If  $R \gg R_1$ ,

$$V_{mos} = V \quad (6.6)$$

If  $R \ll R_1$ ,

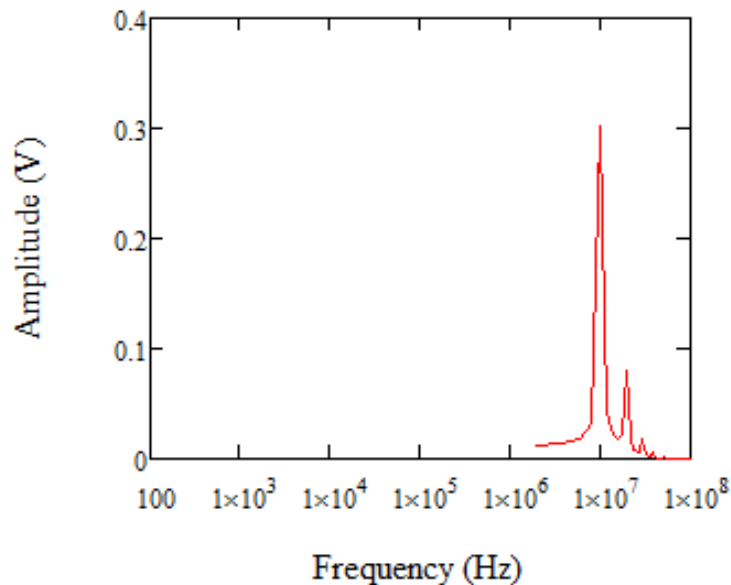
$$V_{mos} = V \frac{R(1 + \alpha \cos \theta)}{R_1} \quad (6.7)$$

The AC component is very small, and it makes measurement difficult especially with RF crosstalk present.

If  $R \approx R_1$ ,

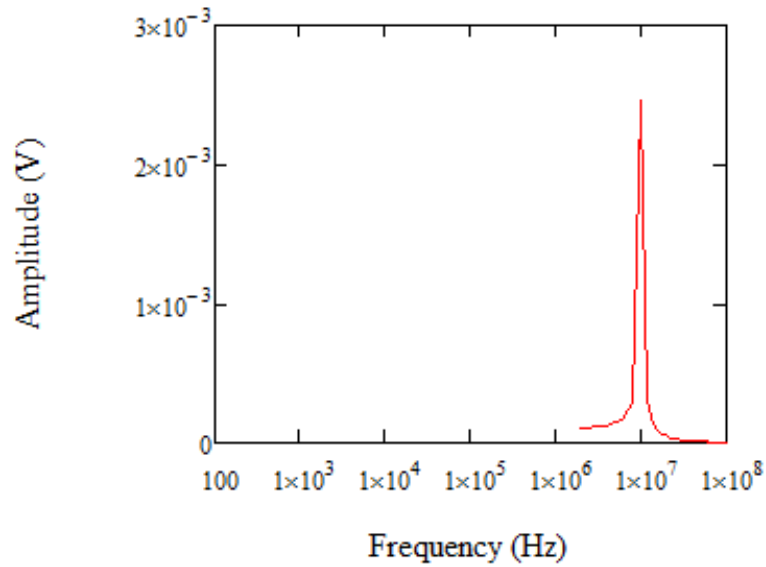
$$V_{mos} = V \frac{1 + \alpha \cos \theta}{2 + \alpha \cos \theta} = V - V \frac{1}{2 + \alpha \cos \theta} \quad (6.8)$$

This output distorts the pure sine wave of AC output and induces harmonics. The output spectrum of this output in the frequency domain can be analyzed using FFT. Assuming  $f = 10 \text{ MHz}$ ,  $V = 1 \text{ V}$ , the output spectrum is shown in Figure 6.4. In Figure 6.4 (a), when  $\alpha \gg 1$ , the harmonics are present. In Figure 6.4 (b), when  $\alpha \ll 1$ , the harmonics are depressed and the output is an almost pure sine wave. In most cases,  $\alpha$  is far less than 1. Therefore, it is best to choose a resistance close to the MOS capacitor's resistance.



(a)





(b)

Figure 6.4 The output spectrum when  $R \approx R_1$ . (a)  $\alpha \gg 1$ . (b)  $\alpha \ll 1$ .

### 6.2.3 Bulk acoustic RF resonator testing

This section discusses testing setup for the bulk acoustic RF resonator. The resonator is made to demonstrate the sensing method using MOS tunneling current strain sensor. However, the resonator can also work as a capacitive resonator. The resonator will be tested first using the traditional capacitive sensing method, and then using MOS tunneling current strain sensor way.

Figure 6.5 gives the measurement setups for capacitive sensing and MOS tunneling current sensing. A RF impedance analyzer Hp4294a is used to measurement the resonator. The schematic in Figure 6.5 (a) shows the setup for capacitive sensing method. Hp4294a outputs both DC bias and AC voltage from the connectors of Hpot and Hcur to the left and right electrodes. The connectors of Lpot and Lcur receive signal from the top electrode which

is in contact with beam. The schematic in Figure 6.5 (b) shows the set up for MOS tunneling current sensing method. The driving signal is supplied by a network analyzer and a DC source in the right of the schematic. The DC source in the left of the schematic is applied to the MOS capacitor, and tunneling current through the MOS capacitor is fed into the network analyzer. Figure 6.5 (c) is the picture of measurement set up for the capacitive sensing method. The device is put on a breadboard and put in an aluminum vacuum box. The aluminum box has vacuum BNC connectors to the outside instruments.

Next, the motional resistance  $R_m$ , the motional capacitance  $C_m$ , and the motional inductance  $L_m$  for equivalent circuit of resonator are defined. They can be expressed as

$$R_m = \frac{\sqrt{km}}{Q\eta^2} \quad (6.9)$$

$$C_m = \frac{\eta^2}{k} \quad (6.10)$$

$$L_m = \frac{m}{\eta^2} \quad (6.11)$$

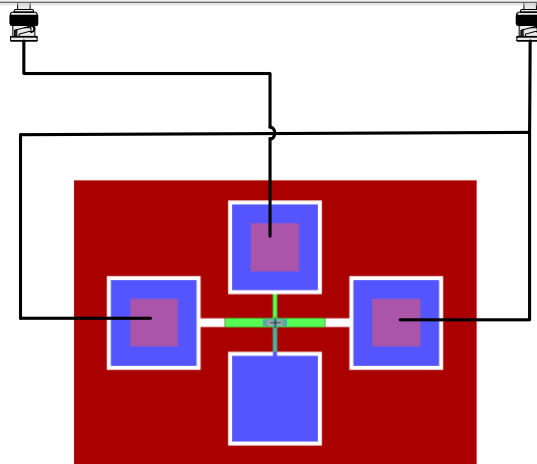
Where  $\eta$  is the electromechanical transduction factor, which relates vibration velocity to the motional current or the ac voltage to the actuation force. For the capacitive sensing method,  $\eta$  can be expressed as

$$\eta \approx V_{dc} \frac{\varepsilon A}{g^2} \quad (6.12)$$

Where  $\varepsilon$  is the permittivity,  $A$  is the cross section area,  $V_{dc}$  is the dc bias,  $g$  is the distance between beam and electrode pad. Assuming  $V_{dc} = 50 V$  and  $Q = 1.8e15$  [85], according to the parameters in Table IX and equations (6.1) – (6.4) and (6.9) – (6.12), we can get  $f_0 = 13.643 MHz$ ,

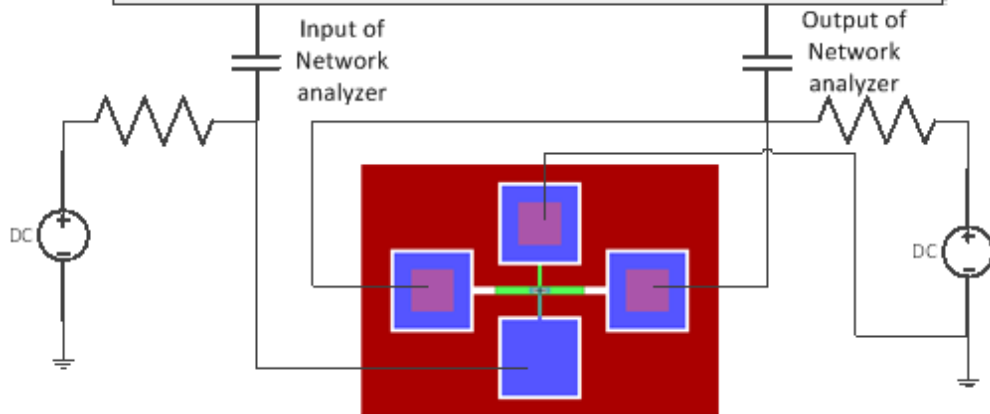
$R_m = 10.038 M\Omega$ ,  $C_m = 0.006456 aF$  and  $L_m = 21080H$ .

# RF impedance analyzer



(a)

# Network Analyzer



(b)



(c)

Figure 6.5 Schematic for measurement set up. (a) Capacitive sensing method measurement set up. (b) MOS tunneling current sensing method measurement set up. (c) Picture of the measurement set up.

#### 6.2.4 Testing and discussion

Unfortunately, the first try to make a bulk acoustic resonator based on MOS tunneling strain sensor was not successful. The MOS capacitors are broken, which were good before DRIE. There is a very large possibility that MOS capacitors can be damaged during DRIE and sacrificial layer etching as discussed in Section 6.2.2. However, even the capacitive sensing method doesn't work. Here several facts that could make the capacitive sensing test fail are listed.

- 1) Degraded Q due to misalignment. One of the benefits of this design is the driving force symmetrically actuate the beam and anchor is located at the vibration node point. However due to misalignment, the symmetry could be degraded.

- 2) Cross-talking in testing circuit. A breadboard is used in test, which is not a good choice for RF testing, but should be fine for 10MHz. Short and neat wiring, plus grounding all unused pins should prevent large cross-talking. Replacing device with resistor shows that there is very little cross-talking in testing circuit.
- 3) Cross-talking in device. There is always cross-talking through substrate. Usually substrate should be grounded to minimize this cross-talking. However, we didn't sputter any metal on the bottom of the substrate, but used conductive epoxy to glue device to package. This conductive epoxy works well for DC measurement, but could be a problem for RF measurement.

Among all of these three facts, cross-talking in device is the most suspicious one. The device is pasted to the package by silver epoxy, which contact impedance is unknown. A RF impedance analyzer, Hp4294a, is used to measure the impedance on the substrate. Three groups of capacitance and resistance, A or C to Bottom, B to Bottom and D to Bottom (refer to Figure 6.2 (a) and Table 10 for definitions) are measured. The results are shown in Table 12. From A (or C) to Bottom, we can see that the capacitance keeps consistent and is close to  $C_{ag}$  or  $C_{cg}$  from Table 10, but the resistance decreases with increasing frequency. The resistance from B to Bottom and D to Bottom are close to A or C to Bottom. The capacitance is almost twice of A or C to Bottom, because B and D are connected through beam.

Table 12

Measurement results for substrate impedance

	Frequency (Hz)	R ( $\Omega$ )	C (pF)
A (or C) to Bottom	50K	8K	4.85
	100K	6.6K	4.75
	1000K	667	4.5
	10 M	331	4.4
	B to Bottom	1000K	459
	10 M	220	7
D to Bottom	1000K	344	8.6

From Table 12, it is found that at 10 MHz, the substrate resistance is at least 220  $\Omega$ . This resistance can come from the resistance of substrate itself, or the contact on the bottom of substrate. However COMSOL can be used to verify that the resistance of substrate itself is small. Figure 6.6 shows the modeling results. The total current is calculated using surface integration of the current density, which is 0.054 A at 1 V. Therefore the resistance is around 18  $\Omega$ . Therefore this high resistance comes from the poor contact on the bottom of substrate.

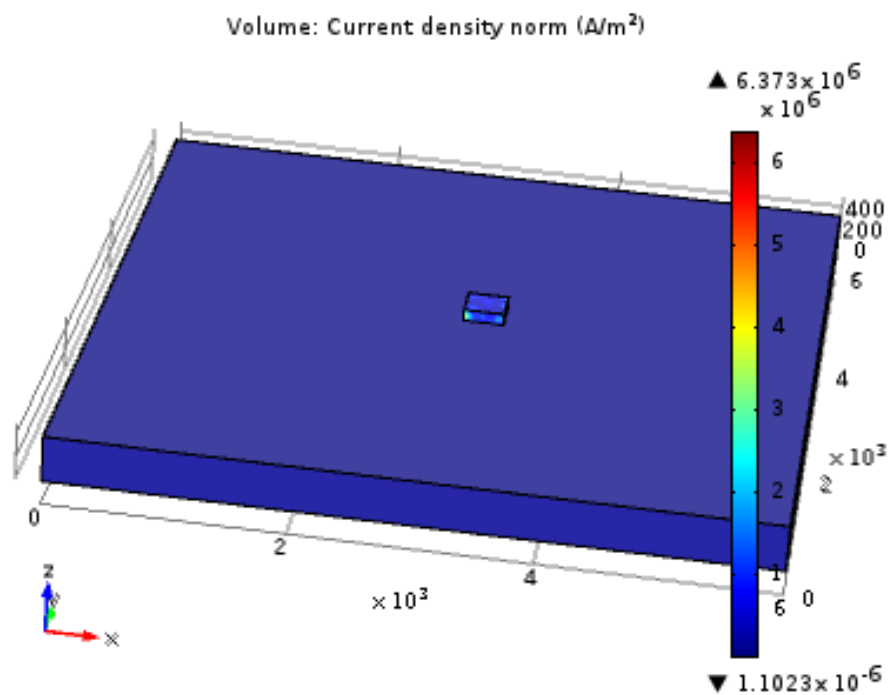
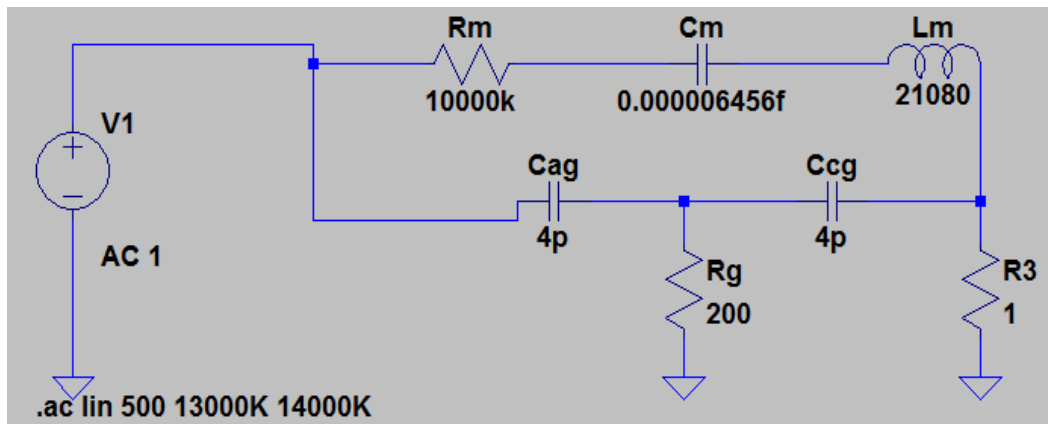
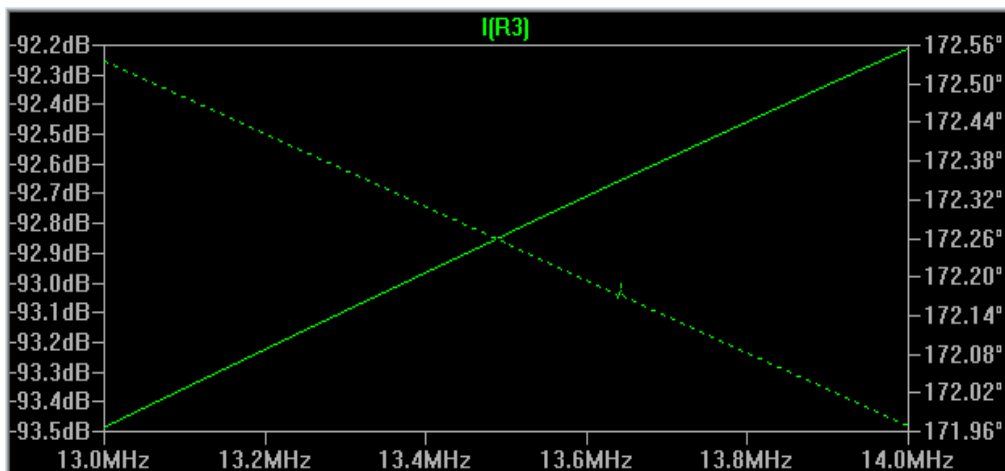


Figure 6.6 COMSOL modeling. The top bulk is contact which is  $340\ \mu\text{m}$  (x) \*  $340\ \mu\text{m}$  (y) \*  $100\ \mu\text{m}$  (z). The bottom bulk is Silicon which is  $6\text{mm}$  (x) \*  $6\text{mm}$  (y) \*  $400\ \mu\text{m}$  (z). The voltage is  $1\ \text{V}$ .

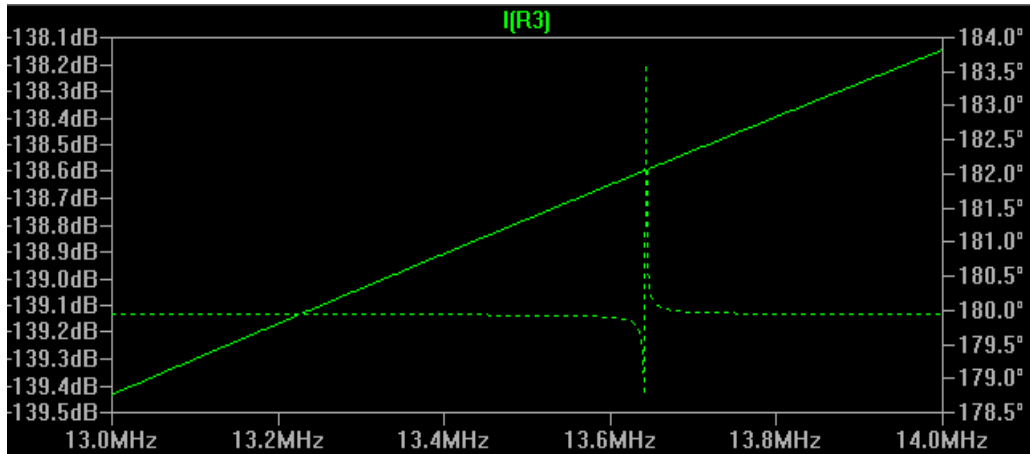
A SPICE simulation is used to find out why this high substrate contact resistance hinders the capacitive sensing testing. Figure 6.7 (a) shows a simplified equivalent circuit for capacitive sensing. R3 is the output. Figure 6.7 (b) shows the simulation result with  $R_g = 200\ \Omega$ . It is clear that the response is so small that it is easy to be buried in noise. Figure 6.7 (c) shows the simulation result with  $R_g = 1\ \Omega$ , which has a larger output.



(a)



(b)



(c)

Figure 6.7 Spice modeling of substrate contact influence on capacitive sensing method. (a) Equivalent circuit for capacitive sensing method. R3 is the output. (b) Simulation result with  $R_g = 200 \Omega$ . (c) Simulation result with  $R_g = 1 \Omega$ .

### 6.3 Suggestions for improvement in future

Although the first try is not successful, some useful tips for next try are learned. To easily measure resonance using the capacitive method, the impedance of the substrate contact has to be reduced. This can be done by sputtering metal on the bottom instead of using conductive epoxy. The area of contact pads can also be reduced to reduce cross-talking among them. The motional resistance  $R_m$  can be reduced by increasing the electromechanical transduction factor  $\eta$  or reducing the effective mass. Since the goal is to make an RF resonator based on a MOS tunneling current strain sensor, the most important thing is to protect MOS capacitors during DRIE and sacrificial layer etching. Perhaps some process protocols from integrated CMOS-MEMS products can be adopted to protect MOS capacitors.



## CHAPTER 7

### CONCLUSIONS AND FUTURE DIRECTIONS

#### 7.1 Conclusions

MEMS strain sensors have been widely researched and commercialized for decades, which can be used in pressure sensor, accelerometer and gyroscope. Nowadays, portable electronics have an increasing requirement for low power sensors, which motivates our research on MOS tunneling current strain sensor. Due to high resistivity of gate oxide, the tunneling current can be in the nano-amp range, which is a good alternative for low power sensing. In this dissertation, a low power MOS tunneling current strain sensor is demonstrated. In the experiment, the noise, sensitivity and drift are characterized. A computationally efficient model for MOS tunneling current is built, which fits this dissertation's experiments as well as other groups' experiments. A bulk acoustic RF resonator based on MOS tunneling current strain sensor is also made. The resonator doesn't work. The reasons why the resonator does not work are discussed, and possible modifications for future research are proposed. In conclusion, the main contributions of this dissertation can be summarized as:

- 1) A low power strain sensor was made. From DC measurement, it is found that the minimum detectable strain with regards to noise and sensitivity. It is also found that the gauge factor of MOS

tunneling current strain sensor is in the range of piezoresistive strain sensor.

- 2) In DC measurement, the MOS tunneling current strain sensor is studied thoroughly from positively bias to negatively bias. With regards to noise, it is found that the device performs best in the inversion region.
- 3) The current drift in MOS tunneling current is studied at different biases. It is found that at different bias, drift behaves different. At high bias, the drift rate is large and MOS tunneling current increases. At low bias, MOS tunneling current decreases.
- 4) A lock-in amplifier is used to perform AC measurement to characterize MOS tunneling current strain sensor. It is found that sensitivity of AC method is close to DC method, but AC method is more efficient in reducing noise than DC method. As for drift, it is found that it is impossible to remove drift using AC method.
- 5) Computationally efficient models are built for MOS tunneling current considering both ECB tunneling current and EVB tunneling current. The computational efficiency comes from the adoption of approximate methods for the sub-bands for ECB tunneling current and WKB method for the tunneling probability for both ECB tunneling current and EVB tunneling current. The model fits experimental results well. It is found that it is acceptable for current density modeling if only ECB tunneling current is considered like other groups did. However, when substrate doping concentration is large, EVB tunneling current has to be included for sensitivity study.

6) A bulk acoustic RF resonator based on MOS tunneling current strain sensor is made. Although the resonator did not work, possible reasons for not working are discussed, which is helpful for future research. From this first try, it is also found that which processes are critical.

## **7.2 Future directions**

Directions of future research are proposed and discussed in this section. They are sensitivity study at different stresses, bolometer based on MOS tunneling current and continuing research on RF resonator based on MOS tunneling current strain sensor.

### **7.2.1 Sensitivity study at different stresses**

The purpose of sensitivity study at different stresses is to improve the performance of the sensors. The minimum detectable strain is determined by both the sensitivity and the noise. Increasing the sensitivity and lowering the noise both can achieve a smaller the minimum detectable strain. Making very high quality ultrathin SiO<sub>2</sub> is the fundamental way to reduce noise. It requires very high quality of wafers, very precise control of gas flow rate, temperature and ultra-low contaminations, which is very time consuming. Therefore an alternative approach is to study sensitivity at stresses along different orientations. Silicon at different type of stresses may cause different changes to the band structure, which will change the sensitivity of tunneling current response to stress.

The setup of the experiment is shown in Figure 7.1. A (001) wafer with MOS devices arranged circularly is laid on an O-ring. A micrometer presses the center of the wafer to introduce stress to the wafer, so stresses at different

directions will be applied to MOS devices at different locations. Tunneling current is measured by a semiconductor parameter analyzer.



Figure 7.1 Setup for sensitivity study at different stresses.

### 7.2.2 Continuing research on RF resonator based on MOS tunneling current strain sensor

Some ideas are learned from this first failure try on RF resonator based on MOS tunneling current strain sensor.

- 1) It is best to make a capacitive resonator without MOS tunneling current strain sensor. This capacitive resonator can be used to verify whether the resonator will resonate. Without MOS tunneling strain sensor, process will be simple and it is easy to control process quality.
- 2) Reduce contact pads to reduce parasitic capacitors which will then decrease cross-talking.

- 3) Use a SOI wafer with both top layer and substrate layer heavily doped. This can decrease resistance in the substrate, which also helps reduce cross-talking.
- 4) Use SOI wafer with a thinner top layer which will make DRIE much easier, and in the same time decreases motional resistance.
- 5) To easy measure resonance using capacitive method, we need to reduce the impedance of substrate contact. Sputtering metal on the bottom instead of using conductive epoxy is necessary.
- 6) Since the goal is to make a RF resonator based on MOS tunneling current strain sensor, the most important thing is to protect MOS capacitors during DRIE and sacrificial layer etching. Perhaps some process protocols from integrated CMOS-MEMS products can be adopt to protect MOS capacitors.

### **7.3 Bolometer based on MOS tunneling current**

During the research, it is found that MOS tunneling current is also very temperature sensitive, which makes it a potential technology for bolometer. There are several facts about MOS tunneling current's response to temperature changing:

- 1) For ultrathin gate oxide, there are two main MOS tunneling current. Above 348 K, MOS tunneling current exponentially depends on  $1/T$ , which means thermionic type of emission dominates. Below 348 K, MOS tunneling current weakly depends on temperature, which means direct tunneling current dominates [26].
- 2) Another fact is that the thinner the gate oxide and the lower the doping concentration, the higher sensitive the direct tunneling

current responses to temperature changing [99].

- 3) The third fact is that MOS capacitor at low electric field gives more sensitive to temperature changing [100].

Figure 7.2 lists parameters of some commercial and state-of-art uncool infrared bolometers. Table 13 gives some measurement results using the MOS capacitors. The measurement is done using a temperature controllable vacuum chamber and a semiconductor parameter analyzer. To achieve at least the performance of the existing bolometers, future research needs to reduce noise by growing high quality gate oxide or increase MOS tunneling current response to temperature.

*Table 1: Commercial and state-of-the-art R&D uncooled infrared bolometer arrays.*

Company	Bolometer type	Array format (pixels)	Pixel pitch ( $\mu\text{m}$ )	Detector NETD (F=1, 20-60 Hz)
FLIR, USA	VO <sub>x</sub> bolometer	160x120 - 640x480	25	35 mK
L-3, USA	VO <sub>x</sub> bolometer	320x240	37.5	50 mK
	$\alpha$ -Si bolometer	160x120 - 320x240	30	50 mK
BAE, USA	VO <sub>x</sub> bolometer	320x240 - 640x480	28	30-50 mK
	VO <sub>x</sub> bolometer (standard design)	160x120 - 640x480	R&D: 17	50 mK
DRS, USA	VO <sub>x</sub> bolometer (umbrella design)	320x240	25	35 mK
	VO <sub>x</sub> bolometer (umbrella design)	320x240	R&D: 17	50 mK
Raytheon, USA	VO <sub>x</sub> bolometer	320x240 - 640x480	25	30-40 mK
	VO <sub>x</sub> bolometer (umbrella design)	640x512	R&D: 17	50 mK
ULIS, France	$\alpha$ -Si bolometer	160x120, 640x480	25-50	35-100 mK
Mitsubishi, Japan	Si diode bolometer	320x240	25	50 mK
NEC, Japan	VO <sub>x</sub> bolometer	320x240	23.5	75 mK
SCD, Israel	VO <sub>x</sub> bolometer	384x288	25	50 mK

Figure 7.2 Table of commercial and state-of-the-art R&D uncooled infrared bolometers.

Table 13

### Experiment result

Devices	NETD
3.9 nm gate oxide, aluminum gate	290 mK
3.9 nm gate oxide, nickel gate	110 mK

## REFERENCES

- [1] R. Bogue, "MEMS sensors: past, present and future," *Sensor Review*, vol. 27, pp. 7-13, 2007.
- [2] A. A. Barlian, W. T. Park, J. R. Mallon, A. J. Rastegar, and B. L. Pruitt, "Review: semiconductor piezoresistance for microsystems," *Proceedings of the IEEE*, vol. 97, pp. 513-52, 2009.
- [3] "The Future of MEMS by Dr. Thomas F. Marinis: <http://sem.org/PDF/s01p01.pdf>."
- [4] W. P. Eaton and J. H. Smith, "Micromachined pressure sensors: review and recent developments," *Smart Materials and Structures*, vol. 6, pp. 530-9, 1997.
- [5] S. Garcia-Alonso, T. Bautista, J. Sosa, J. M. Monzon-Verona, F. J. Santana-Martin, V. Navarro-Botello, *et al.*, "Low-power MEMS pressure sensor for wireless biomedical applications," in *2011 IEEE 54th International Midwest Symposium on Circuits and Systems (MWSCAS 2011)*, 7-10 Aug. 2011, Piscataway, NJ, USA, 2011, p. 4 pp.
- [6] A. A. S. Mohammed, W. A. Moussa, and E. Lou, "Mechanical strain measurements using semiconductor piezoresistive material," in *2006 International Conference on MEMS, NANO, and Smart Systems*, 27-29 Dec. 2006, Piscataway, NJ, USA, 2006, pp. 5-6.
- [7] L. Zhu and S. McNamara, "Low power strain sensing using tunneling current through MOS capacitors," in *IEEE Solid-State Sensor and Actuator Workshop*, Hilton-Head, 2012, pp. 457-460.
- [8] M. Gad-el-Hak, "MEMS: Applications (The MEMS Handbook, Second Edition)," 2009.
- [9] V. Kaajakari, *Practical MEMS: Design of microsystems, accelerometers, gyroscopes, RF MEMS, optical MEMS, and microfluidic systems*: Small Gear Publishing, 2009.

- [10] S. Patra and T. K. Bhattacharyya, "Highly sensitive tunneling accelerometer for low actuation voltage operation," in *9th IEEE Sensors Conference 2010, SENSORS 2010, November 1, 2010 - November 4, 2010*, Waikoloa, HI, United states, 2010, pp. 1192-1197.
- [11] Y. Chingwen and K. Najafi, "Bulk-silicon tunneling-based pressure sensors," in *Technical Digest Solid-State Sensor and Actuator Workshop, 13-16 June 1994*, Cleveland Heights, OH, USA, 1994, pp. 201-4.
- [12] M. Min, H. Qifang, H. Yilong, D. Haifeng, W. Ling, S. Yunbo, *et al.*, "A bulk micromachined Si-on-glass tunneling accelerometer with out-of-plane sensing capability," in *2007 2nd IEEE International Conference on Nano/Micro Engineered and Molecular Systems, 16-19 Jan. 2007*, Piscataway, NJ, USA, 2007, p. 6 pp.
- [13] J. Johansson and J. Delsing, "Microelectronics mounted on a piezoelectric transducer: Method, simulations, and measurements," *Ultrasonics*, vol. 44, pp. 1-11, 1// 2006.
- [14] Noliac Sensors and Tansducers Datasheet [Online].
- [15] L. Ji-Tzuoh, D. Jackson, J. Aebersold, K. Walsh, J. Naber, and W. Hnat, "A High Gauge Factor Capacitive Strain Sensor and its Telemetry Application in Biomechanics," in *University/Government/Industry Micro/Nano Symposium, 2008. UGIM 2008. 17th Biennial, 2008*, pp. 98-101.
- [16] ON CHIP CAPACITIVE PRESSURE SENSORS FRAUNHOFER IMS 02 [Online].
- [17] X. Yang, J. Lim, G. Sun, K. Wu, T. Nishida, and S. E. Thompson, "Strain-induced changes in the gate tunneling currents in p-channel metal-oxide-semiconductor field-effect transistors," *Appl. Phys. Lett.*, vol. 88, pp. 052108-3, Jan. 2006.
- [18] J. C. Ranuárez, M. J. Deen, and C.-H. Chen, "A review of gate tunneling current in MOS devices," *Microelectronics Reliability*, vol. 46, pp. 1939-1956, 12// 2006.
- [19] *International technology roadmap for semiconductors, 2013 update*. Available: <http://public.itrs.net/>
- [20] B. Majkusiak, "Gate tunnel current in an MOS transistors," *Electron Devices, IEEE Transactions on*, vol. 37, pp. 1087-1092, 1990.
- [21] Y. Cherng-Ming, C. Shui-Ming, and S. S. Chung, "A new approach to simulating n-MOSFET gate current degradation by including hot-electron induced oxide damage," *Electron Devices, IEEE Transactions on*, vol. 45, pp. 2343-2348, 1998.



- [22] J.-W. Lee, P. Chan Hyeong, S. Hyungcheol, B.-G. Park, and J.-H. Lee, "Accurate extraction of  $I_{leak}$  due to random telegraph noise in gate edge current of high-k  $n$ -type metal-oxide-semiconductor field-effect transistors under accumulation mode," *Applied Physics Letters*, vol. 98, pp. 023505-023505-3, 2011.
- [23] Y. Jian-Hong, L. Gui-Fang, and L. Hui-Lan, "Off-state leakage current in nano-scale MOSFET with Hf-based gate dielectrics," in *Nanoelectronics Conference, 2008. INEC 2008. 2nd IEEE International*, 2008, pp. 1189-1192.
- [24] C. M. Yih, S. S. Chung, and C. C. H. Hsu, "A numerical model for simulating MOSFET gate current degradation by considering the interface state generation," in *Simulation of Semiconductor Processes and Devices, 1996. SISPAD 96. 1996 International Conference on*, 1996, pp. 115-116.
- [25] S. Tsujikawa, Y. Akamatsu, H. Umeda, and J. Yugami, "Two concerns about NBTI issue: gate dielectric scaling and increasing gate current," in *Reliability Physics Symposium Proceedings, 2004. 42nd Annual. 2004 IEEE International*, 2004, pp. 28-34.
- [26] A. Yassine and R. Hijab, "Temperature dependence of gate current in ultra thin  $\text{SiO}_2$  in direct-tunneling regime," in *Integrated Reliability Workshop Final Report, 1997 IEEE International*, 1997, pp. 56-61.
- [27] L. Wei-Han and C. Ming-Jer, "Gate Direct Tunneling Current in Uniaxially Compressive Strained nMOSFETs: A Sensitive Measure of Electron Piezo Effective Mass," *Electron Devices, IEEE Transactions on*, vol. 58, pp. 39-45, 2011.
- [28] Z. Wei, A. Seabaugh, V. Adams, D. Jovanovic, and B. Winstead, "Opposing dependence of the electron and hole gate currents in SOI MOSFETs under uniaxial strain," *Electron Device Letters, IEEE*, vol. 26, pp. 410-412, 2005.
- [29] S. Goswami and A. Biswas, "Modeling and numerical simulation of gate leakage current in strained-Si channel nMOSFETs with highk gate dielectrics," in *Emerging Trends in Electronic and Photonic Devices & Systems, 2009. ELECTRO '09. International Conference on*, 2009, pp. 33-36.
- [30] S. Y. Son, Y. S. Choi, P. Kumar, H. W. Park, T. Nishida, R. K. Singh, *et al.*, "Strain induced changes in gate leakage current and dielectric constant of nitrated Hf-silicate metal oxide semiconductor capacitors," *Applied Physics Letters*, vol. 93, pp. 153505-153505-3, 2008.
- [31] L. Esaki, "Long journey into tunneling," *Reviews of Modern Physics*, vol. 46, pp. 237-244, 04/01/ 1974.

- [32] M. Razavy, *Quantum Theory of Tunneling*: World Scientific, 2003.
- [33] H. Geiger and J. M. Nuttall, "The ranges of the  $\alpha$  particles from various radioactive substances and a relation between range and period of transformation," *Philosophical Magazine*, vol. 22, pp. 613-621, 1911.
- [34] R. H. Fowler and L. Nordheim, "Electron Emission in Intense Electric Fields," *Proceedings of the Royal Society of London*, vol. 119, pp. 173-181, 1928.
- [35] J. Frenkel, "On the Electrical Resistance of Contacts between Solid Conductors," *Physical Review*, vol. 36, pp. 1604-1618, 1930.
- [36] A. H. Wilson, "A Note on the Theory of Rectification," *Proceedings of the Royal Society of London. Series A, Containing Papers of a Mathematical and Physical Character*, vol. 136, pp. 487-498, 1932.
- [37] "Frenkel, J. and Joffe, A., *Physik. Z. Sowjetunion* I, 60 (1932)."
- [38] "Nordheim, L., *Z. Physik* 7.5, 434 (1932)."
- [39] I. Giaever, "Electron Tunneling and Superconductivity," *Science*, vol. 183, pp. 1253-1258, March 29, 1974 1974.
- [40] M. Lenzlinger and E. H. Snow, "Fowler-Nordheim Tunneling into Thermally Grown SiO<sub>2</sub>," *Journal of Applied Physics*, vol. 40, pp. 278-283, 1969.
- [41] R. Entner, "Modeling and Simulation of Negative Bias Temperature Instability," Ph.D, Technische Universitat Wien, 2007.
- [42] R. Tsu and L. Esaki, "Tunneling in a finite superlattice," *Applied Physics Letters*, vol. 22, pp. 562-564, 1973.
- [43] "WKB approximation," in *Wikipedia*, ed.
- [44] R. Clerc, A. Spinelli, G. Ghibaudo, and G. Pananakakis, "Theory of direct tunneling current in metal--oxide--semiconductor structures," *Journal of Applied Physics*, vol. 91, pp. 1400-1409, 2002.
- [45] PowerPoint. Inclusion of Tunneling and Size-Quantization Effects in Semi-Classical Simulators.
- [46] M. Razeghi, *Fundamentals of Solid State Engineering*, Third ed.: Springer, 2009.
- [47] Wikipedia. *Silicon-unit-cell-3D-balls*.
- [48] R. F. Pierret, *Advanced Semiconductor Fundamentals*, 2nd ed. vol. V: Pearson Education, 2002.

- [49] H. Föll. *Semiconductor I*. Available: [http://www.tf.uni-kiel.de/matwis/amat/semi\\_en/index.html](http://www.tf.uni-kiel.de/matwis/amat/semi_en/index.html)
- [50] D. B. Jochym, "Development of Non-Local Density Functional Methods," Ph.D, Department of Physics, University of Durham, 2008.
- [51] efunda. *Mechanics of Materials: Stress*. Available: [http://www.efunda.com/formulae/solid\\_mechanics/mat\\_mechanics/stress.cfm](http://www.efunda.com/formulae/solid_mechanics/mat_mechanics/stress.cfm)
- [52] Y. Sun, S. E. Thompson, and T. Nishida, *Strain Effect in Semiconductors: Theory and Device Applications*: Springer, 2010.
- [53] Y. Sun, S. E. Thompson, and T. Nishida, "Physics of strain effects in semiconductors and metal-oxide-semiconductor field-effect transistors," *Journal of Applied Physics*, vol. 101, pp. 104503-1, 2007.
- [54] X. D. Yang, Y. Choi, J. Lim, T. Nishida, and S. Thompson, "Strain induced changes in the gate leakage current of n-channel metal-oxide-semiconductor field-effect transistors," *Journal of Applied Physics*, vol. 110, Jul 1 2011.
- [55] X. Yang, Y. Choi, J. Lim, T. Nishida, and S. Thompson, "Strain induced changes in the gate leakage current of n-channel metal-oxide-semiconductor field-effect transistors," *J. Appl. Phys.*, vol. 110, pp. 014511-014511-8, Jul. 2011.
- [56] Y. Nian, W. K. Henson, J. R. Hauser, and J. J. Wortman, "Modeling study of ultrathin gate oxides using direct tunneling current and capacitance-voltage measurements in MOS devices," *IEEE Trans. Electron Devices*, vol. 46, pp. 1464-1471, July 1999.
- [57] L. F. Register, E. Rosenbaum, and K. Yang, "Analytic model for direct tunneling current in polycrystalline silicon-gate metal-oxide-semiconductor devices," *Appl. Phys. Lett.*, vol. 74, pp. 457-459, Jan. 1999.
- [58] M. M. Rieger and P. Vogl, "Electronic-band parameters in strained  $\text{Si}_{1-x}\text{Ge}_x$  alloys on  $\text{Si}_{1-y}\text{Ge}_y$  substrates," *Phys. Rev. B*, vol. 48, pp. 14276-14287, Nov. 1993.
- [59] T. Ando, A. B. Fowler, and F. Stern, "Electronic properties of two-dimensional systems," *Rev. Mod. Phys.*, vol. 54, pp. 437-672, Apr. 1982.
- [60] F. Stern, "Self-Consistent Results for n-Type Si Inversion Layers," *Phys. Rev. B*, vol. 5, pp. 4891-4899, Jun. 1972.
- [61] F. F. Fang and W. E. Howard, "Negative Field-Effect Mobility on (100) Si Surfaces," *Phys. Rev. Lett.*, vol. 16, pp. 797-799, May 1966.

- [62] D. Vasileska, S. S. Ahmed, G. Kannan, M. Mannino, G. Klimeck, M. Lundstrom, *et al.*, "Schred," ed, 2006.
- [63] F. Rana, S. Tiwari, and D. A. Buchanan, "Self-consistent modeling of accumulation layers and tunneling currents through very thin oxides," *Appl. Phys. Lett.*, vol. 69, pp. 1104-1106, Aug. 1996.
- [64] L. Zhu and S. McNamara, "Computationally Efficient Modeling of Uniaxial Stressed NMOS Gate Current in Inversion Layer," *Journal of Micromechanics and Microengineering*, 2014.
- [65] Y. Taur and T. H. Ning, *Fundamentals of Modern VLSI Devices*: Cambridge University Press, 2009.
- [66] J.-S. Lim, X. Yang, T. Nishida, and S. E. Thompson, "Measurement of conduction band deformation potential constants using gate direct tunneling current in n-type metal oxide semiconductor field effect transistors under mechanical stress," *Appl. Phys. Lett.*, vol. 89, pp. 073509-073509-3, Aug. 2006.
- [67] P. Chan-Kwang, L. Chang-Yeol, L. Kwyro, M. Byung-Jong, B. Young Hee, and M. Shur, "A unified current-voltage model for long-channel nMOSFETs," *IEEE Trans. Electron Devices*, vol. 38, pp. 399-406, Feb. 1991.
- [68] Y. Ma, L. Litian, Y. Zhiping, and L. Zhijian, "Validity and applicability of triangular potential well approximation in modeling of MOS structure inversion and accumulation layer," *IEEE Trans. Electron Devices*, vol. 47, pp. 1764-1767, Sep. 2000.
- [69] R. Tsu and L. Esaki, "Tunneling in a finite superlattice," *Appl. Phys. Lett.*, vol. 22, pp. 562-564, 1973.
- [70] W. Weimin, L. Xin, G. Gildenblat, G. O. Workman, S. Veeraraghavan, C. C. McAndrew, *et al.*, "A Compact Model for Valence-Band Electron Tunneling Current in Partially Depleted SOI MOSFETs," *Electron Devices, IEEE Transactions on*, vol. 54, pp. 316-322, 2007.
- [71] Y. Sun, S. E. Thompson, and T. Nishida, "Physics of strain effects in semiconductors and metal-oxide-semiconductor field-effect transistors," *J. Appl. Phys.*, vol. 101, pp. 104503-1, 2007.
- [72] M. Konno, T. Ikehara, S. Murakami, R. Maeda, M. Kimura, T. Fukawa, *et al.*, "Novel MEMS oscillator using in-plane disk resonator with sensing platform and its mass sensing characteristics," in *Solid-State Sensors, Actuators and Microsystems Conference (TRANSDUCERS), 2011 16th International*, 2011, pp. 518-521.
- [73] J. Lu, T. Sagawa, L. Zhang, H. Takagi, D. F. Wang, T. Itoh, *et al.*, "Piezoelectric MEMS devices and its application as bio-chemical sensors," in *Nano/Micro Engineered and Molecular Systems (NEMS), 2013 8th IEEE International Conference on*, 2013, pp. 163-166.

- [74] W. Xiaotie, Z. Chengjie, Z. Milin, J. Van der Spiegel, and G. Piazza, "A 47-MHz 204MHz AIN Contour-Mode MEMS based tunable oscillator in 65nm CMOS," in *Circuits and Systems (ISCAS), 2013 IEEE International Symposium on*, 2013, pp. 1757-1760.
- [75] J. H. Kuypers, G. Zolfagharkhani, A. Gaidarzhy, F. Thalmayr, A. Sparks, D. M. Chen, *et al.*, "Wafer-level chip scale MEMS oscillator for wireless applications," in *Frequency Control Symposium (FCS), 2012 IEEE International*, 2012, pp. 1-5.
- [76] S. Yonghyun, R. Jia, W. Zhengzheng, and M. Rais-Zadeh, "An integrated RF MEMS tunable filter," in *Micro Electro Mechanical Systems (MEMS), 2012 IEEE 25th International Conference on*, 2012, pp. 15-18.
- [77] L. Kok-Yan and G. M. Rebeiz, "A miniature 8-16 GHz packaged tunable frequency and bandwidth RF MEMS filter," in *Radio-Frequency Integration Technology, 2009. RFIT 2009. IEEE International Symposium on*, 2009, pp. 249-252.
- [78] R. Marathe, W. Wentao, and D. Weinstein, "Si-based unreleased hybrid MEMS-CMOS resonators in 32nm technology," in *Micro Electro Mechanical Systems (MEMS), 2012 IEEE 25th International Conference on*, 2012, pp. 729-732.
- [79] G. K. Fedder, R. T. Howe, L. Tsu-Jae King, and E. P. Quevy, "Technologies for Cofabricating MEMS and Electronics," *Proceedings of the IEEE*, vol. 96, pp. 306-322, 2008.
- [80] G.-C. Wei and M. S.-C. Lu, "Design and characterization of a CMOS MEMS capacitive resonant sensor array," *Journal of Micromechanics and Microengineering*, vol. 22, p. 125030, 2012.
- [81] N. V. Toan, M. Toda, Y. Kawai, and T. Ono, "A capacitive silicon resonator with a movable electrode structure for gap width reduction," *Journal of Micromechanics and Microengineering*, vol. 24, p. 025006, 2014.
- [82] J. T. M. v. Beek and R. Puers, "A review of MEMS oscillators for frequency reference and timing applications," *Journal of Micromechanics and Microengineering*, vol. 22, p. 013001, 2012.
- [83] J. Basu and T. K. Bhattacharyya, "Microelectromechanical resonators for radio frequency communication applications," *Microsyst. Technol.*, vol. 17, pp. 1557-1580, 2011.
- [84] D. K. Shaeffer, "MEMS inertial sensors: A tutorial overview," *Communications Magazine, IEEE*, vol. 51, pp. 100-109, 2013.
- [85] T. Mattila, J. Kiihamäki, T. Lamminmäki, O. Jaakkola, P. Rantakari, A. Oja, *et al.*, "A 12 MHz micromechanical bulk acoustic mode oscillator," *Sensors and Actuators A: Physical*, vol. 101, pp. 1-9, 9/30/ 2002.

- [86] J. Bernstein. (2003). *An Overview of MEMS Inertial Sensing Technology*. Available: <http://www.sensorsmag.com/sensors/acceleration-vibration/an-overview-mems-inertial-sensing-technology-970>
- [87] B. Antkowiak, J. P. Gorman, M. Varghese, D. J. D. Carter, and A. E. Duwel, "Design of a high-Q, low-impedance, GHz-range piezoelectric mems resonator," in *TRANSDUCERS, Solid-State Sensors, Actuators and Microsystems, 12th International Conference on, 2003*, 2003, pp. 841-846 vol.1.
- [88] R. Resmi and M. R. Baiju, "Performance analysis of a tunable piezoelectric actuator based MEMS resonator," in *MIPRO, 2012 Proceedings of the 35th International Convention, 2012*, pp. 173-178.
- [89] Z. Chengjie, J. Van der Spiegel, and G. Piazza, "1.5-GHz CMOS voltage-controlled oscillator based on thickness-field-excited piezoelectric AlN contour-mode MEMS resonators," in *Custom Integrated Circuits Conference (CICC), 2010 IEEE, 2010*, pp. 1-4.
- [90] K. L. Phan, T. van Ansem, C. van der Avoort, J. T. M. van Beek, M. J. Goossens, S. Jose, *et al.*, "High precision frequency synthesizer based on MEMS piezoresistive resonator," in *Solid-State Sensors, Actuators and Microsystems (TRANSDUCERS & EUROSENSORS XXVII), 2013 Transducers & Eurosensors XXVII: The 17th International Conference on, 2013*, pp. 802-805.
- [91] J. T. M. van Beek, P. G. Steeneken, and B. Giesbers, "A 10MHz piezoresistive MEMS resonator with high Q," in *International Frequency Control Symposium and Exposition, 2006 IEEE, 2006*, pp. 475-480.
- [92] H. Wan-Thai, "Vibrating RF MEMS for Timing and Frequency References," in *Microwave Symposium Digest, 2006. IEEE MTT-S International, 2006*, pp. 672-675.
- [93] F. D. Bannon, J. R. Clark, and C. T. C. Nguyen, "High-Q HF microelectromechanical filters," *Solid-State Circuits, IEEE Journal of*, vol. 35, pp. 512-526, 2000.
- [94] A. A. Zainuddin, J. Karim, A. N. Nordin, M. S. Pandian, and K. Sheroz, "Design and simulation of Clamped-Clamped and Clamped-Free resonators," in *Quality Electronic Design (ASQED), 2013 5th Asia Symposium on, 2013*, pp. 55-59.
- [95] W. Kun, W. Ark-Chew, and C. T. C. Nguyen, "VHF free-free beam high-Q micromechanical resonators," *Microelectromechanical Systems, Journal of*, vol. 9, pp. 347-360, 2000.
- [96] V. Kaajakari, T. Mattila, A. Oja, J. Kiihamaki, H. Kattelus, M. Koskenvuori, *et al.*, "Square-extensional mode single-crystal silicon micromechanical RF-resonator," in *TRANSDUCERS, Solid-State*

*Sensors, Actuators and Microsystems, 12th International Conference on, 2003*, 2003, pp. 951-954 vol.2.

- [97] M. A. Abdelmoneum, M. U. Demirci, and C. T. C. Nguyen, "Stemless wine-glass-mode disk micromechanical resonators," in *Micro Electro Mechanical Systems, 2003. MEMS-03 Kyoto. IEEE The Sixteenth Annual International Conference on, 2003*, pp. 698-701.
- [98] X. Yuan, L. Sheng-Shian, L. Yu-Wei, R. Zeying, and C. T. C. Nguyen, "UHF micromechanical extensional wine-glass mode ring resonators," in *Electron Devices Meeting, 2003. IEDM '03 Technical Digest. IEEE International, 2003*, pp. 39.2.1-39.2.4.
- [99] J. Garima, D. N. Singh, and S. Thangjam, "Effect of Temperature Variation on Gate Tunneling Currents in Nanoscale MOSFETs," in *Nanotechnology, 2008. NANO '08. 8th IEEE Conference on, 2008*, pp. 37-41.
- [100] C. H. Ang, C. H. Ling, Z. Y. Cheng, and B. J. Cho, "Origin of temperature-sensitive hole current at low gate voltage regime in ultrathin gate oxide," *Journal of Applied Physics*, vol. 88, pp. 2872-2876, 2000.

## CURRICULUM VITAE

### CONTACT INFORMATION

---

Li Zhu

Shumaker Research Building, Room 209,  
University of Louisville, Louisville, KY, 40206.

Cell Phone: 336-745-6981

Email: li.zhu@louisville.edu

### EDUCATION

---

- ❖ Aug. 2009 – Apr. 2014  
Ph.D Candidate in Electrical Engineering, University of Louisville, KY,  
USGPA: 4.00/4.00
- ❖ Sept. 2007 – July 2009  
M.S. in Optical Engineering, Beijing Institute of Technology, Beijing, China
- ❖ Sept. 2003 – July 2007  
B.S. in Optical Engineering, Beijing Institute of Technology, Beijing, China

### EXPERIENCE

---

Research Assistant

University of Louisville

Aug. 2009 – Present (4 years 7 months)

Dissertation:

Low power strain sensor based on MOS tunneling current

- Built models for MOS tunneling current in strain sensor.
- Fabricated MOS tunneling strain sensor in cleanroom.
- Tested the device using both DC and AC method. HP4145a was used in the DC method. For the AC method, designed a preamplifier circuit to transfer tunneling current to voltage and used SR7265 lock-in amplifier to measure the tunneling current. Used Labview to control Hp4145a semiconductor analyzer and SR7265 lock-in amplifier.



- Developed MOS tunneling current RF resonator (12 MHz). Coventorware and COMSOL were used to design the resonator. Fabricated in University of Louisville's cleanroom. Tested using network analyzer, LCR meter and oscilloscope.

#### Research Assistant

Beijing Institute of Technology

Jan. 2007 – June 2009 (2 years 5 months)

Thesis:

System design and simulation of 0.2 THz radar

- System design of a 0.2 THz stepped frequency transmitter and receiver.
- Used Simulink in Matlab to simulate the space resolution of the radar in a system level.
- Used ADS to simulate power and noise of the output of the transmitter line by using parameters from actual parts.

#### TEACHING EXPERIENCE

---

- ❖ Introduction to microelectronics (lab in the cleanroom and lecture), Spring semester, 2012 & 2013;
- ❖ Microelectronics design and fabrication (lab in the cleanroom and part time lecture), Spring semester, 2013;
- ❖ Semiconductor fundamentals (part time lecture), Fall semester, 2012;
- ❖ Advanced MEMS (lab in the cleanroom), Spring semester, 2012.

#### AWARDS

---

- ❖ University Fellowship, University of Louisville, 2009;
- ❖ Graduate admission with qualification exams waiver, Beijing Institute of Technology (BIT), 2007;
- ❖ Renmin scholarship, first class, BIT, 2005 – 2006;
- ❖ Beijing College Student Physics contest, third class, BIT, 2004 – 2005;
- ❖ Outstanding student scholarship, BIT, 2004 – 2005;
- ❖ Renmin scholarship, first class, BIT, 2004 – 2005;
- ❖ Renmin scholarship, second class, BIT, 2003 – 2004.

#### PUBLICATIONS & POSTERS

---

[1]. Li Zhu, Ruchira Dharmasena and Shamus McNamara, "MOS Tunneling Strain Sensor Using an AC Measurement Technique," *IEEE NEMS, 2013 Suzhou, China: p.1159-1162.*

[2]. Li Zhu and Shamus McNamara, "Low power strain sensing using tunneling current through MOS capacitors," in Digest, *IEEE Solid-State Sensor and Actuator Workshop, 2012 Hilton-Head, SC: p.457-460.*

- [3]. Li Zhu, Chao Deng, Cun-lin Zhang, Yue-jin Zhao, "System Simulation of a 0.2 THz imaging radar", *Proc. SPIE, Vol. 7385, 738523 (2009)*.
- [4]. Li Zhu and Shamus McNamara, "Computationally Efficient Modeling of MOS Tunneling Current Micro Strain Sensor," *Journal of Micromechanics and Microengineering*. (Under review).
- [5]. Li Zhu and Shamus McNamara, "Effect of Substrate Doping Concentration on NMOS Tunneling Current Strain Sensor," *IEEE Electron Device Letters*. (Under review).
- [6]. Li Zhu and Shamus McNamara, "LOW POWER STRAIN SENSING USING TUNNELING CURRENT THROUGH MOS CAPACITORS- EXPERIMENT AND MODELING," *Journal of microelectromechanical systems*. (Under review).
- [7]. Li Zhu, Bryan Snatchko and Shamus McNamara, "A new oscillator using MOS tunneling resonator," KY EPSCOR conference, Oct. 17th, 2014. Open Poster.
- [8]. Li Zhu, Bryan Snatchko and Shamus McNamara, "MOS tunneling sensing for resonant sensors," IEEE sensors, 2013. Open Poster.